ECOLE POLYTECHINQUE FÉDÉRALE DE LAUSANNE

MASTER THESIS

Climatology of atmospheric boundary layer height over Switzerland

Author:
Benjamin HEUTTE

Supervisors:
Martine COLLAUD COEN,
Alexis BERNE

Bundesamt für Meteorologie und Klimatologie MeteoSchweiz

A thesis submitted in fulfillment of the requirements
for the degree of Master in Environmental Sciences and Engineering

in the

Environmental Remote Sensing Laboratory LTE
Environmental Sciences and Engineering

August 19, 2021

Declaration of Authorship

I, Benjamin HEUTTE, declare that this thesis titled, "Climatology of atmospheric boundary layer height over Switzerland" and the work presented in it are my own. I confirm that:

- Where I have consulted the published work of others, this is always clearly attributed.
- Where I have quoted from the work of others, the source is always given. With the exception of such quotations, this thesis is entirely my own work.
- I have acknowledged all main sources of help.
- Where the thesis is based on work done by myself jointly with others, I have made clear exactly what was done by others and what I have contributed myself.

Signed:

Date:

ECOLE POLYTECHINQUE FÉDÉRALE DE LAUSANNE

Abstract

Determining the height of the planetary boundary layer (PBL) is of crucial importance as it is a key parameter in air-quality modelling and weather forecasting. Continuous remote sensing measurements allow to estimate this parameter based on temperature, humidity, turbulence, or aerosol backscatter profiles. In this study, measurements from radiosounding (RS), lidars, microwave radiometers (MWR) and wind profilers (WP) were coupled to various detection methods (parcel method (PM), bulk-Richardson number method (bR), surface-based temperature inversion (SBI), potential temperature gradients (SBLpt), aerosol scattering ratio (ASR) and signal-to-noise (SNR) ratio gradients) for day-time and night-time detection of the PBL height. An inter-comparison of the results from each set of instrument and method, for a period of 5 years (2016-2020), was performed taking RS with PM as reference. The Raman lidar (RALMO) and the COSMO model showed very good agreements with RS, while MWR underestimated the PBL height, mostly in summer, probably due to an overheating of the instrument by the sun. This study notably exposed the great perspective of using temperature and humidity profiles retrieved with RALMO to estimate the PBL height. WP showed more scattered, and overall underestimated, results as the measured maximum of turbulence did not always correspond to the PBL height. A 5-year climatology resulted in clear seasonal and diurnal cycles, with maximum height attained in summer, during the day between 12:00 and 14:00, and a minimum in wintertime. Clear and cloudy sky differentiation showed a negative correlation between the PBL height and cloudiness. A decrease of the PBL height in June was observed with all instruments and methods in the three stations of interest, with no clear explanation of the phenomenon. During the night, the bR method has been invalidated due to its tendency to detect layers, almost constantly, just above ground with RS and KENDA. For RALMO and MWR, the use of wind speed measurements from WP in the bR method resulted in a positive bias of the results. This was attributed to a large amount of missing WP data points near ground due to ground clutter and weak nightly turbulences bellow the detection threshold. The growth rate of the convective layer during the day showed similar seasonality, with a maximum in summer and a minimum in autumn when using RALMO and KENDA. An under-estimation of the growth rate was observed using MWR, as a consequence of the underestimated convective boundary layer height. The analysis of a 30-year long-term PBL height trend, using RS, resulted in a small positive trend using PM and negative using bR method, with weak statistical significance. Trends with larger magnitude were observed with shorter data sets from 10 to 20 years, suggesting that stronger variations are observed on the decadal time scale, due to climate oscillations. Finally, the restrictions for each instrument and method, due to weather conditions, vertical resolution and accuracy have been exposed and discussed in this study.

KEYWORDS: *planetary boundary layer*, *remote sensing*, *climatology*, *long-term trends*, *PBL diurnal and seasonal cycle*, *clear-cloudy sky differentiation*

ECOLE POLYTECHINQUE FÉDÉRALE DE LAUSANNE

Résumé

La détermination de la hauteur de la couche limite planétaire (PBL) est d'une importance capitale puisqu'il s'agit d'un paramètre clé dans la modélisation de la qualité de l'air et dans les prévisions météorologiques. Les mesures de télédétection en continu permettent d'estimer ce paramètre en se basant sur des profils de température, humidité, turbulence ou rétrodiffusion des aérosols. Dans cette étude, des mesures provenant de radiosondages (RS), lidars, radiomètres micro-ondes (MWR) et profileurs de vent (WP) ont été couplées à diverses méthodes de détéction (méthode de parcelle (PM), méthode du nombre global de Richardson (bR), inversion de la température en surface (SBI), gradient de température potentielle (SBLpt) et gradient des rapports de diffusion des aérosols (ASR) et signal sur bruit (SNR)) pour la détection diurne et nocturne de la hauteur de la PBL. Une comparaison des résultats de chaque paire d'instrument et méthode, pour une période de 5 ans (2016-2020), a été réalisée en prenant RS avec PM comme référence. Le lidar Raman (RALMO) et le modèle KENDA ont montré de très bons résultats, tandis que MWR a sous-estimé la hauteur de la PBL, principalement en été, probablement en raison d'une surchauffe de l'instrument par le soleil. Cette étude a notamment montré l'intérêt d'utiliser les profils de température et d'humidité obtenus par RALMO pour estimer la hauteur de la PBL. Le WP a apporté des résultats plus disparates, et globalement sous-estimés, car le maximum de turbulence mesuré ne correspondait pas toujours à la hauteur de la PBL. Une climatologie sur 5 ans a permis d'établir des cycles saisonniers et diurnes clairs, avec une hauteur maximale atteinte en été, pendant la journée entre 12h00 et 14h00, et un minimum en hiver. La différenciation des conditions de ciels dégagés et nuageux a montré une correlation negative entre la hauteur de la PBL et la nébulosité. Une diminution de la hauteur de la PBL en Juin a été observée avec tous les instruments et toutes les méthodes dans les trois stations d'intérêt, sans explication claire du phénomène. Pendant la nuit, la méthode bR a été invalidée en raison de sa tendance à détecter des couches, presque constamment, juste au-dessus du sol avec RS et KENDA. Pour RALMO et MWR, l'utilisation des mesures de vitesse du vent du WP dans la méthode bR a entraîné un biais positif des résultats. Cela peut être attribué à un grand nombre de données WP manquantes près du sol en raison d'un bruitage du signal au sol et de faibles turbulences nocturnes en dessous du seuil de détection. La vitesse de croissance de la couche convective pendant la journée a montré une saisonnalité similaire, avec un maximum en été et un minimum en automne en utilisant RALMO et KENDA. Une sous-estimation de la vitesse de croissance a été observée avec le MWR, attribuée à la sous-estimation de la mesure de la hauteur de la couche convective. L'analyse des tendances à long terme, sur 30 ans, de la hauteur de la couche convective, en utilisant RS, a abouti à une faible tendance positive en utilisant PM et négative en utilisant la méthode bR, avec une faible signification statistique. Des tendances plus marquées ont été observées sur des périodes plus courtes, de 10 à 20 ans, suggérant que des variations plus fortes sont observées à l'échelle décennale, causées par des oscillations climatiques. Enfin, les restrictions pour chaque instrument et méthode, dues aux conditions météorologiques, à la résolution verticale et à la précision des mesures, ont été mises en avant et discutées dans cette étude.

MOTS-CLES: *couche limite planétaire, télédétection, climatologie, tendances à long terme, cycles diurnes/saisonniers de la PBL, différenciation de ciel nuageux et dégagé*

Acknowledgements

I would like to thank, from the bottom of my heart, Martine Collaud Coen, who took the responsibility and the time to supervise this project and provided priceless help constantly, and especially when most needed. I also thank Alexis Berne, who agreed to supervise this project on the EPFL side and kept a great interest in the work I was doing all along.

I am also greatly thankful for the help provided by all the employees of the MDA section at MeteoSwiss Payerne. In particular, I would like to thank Maxime Hervo, Giovanni Martucci and Rolf Ruefenacht who gave a considerable amount of their time to help me find my way into this project. I wish to thank Philippe Overney and Jean-Christian Zill for their IT support along this journey.

Finally, many thanks go to my colleagues at the APN section in Zurich (Daniel Leuenberg, Marco Arpagaus, Pirmin Kaufmann) for providing data and sharing their knowledge and enthusiasm of the PBL with me.

Contents

List of Figures

List of Tables

List of Abbreviations

ABL	Atmospheric Boundary Level
agl	above ground level
APCADA	Automatic Partial Cloud Amount Detection Algorithm
asl	above sea level
ASR	Aerosol Scattering Ratio
bR	bulk Richardson number method
CBL	Convective Boundary Layer
CBLH	Convective Boundary Layer Height
CBLH^{Max}	CBLH daily maxima
COSMO	COnsortium for Small-scale MOdeling
GRE	GREnchen measuring station
KENDA	Kilometer-scale ENsemble Data Assimilation for cosmo model
MLH	Mixing Layer Height
MWR	MicroWave Radiometer
NBL	Neutral Boundary Layer
PAY	PAYerne measuring station
PBL	Planetary Boundary Layer
PBLH	Planetary Boundary Layer Height
PM	Parcel Method
RALMO	RAman Lidar for Meteorological Observations
REM	REMote sensing
RS	Radio Sounding
RL	Residual Layer
SBI	Surface-based Temperature Inversion
SBL	Stable Boundary Layer
SBLpt	Stable Boundary Layer detected by potential temperature
SHA	ScHAffhausen measuring station
SMN	SwissMetNet
SNR	Signal-to-Noise Ratio
WP	Wind Profiler

Physical Constants

Earth gravitational acceleration	$g = 9.806\,65\,\mathrm{m\,s^{-1}}$
Gravitational constant	$G = 6.674\,30(15) \times 10^{-11}\,\mathrm{m^3\,kg^{-1}\,s^{-2}}$
Molar gas constant	$R = 8.314\,46\,\mathrm{J\,K^{-1}\,mol^{-1}}$
Molar mass of dry air	$M_a = 28.965\,\mathrm{g\,mol^{-1}}$
Molar mass of water	$M_w = 18.016\,\mathrm{g\,mol^{-1}}$

Chapter 1

Introduction

The lowest layer of the atmosphere, the troposphere, can be divided in two parts: the planetary (or atmospheric) boundary layer (PBL) and the remaining free troposphere (FT). The former is defined as the *layer directly influenced by the presence of the earth's surface, responding to surface forcing with a timescale of about an hour or less* (Stull, 1998). Determining the height of the PBL is of crucial importance as it is a key parameter for pollutant dispersion such as aerosols (Li et al., 2017), greenhouse gases (Barrera et al., 2019) or nuclear particles (Calpini et al., 2011). Quite notably, the top of the PBL determines the available volume for pollutants dispersion through advection and convection, as well as cloud height formation. It is hence a very important parameter in air-quality modelling and weather forecasting.

The PBL is characterised by a diurnal cycle, for which the growth, extent and decline of each layer depends greatly on the terrain (topography, land-use, soil moisture, vegetation, etc (Rihani et al., 2015; Pielke, 2001)) and weather conditions. For a clear-sky day, the structure of the PBL is well established (see Figure 1.1). Shortly after sunrise, solar radiation causes the ground to heat up, which in turns leads to the development of a convective boundary layer (CBL), also called mixing layer (ML). The growth and extent of this layer is primarily defined by the intensity of vertical buoyant turbulences, characterized by a strong positive vertical heat flux. In general, a maximum height is reached in the afternoon (around 14:00). The region, of variable thickness, between the CBL and the FT is known as the entrainment zone, where warm ascending air from the CBL penetrates the above FT. At the end of the afternoon, the turbulence intensity decreases until, eventually, the vertical heat flux becomes negative. The aerosols and gases trapped in the CBL during the day tend to persist at higher altitude in what is known has the residual layer (RL). As its name indicates, the RL is a residual of the CBL, and share the common characteristic to be both marked by a sharp decrease in airborne particle's concentration (i.e. pollutants emitted at ground, water vapor and other gases) at their interface with the FT. The RL is however less turbulent than the CBL and most often neutrally stratified (Stull, 1998). Meanwhile, during the night, radiative cooling at the ground results in the formation of a stable boundary layer (SBL). This layer is characterised by a surface-based temperature inversion (SBI) and a poorly defined top merging with the RL. The top of the SBL can however be estimated by the altitude at which the gradient of the potential temperature becomes null (neutrality). Pollutants emitted during the night will most often be contained in the SBL, with a very limited vertical displacement.

In cloudy-sky conditions, without precipitations, while the overall structure of the PBL is preserved, the physical mechanisms behind it differ. During the day, convection is no longer primarily driven by solar heating of the ground but instead by radiative cooling from cloud top, cold air advection or ground thermal inertia (Collaud Coen et al., 2014; Stull, 1998). In any case, the growth and extent of the CBL is most often reduced. During the night however, the effect of clouds on the SBL and RL is less evident. Most studies treating the detection or analysis of the PBL height make no differentiation between clear

and cloudy sky conditions, due to the uncertainties that clouds bring in the determination of the PBL height (Kotthaus et al., 2021).

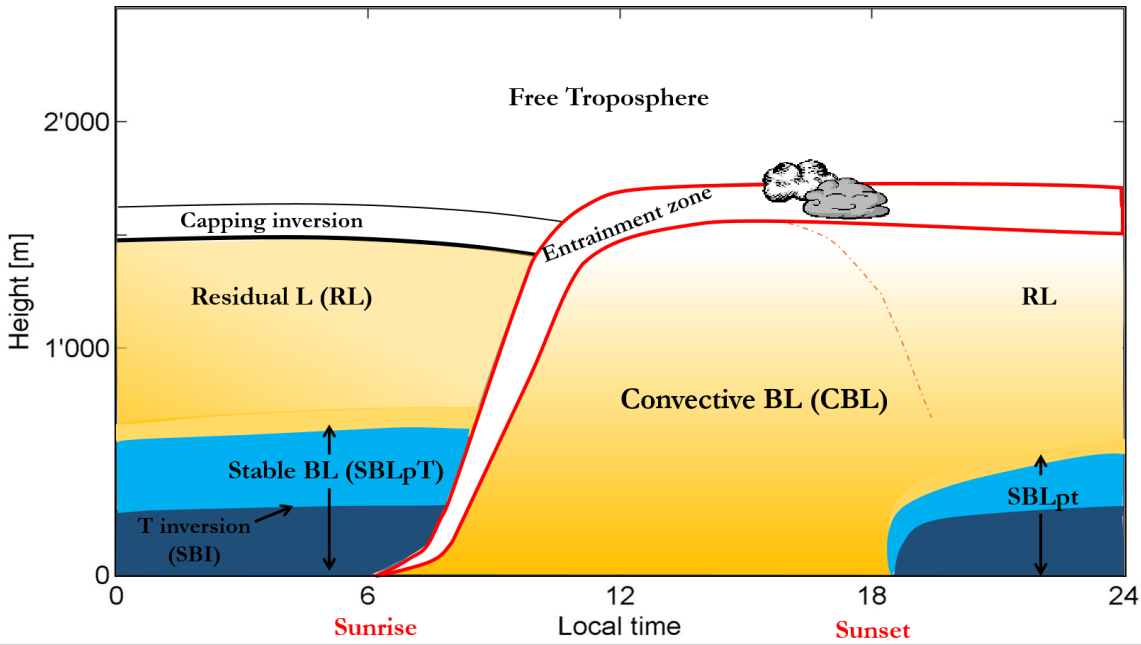

FIGURE 1.1: Diurnal cycle of the different PBL sub-layers' heights for a clear convective day (adaptation from Collaud Coen et al., 2014).

While PBLH determination by radio-sounding (RS) observations has proven to be accurate (Seidel et al., 2010; Sivaraman et al., 2013), measurements are most often only made twice a day (00:00 UTC and 12:00 UTC), making it a very limited instrument to recover the full diurnal dynamic of the PBL. Thereby, continuous remote sensing measurements are preferred for characterization of the PBL diurnal cycle. As such, ground-based lidars have received increasing interested for their ability to retrieve the PBL top with high time resolution (Baars et al., 2008; Pal and Haeffelin, 2015; Haeffelin et al., 2012), but with important problems of gradient attribution to the correct layers. Du et al., 2020, also proposed a new method for PBLH detection using satellite-based lidars. Microwave radiometers (MWR) have also been extensively used in recent studies (Cimini et al., 2013; Moreira et al., 2020), for they provide temperature and relative humidity profiles with high temporal resolution. PBLH detection has also been performed using wind profiler (WP) radars (Allabakash et al., 2017; Liu et al., 2019; Molod et al., 2019; Camilo et al., 2021), with the advantage of being less impacted by weather conditions as it is the case for radiometers or lidars. Finally, modelling of the PBLH is also an option, with models like COSMO (Szintai, 2010), being constantly improved for an accurate forecasting of atmospheric flows and dynamics. Overall, there have been numerous studies comparing and validating the results of different instruments and method (Herrera and Hoyos, 2019; Seidel et al., 2010; Emeis et al., 2012), most often using RS as a reference

A common effort towards determination and characterization of the PBL over Europe is currently ongoing, through the PROBE (PROfilling the atmospheric Boundary layer at European scale) initiative of the COST (European Cooperation in Science and Technology) action (Cimini et al., 2020). This project is also aiming for a global harmonization of the different instruments and detection methods for a higher quality PBL detection.

In this study, several remote sensing instruments coupled with various PBLH detection methods were used, with a 5-year data set from 2016 to 2020. RS, lidar and MWR were used to retrieve temperature and relative humidity profiles, where the lidar was also providing a full aerosols' backscattering profile. This study is one of the first to make use of T and RH profiles retrieved with a lidar to compute the PBLH with conventional T-related detection methods. Additionally, atmospheric wind speed and signal-to-noise ratio (SNR) have been retrieved by WP to detect the height of maximum turbulence. Temperature and humidity profiles were used in the parcel method (PM) and bulk-Richardson (bR) method for daytime detection of the CBL and for the SBL detection during the night, where bR was also tested. The aerosol scattering ratio (ASR) provided by the lidar has been used continuously throughout the day to detect the top of the PBL (RL during the night and CBL during the day), associated with a sharp decrease in particles' concentration.

Following the work of Praz, 2013, and Collaud Coen et al., 2014, the next chapters will cover a comprehensive description of the instruments and methodology used; a computation of the errors associated with PBLH detection through propagation of measurement's uncertainties; a comparison between the results provided by each instrument and method, as well as with the PBLH from the COSMO/KENDA model; a 5-year climatology of the PBLH for day and night in clear and cloudy sky conditions; an analysis of the CBL growth rate during the day and finally, a trend analysis on a 30-year RS data set. Strengths and limitations of this work will be discussed in the conclusion. Throughout this study the way each instrument can detect specific sub-layers has been exposed and discussed, as well as the necessity to use jointly several instruments and methods to fully characterize the PBL dynamic. A discussion is also made on the restrictions associated with the instruments, due to weather conditions, vertical resolution and accuracy.

Chapter 2

Experimental

2.1 Measurements sites

The measurements from three stations have been used to perform the PBL analysis, all of which are part of the EMER-Met network (EMErgency-Response Meteorology network for analysis and forecasting in case of nuclear accident (Calpini et al., 2011)): Payerne (490 m a.s.l., 46.812°N, 6.942°E), Grenchen (428 m a.s.l., 47.179°N, 7.415°E) and Schaffhausen (438 m a.s.l., 47.690°N, 8.620°E). These stations are all located on the Swiss Plateau, in rural areas and close to small cities (see Fig. 2.1).

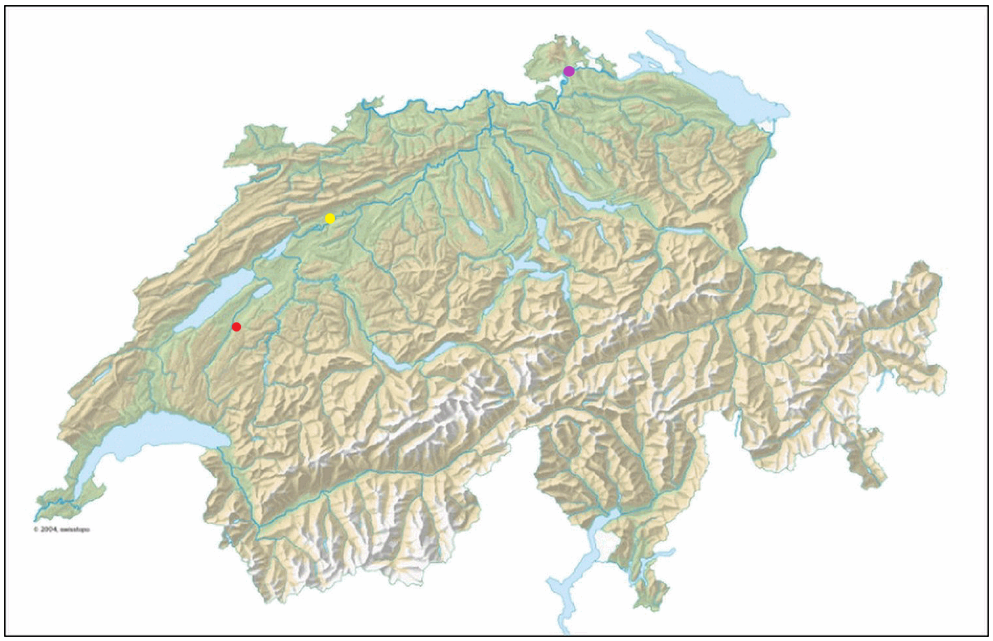

FIGURE 2.1: Measuring sites locations: Payerne is at the red dot, Grenchen at the yellow one and Schaffhausen at the purple one. (Source of the map: www.swisstopo.ch)

2.2 Instruments description and data availability

Several remote sensing instruments were used in this study, with an 11-year data set (2010-2020) for some instruments and 5-year data set (2016-2020) in most cases. The availability of the different instruments and corresponding data sets, in the three stations of interest, has been summarized in Table 2.1 and a short description of each instrument is given hereafter. Finally, time will always be given in Coordinated Universal Time (UTC) in this report. The altitude will be given in meters above sea level (a.s.l.), exceptions are made when citing other studies that may use meters above ground level (a.g.l.). When referring to

instruments coupled with specific PBLH detection method, the following convention will be used: "*Instruments/Method*" (e.g. RALMO/PM, MWR/bR,...).

2.2.1 Microwave radiometer

Microwave radiometers (MWR) are passive remote sensing instruments that measure thermally-emitted electromagnetic radiations from the atmosphere in the microwave spectrum range (1 mm to 1 m or 300 MHz to 300 GHz in frequencies). The absorption spectrum, retrieved at multiple frequencies and angles, is used to derive the brightness temperature via the Planck function. Atmospheric temperature or humidity vertical profiles are then estimated using an inversion method, such as a neural network method, trained with a data set of profiles from radio-sounding (Löhnert and Maier, 2012; Cimini et al., 2013).

MeteoSwiss uses MWR to measure vertical profiles of temperature and humidity in the troposphere. Four radiometers have been rotating in the three stations of interest, two HATPRO radiometers (Humidity and Temperature Profiler) and two TEMPRO (Temperature Profiler), all manufactured by *Radiometer Physics GmbH* (Germany). HATPRO radiometers measure at 14 different channels: 7 in a band between 22 and 31 GHz, for water vapour (humidity) and 7 in a band between 51 and 58 GHz, for temperature. TEMPRO radiometers only retrieve temperature profiles and hence measure in the 7 channels between 51 and 58 GHz. The temporal resolution for the acquisition of profiles is of 10 min while the vertical resolution decreases with altitude, from 50 m at the first altitude levels to 400 m at 4000 m a.g.l. More technical specifications can be found on the manufacturer's website: `https://www.radiometer-physics.de/products`.

Furthermore, the instrument also detects rain and automatically attributes a flag to invalidate the compromised data before storage. Finally, due to the use of some MWR instruments for measurement campaigns across Switzerland, there are missing data in the 2010-2020 timeseries (especially in Grenchen, where there was no operational MWR installed between 2010 and 2014). Further investigations also revealed that MWR data in Payerne were invalidated before 2016, making them unusable for the purpose of this project,

2.2.2 Radio-sounding

Two times a day, at 12:00 and 00:00 UTC, a radio-sounding (RS) is performed with a weather balloon at Payerne, which is also the only sounding station in Switzerland. RS measures the in-situ vertical profiles of temperature, humidity, pressure, wind speed and direction and ozone concentration (only three days per week at midday). The temperature is measured with a platinum resistance thermometer, the humidity with a capacitive hygrometer, the altitude, wind speed and direction are retrieved from GPS measurements and the pressure is estimated from the geopotential height. The rising speed of the balloon is more or less constant (5 m/s) with a maximum altitude of about 30 to 35km before implosion, but for the purpose of this project, only the first 4km were kept. Up to this altitude, we consider that the horizontal displacement of the sounding system will not affect the accuracy of the vertical profile . While radio-sounding provides measurements with high accuracy, two soundings per day are very limiting to draw a complete picture of the PBL dynamic. It however represents a reliable reference for comparison with continuous remote sensing instruments. Additionally, RS measurements are stored back to the middle of XX^{th} century and can be used for long-term trend analysis. Nonetheless, various models of radiosondes have been used throughout time, with different acquisition methods and vertical resolutions (Jeannet et al., 2016). Before 1990, mechanical radiosondes were used, such as the *CH-Vc*, with a vertical resolution of more than 100-150 m. In April 1990, electronic radiosondes were introduced, the first one being a Meteolabor *SRS 400* with a new

vertical resolution of 15-20 m. In 2011, the *SRS 400* was replaced with a *SRS C34*, introducing GPS measurements, with a vertical resolution around 5 m. The *SRS C50* radiosonde was then introduced in 2018 and quickly replaced by the Vaisala *RS41*, that is still in use nowadays.

2.2.3 Raman Lidar (RALMO)

A lidar (light detection and ranging) is an active remote sensing instrument that sends laser beams into the atmosphere and measures the reflected signal, at the surface, from atmospheric molecules or particles. Depending on the characteristics of the measured signal, the humidity, temperature or aerosols dispersal properties can be retrieved from the pure rotational Raman (PRR).

The Swiss **RA**man **L**idar for **M**eteorological **O**bservations (RALMO), installed in Payerne and developed by the Swiss Federal Institute of Technology (EPFL), has been operational since 2008 (Dinoev et al., 2013). In practice, UV pulses (355 nm) are emitted from the laser and the reflected signal is measured with the telescope system, composed of four mirrors of 30 cm in diameter, fiber coupled to the polychromator that spectrally separates the backscattered light. While most conventional lidars can only measure the backscatter coefficient, RALMO retrieves water vapor profiles using vibrational Raman scatter from nitrogen (387 nm) and water vapor (407 nm) signals and T profiles from the PRR signals detected around the 355 nm Cabannes line (Martucci et al., 2021). These signals are then calibrated with RS measurements. This study is one of the first to make use of T and RH profiles retrieve with a lidar to compute the PBLH with conventional T-related detection methods.

The first range is located at 160 m a.g.l, with a maximum range varying from 5000 m a.g.l during the day to around 9000 m a.g.l at night. The vertical resolution is fixed at 30 m throughout the whole profile. The temperature, specific humidity, aerosol backscattering and scattering ratio profiles are retrieved with an effective time resolution of 30min (averaged profiles over 30min). In case of rain or low cloud cover, the signal is shut down and no data are hence retrieved. Due to an instrumental failure, RALMO seized to function from July 2020 to July 2021 (could not be repaired sooner due to Covid-19 restrictions).

Martucci et al., 2021, performed a complete validation of the temperature data from Ralmo against two reference radio-sounding systems. However, due to an error in the homogenisation of humidity and T profiles, RALMO data are presently unusable before 2016, except for the Aerosol Scattering Ratio (ASR) that is correctly stored in the data bank and available from 2010 to 2020.

2.2.4 Wind profiler

A wind profiler (WP) is an active remote sensing instrument that measures vertical profiles of the radial wind components (speed and direction) up to several kilometers, depending on the wavelength used and the meteorological conditions. Turbulent structures in the atmosphere, also referred as eddies, travel with the wind (or at least the assumption is made that they do). When the emitted signal from the WP antennas hits these structures, the signal is backscattered and measured by the instrument's receptors at the ground. The radial velocity of these turbulent structures is then derived based on the shift in frequency between the emitted and received signal, according to the Doppler effect. The elapsed time between emission and reception of the signal is used to determine the range in the vertical profile.

In Switzerland, three WP are installed, one in each station of the EMER-Met Network (Pay, Gre and Sha) with continuous available measurements for the period of interest. All

three stations have the same WP model: the PCL-1300, manufactured by *Degréane* (France) and running at 1290 MHz ($\lambda = 23.3$ cm). This model operates with five antenna to recover all radial components of the wind. One has a vertical inclination to measure the vertical wind velocity and the four others are titled by a 17° angle relative to zenith, in the four orthogonal directions, to measure the horizontal components. The instruments are operated in a low and high mode with a vertical resolution of approximately 58m and 144m and a range between roughly 100-3000 m a.g.l and 300-8000 m a.g.l, respectively. The effective time resolution is of 10 min for both modes. In this study, only the low mode has been used.

In addition to the computed wind components (based on Doppler effect), the internal software of the instrument also computes the vertical profile of the signal-to-noise ratio (SNR) by taking the minimum SNR value from the five antenna (Collaud Coen et al., 2014). A quality check is further performed before storing the data, to eliminate the data for which the Doppler shift peak is not strong enough to derive a wind speed (Praz, 2013). Furthermore, Haefele and Ruffieux, 2015, performed a full validation of the 1290 MHz PCL-1300 WP against radiosonde GPS wind measurements.

Finally, WP is a very useful instrument since it works under all weather conditions (cloudy situation, rain, snow, etc) and is hence widely used in various operational meteorological applications, such as nuclear power plant surveillance (Calpini et al., 2011), or like it is done in this project, PBLH detection. However, this instruments is very sensitive to noise generated on the ground and surrounding terrain (ground clutter), this is why a metallic fence is often found around WP, to mitigate the effect of this noise. Also, during the night, the more stable and stratified atmosphere near ground leads to weaker turbulent structures hardly detected/measured by the WP. Ultimately, the amount of data available near ground, at night, is greatly reduced. This behaviour is also observed, to a lesser extent, during the day, in conditions of weak instability. Wilczak et al., 1995, also showed that mass migration of birds could greatly influence the measurements of WP at night during the migration seasons (spring and autumn).

2.2.5 SwissMetNet

SwissMetNet (SMN) is the Swiss meteorological network, composed of about 260 automatic measurements stations dispersed across the country. A variety of atmospheric parameters are measured at these stations, including ground temperature, humidity, atmospheric pressure and radiation, at 2 m a.g.l. The wind speed and direction are also measured, at 10 m a.g.l. For this project, the measurements from the SMN stations of Payerne, Grenchen, Schaffhausen and Koppigen (for APCADA in Grenchen, see Sect. 2.2.7) were used, with a time resolution of 10min and no interruption in the data availability throughout the years.

2.2.6 Ceilometer CL31

A ceilometer is a lidar specifically designed to retrieve the cloud base height. The laser beam wavelength (910 nm) is chosen so that the measured backscattered signal comes from water droplets (in the clouds). A network of Ceilometers CL31, manufactured by *Vaisala* (Finland) provides three cloud layers heights (up to 7.6 km) for the 35 measurements stations of the REGA network (Hervo, 2020). The entire backscattering profile is also retrieved by the CL31 at Payerne (and in most of the 35 stations). CL31 ceilometers are installed in all three stations of interest of this project and were used as criterion to remove situations of cloudy conditions for some PBLH detection methods (ASR and SNR).

2.2.7 APCADA

The Automatic Partial Cloud Amount Detection Algorithm (Bruno and Philipona, 2004) was used in this project to differentiate between clear and cloudy sky conditions (see Sect. 3.4). APCADA uses measurements of longwave downward radiation (LDR), temperature and relative humidity from the SMN stations to estimate the cloud coverage (in [okta]), with a time resolution of 10 min. This algorithm has the disadvantage that high cloud radiating at temperature near the background one (cirrus clouds) are not detected (Pasquier, 2018).

Furthermore, while data are available between 2010 and 2020 in the stations of Payerne and Schaffhausen, there are no LDR measurements at the Grenchen automatic measurements station. We hence decided to use the APCADA data from the Koppigen station, located east of Grenchen at less than 20 km and with an altitude of 485 m (also available between 2010 and 2020). This station has a very similar geographical position and this approximation should only have a negligible influence on the clear/cloudy sky differentiation process.

2.2.8 COSMO model with KENDA data assimilation

Additionally to the instruments cited before, PBLH results from the COSMO-1E and COSMO-2E (Consortium for Small-scale Modeling: `http://www.cosmo-model.org/`) model were also used, as a basis for comparison. The PBLH timeseries, available at all three stations of interest, continuously between 2016 and 2020, were computed with the KENDA (Kilometre-scale Ensemble Data Assimilation) system, for which radio-sounding, aircraft, wind profiler and surface station data are assimilated in the COSMO-E model to enhance the prediction performance (Schraff et al., 2016). The data are available at a time resolution of 1h and the bulk-Richardson number method (see Sect. 3.1.2) with modelled virtual potential temperature profiles is used to retrieve the PBLH. Vertical interpolation is used to retrieve the correct PBLH between two levels of vertical resolution. The assimilated measurements at one point of the grid (e.g. sounding in Payerne) also influence the others points of the grid with decreasing magnitude when increasing distance to the data source.

	Pay	Gre	Sha
APCADA	2010-2020	- Koppigen (2010-2020)	2010-2020
CL31	2018-2020	2016-2020	July 2016-2020
KENDA	2016-2020	2016-2020	2016-2020
MWR	2016-2020	2013-2017 2019-2020	2010-2020
RALMO	2010- July 2020 (ASR) 2016- July 2020 (T, RH)	-	-
RS	1991-2020 (trends)	-	-
SMN	2010-2020	2010-2020	2010-2020
WP	2010-2020	2010-2020	2010-2020

TABLE 2.1: Summary of instrument's and data availability in the three measuring stations of interest. The "-" symbol means that this instrument is not available for this station. Note that for some REM instruments, data may be available before 2010, but without interest for this project.

2.2.9 Instrument errors

The errors on each variable must be defined the same way for consistency in the error propagation procedure. Hence, they were defined as the standard deviation of the bias between the instrument's measurement and the one from radio-sounding data sets, based on various studies. These values were then used as constant errors along each T, RH and p profiles and are available in Table 2.2. There exists, for now, no other common definitions of the variable's errors for MeteoSwiss' remote sensing instruments.

	MWR	RALMO	RS	SMN
Temperature	1 K (Martinet et al., 2015)	0.6 K (Martucci et al., 2021)	0.15 K (Jeannet, 2018)	0.15 K (internal: L.Modolo, 01/04/21, Payerne)
Humidity	0.5 g/kg on **mmr** (Martinet et al., 2020)	Relative uncertainty (Martucci et al., 2021)	3 % on **RH** (Jeannet, 2018)	3 % on **RH** (L.Modolo)
Pressure	-	-	0.4 hPa (Jeannet, 2018)	0.15 hPa (L.Modolo)

TABLE 2.2: Standard deviation of the bias between the instrument's measurements and the sounding. RS is compared with other models of radiosondes to establish the bias.

Chapter 3

Methodology

3.1 Methods based on temperature-related profiles

The potential temperature θ is defined as the temperature that an hypothetical air parcel at altitude z, temperature $T(z)$ and pressure $p(z)$ would have if brought adiabatically to a reference level with pressure p_{ref} (Eq. 3.1):

$$\theta(z,p) = T(z)\left(\frac{p_{ref}}{p(z)}\right)^{\frac{R}{M_a c_{pa}}} \simeq T(z)\left(\frac{p_{ref}}{p(z)}\right)^{0.286} \tag{3.1}$$

where M_a is the molar mass of dry air, g is the Earth gravitational acceleration, R is the molar gas constant and p_{ref} is the pressure at reference level. In this work, we set p_{ref} equal to 1013.35 hPa, which is the atmospheric pressure at mean sea level. Apart from being an important variable for determining the PBLH, θ is also useful to quickly assess the stability of the atmosphere: $\partial\theta/\partial z = 0$, $\partial\theta/\partial z > 0$ and $\partial\theta/\partial z < 0$ for neutral, stable and unstable atmosphere, respectively. Indeed, for a positive gradient, the parcel will have a temperature superior to that of the surrounding air and will hence adiabatically rise, causing instability in the atmosphere. Oppositely, a negative gradient will lead to adiabatical sinking of the parcel and a stable atmosphere. Finally, a vanishing gradient means that the parcel will always be at the same T than the surrounding air and will neither rise or sink (neutrality).

While θ assumes dry air conditions, it may be important to account for moisture in the air. As moist air is lighter than dry air at the same temperature, the buoyancy of a moist air parcel is ultimately increased. One can correct the potential temperature for moisture into the virtual potential temperature θ_v, defined as follow (Eq. 3.2):

$$\theta_v = \theta(1 + 0.61r) \tag{3.2}$$

where r is the mass mixing ratio of water vapor. The stability of the atmosphere can be assessed the same way with θ_v and θ and all the PBLH detection methods described hereafter in Sections 3.1.1 to 3.1.3 were applied similarly on θ and θ_v.

We saw in Eq. 3.1 that the pressure profile is needed while computing θ and θ_v. This variable is not measured by the instruments and needs to be approximated from the temperature profile using the following assumptions: air is considered a perfect gas and the atmosphere is in hydrostatic equilibrium. The pressure profile can then be approximated as follow (Eq. 3.3):

$$p(z,T) = p_0 \cdot exp\left(-\int_{z_0}^{z} \frac{M_a g}{RT(z')} dz'\right) \tag{3.3}$$

where p_0 is the pressure at ground, measured at the SMN stations.

3.1.1 Parcel Method

The parcel method (PM) (Holzworth, 1964) was developed to retrieve the CBL height (CBLH) from either temperature or potential temperature profiles. In this study, we chose to apply this method on the potential temperature as the detection is more straightforward.

With this method, the CBLH is computed based on the hypothetical vertical displacement (adiabatical rise by convection) of an air parcel in an unstable atmosphere. The parcel rises from the surface to the altitude at which its temperature equals the dry adiabate, or its potential temperature equals the one at the ground (Seidel et al., 2010). At this altitude, the parcel (that was originally warmer than the surrounding air at the ground) is at equilibrium with the surrounding atmosphere and will rise no further. This method hence requires that the atmosphere is unstable, as an air parcel could not adiabatically rise in stable conditions.

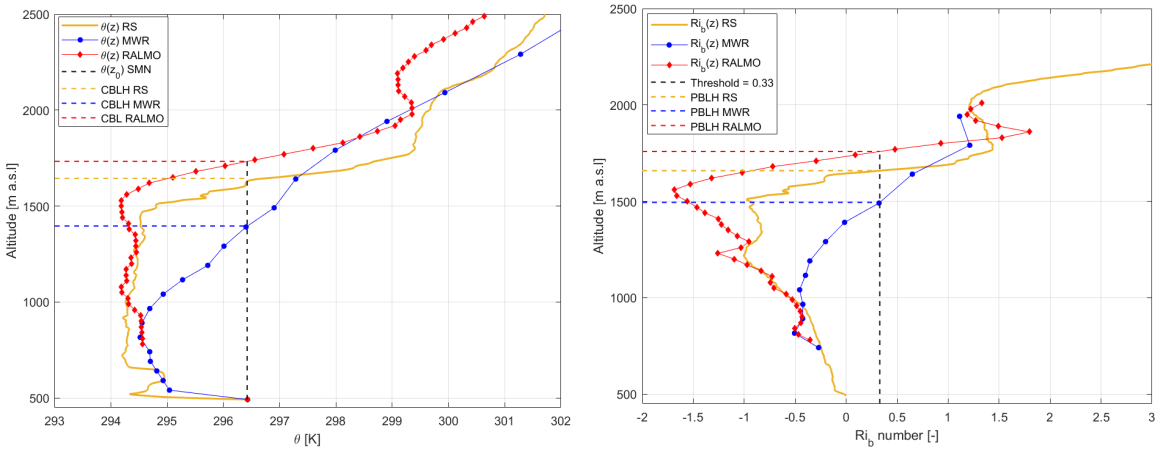

(A) Parcel method

(B) Bulk Richardson number method

FIGURE 3.1: Graphical illustration of the parcel method (A) and bulk Richardson number method (B), applied on RS (yellow), MWR (blue) and RALMO (red) temperature-related profiles on the 26^{th} of May 2020 at 11:30 in Payerne. The PM (bR) CBLH are found at approximately 1400 (1500) m a.s.l. for MWR, 1650 (1660) m a.s.l. for RS and 1730 (1760) m a.s.l. for RALMO. Note that for the two methods, the ground value is from SMN measurements at 2 m a.g.l.

In practice, the algorithm first determines if the atmosphere close to the ground is unstable ($\theta(z_1) < \theta(z_0)$). We hence only retrieve time steps comprised between sunrise and sunset, +/- 2 hours, as there is usually no unstable conditions during the night. The profile is then scanned to find the altitude at which $\theta(z)$ is equal to $\theta(z_0)$. If this value is between two levels of vertical resolution, a linear interpolation is performed with the neighboring values to retrieve the correct altitude. A graphical representation of this method is given in Figure 3.1a. Note that the temperature measured by the MWR is higher than with RALMO or RS, resulting in a lower CBLH detection. This will be further examined in Sect. 5.3.

One of the core variable to this method is the ground temperature, as the final computed CBLH directly depends on it. For the MWR and RALMO, there are no measurements at ground, it is for this reason that we chose to take the ground temperature (and humidity for θ_v) from the precise SMN instruments at 2 m a.g.l. For better consistency between the instruments, the ground measurements from the radio-sounding were also replaced with the SMN ones.

3.1.2 Bulk Richardson Number Method

The bulk Richardson number Ri_b is a dimensionless number that represent the ratio between thermally/convective produced turbulence and those produced by vertical shear (Sivaraman et al., 2013). To be consistent with the Ri_b used in the COSMO-E (KENDA) model (Szintai, 2010; Schraff et al., 2016), the following expression has been used (Richardson et al., 2013):

$$Ri_b = \frac{gz(\theta(z) - \theta(z_0))}{\bar{\theta}(U^2(z) + V^2(z))} \tag{3.4}$$

where g is the gravitational acceleration; $\theta(z)$ and $\theta(z_0)$ are the potential temperature at altitude z and at the ground, respectively; $\bar{\theta}$ is the mean θ between z and z_0 and $U(z)$ and $V(z)$ are the horizontal wind speed components at altitude z. For MWR and RALMO, the wind speed is taken from the WP measurements while RS has its own wind speed measurements (based on GPS positioning).

The PBLH is computed as the elevation z at which the bulk Richardson number equals or exceeds a defined threshold. In the literature, this threshold is most often set between 0.15 and 0.40 (Jeričević and Grisogono, 2006; Sivaraman et al., 2013; Zhang et al., 2014), depending on the stability of the atmosphere, the hour of the day, the surface roughness, etc. Again, to be consistent with the COSMO-E model, we chose to set these thresholds to 0.22 for stable conditions during the night and 0.33 for unstable conditions during the day. Furthermore, this method assumes that there are no turbulence production above the top of the mixing layer so that Ri_b exceeds its threshold at the top of this layer.

The algorithm is very similar to the one used for the parcel method. Indeed, if we set the threshold to 0, one solution of the equation Ri_b=0 is given by $\theta(z)$=$\theta(z_0)$, which correspond to the PM. However, because of the positive threshold applied to bR, this methods almost always yields higher PBLH than with PM and requires no condition on the stability of the atmosphere. Hence, this method also theoretically works during the night, for conditions of weak stability. The profile is then scanned until the threshold is exceeded, and a linear interpolation between neighboring levels is performed to retrieve the altitude at which Ri_b is equal to the threshold. However, due to missing data points in the WP wind profiles (see Sect. 2.2.4), it may happens that some Ri_b values, before the threshold is exceeded, are missing (NaN's). This only happens for RALMO and MWR (which use WP wind data into computing Ri_b), mostly during the night and, more rarely, during the day. In this case, a linear interpolation with the last non-NaN value may be tricky and generate a large error in the PBL height determination. We hence decided to interpolate only if the last non-NaN value was less than 400 m bellow. This leads to a high amount of missing points during the night and, to a lesser extent, during the day. For the KENDA values (from COSMO-E model), the PBLH were computed using the Ri_b with θ_v, as mentioned in Sect. 2.2.8. A graphical illustration of this method is given in Figure 3.1b, for which we can see the missing data points close to the ground due to a lack of WP wind data. The measured CBLH is also higher with bR than with PM, as expected.

3.1.3 SBLpt and SBI detection

During the night, the ground-based temperature inversion height (SBI) and the stable boundary layer (SBL) height, retrieved with the potential temperature profile (SBLpt), are computed. In practice, we allow these computations for time steps comprised between sunrise and sunset +/- 3 hours, so that the full rise and decline of the SBI and SBLpt are also retrieved.

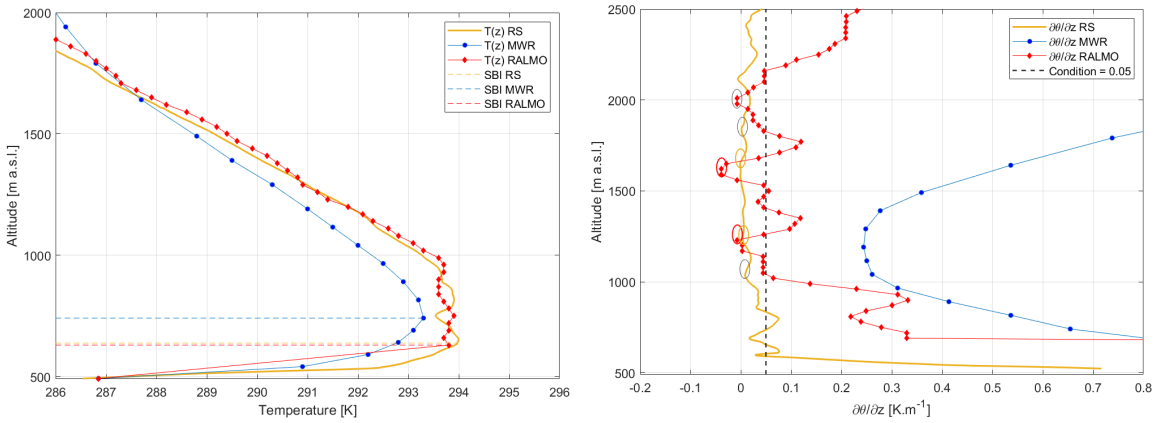

(A) SBI: T profiles.

(B) SBLpt: θ gradient profiles.

FIGURE 3.2: Graphical illustration of the SBI detection method (A) and SBLpt detection method (B), applied on temperature related profiles on the 10th of September 2018 at 23:30 in Payerne. For the SBI, the dashed lines correspond to the heights of the SBI, altitudes at which the temperature profiles start to decrease. For the SBLpt, 2 peaks are kept for RS and RALMO (yellow and red circles respectively) while 2 others are discarded (dark grey circles) to keep only two finals SBLpt heights; no peak meeting the conditions is found with the MWR profile.

SBI: The algorithm first checks if the temperature is increasing close to the ground ($T(z_1) > T(z_0)$). Then, it finds the altitude at which the temperature starts to decrease ($T(z_{i+1}) < T(z_i)$) and set it as the SBI (see Fig. 3.2a). The vertical resolution has a big impact on the computed SBI height, where small variations (with RS and RALMO) result, wrongly, in a lower SBI. An alternative algorithm could be imagined to tackle this problem. However, it remains unclear if one should decide to put the SBI height where the T profile becomes monotonically decreasing (at about 900 m a.s.l. for RALMO and RS in Fig. 3.2a) or if the profiles should be smoothed until only an unique change of slope is observed. The error introduced in this decision-making process may be far greater than the error already introduced in this method due to vertical resolution.

SBLpt: First, the derivative of the θ profile is computed using a smooth polynomial interpolation, the Savitzky-Golay filter. The SBLpt is set as the height at which the derivative becomes null (i.e. where the θ profile stabilizes). In practice, the derivative does not always reach zero in the profile but might get very close to it. This is why we extracted all the local minimum peaks in the derivative with the following conditions: the derivative should be smaller than 0.05, two locals peaks should not be separated by less than 250m and finally, the maximum height for finding a local peak is set to 2500m. It is important to say that there is usually only one peak that meets these conditions with the MWR, as its vertical resolution is insufficient to find other stability heights. However, many peaks meeting the conditions mentioned above are found while using Ralmo or RS θ profiles, due to their high vertical resolution (see Figure 3.2). In this case, we only kept the two strongest peaks (with smallest values of derivative) and chose the one at lowest altitude as SBLpt. To avoid having too much peaks for RS, due to the very high vertical resolution of this instrument, the theta profiles were smoothed beforehand with the same Savitzky-Golay filter that is used to compute the derivatives.

3.2 Method based on concentration profiles

As mentioned in Sect. 2.2.3, RALMO provides a full aerosol scattering ratio (ASR), which is the ratio between the total and molecular backscatter coefficients. While the concentration of aerosols within the PBL is rather high, the top of the PBL is characterized by a sharp decrease in aerosol concentration before the free troposphere. By setting the PBLH as the absolute minima in the ASR's gradient, we expect to find the CBLH during the day and the RL height during the night. In practice, the algorithm does not necessarily set the absolute minima as the CBLH/RL, as a time continuity criterion is applied (Collaud Coen et al., 2014). The k ASR peaks ($s_{k,i}$) at time i, with local minimum lower than 10% of the absolute minima are kept as possible candidates. A Gaussian function $g(h_{i-1}, \sigma)$, with a mean equal to the PBL height at previous time step h_{i-1} and a standard deviation σ depending on the number of preceding NaN's, is used to weight the $s_{k,i}$ peaks. The PBLH is then chosen as the minimum of the weighted ASR peaks (see Figure 3.3).

To avoid setting the PBLH to the cloud top height (altitude at which a strong decrease in the ASR is also observed), we constrained the search for PBLH at time steps without continuous cloud cover, detected by the ceilometer CL31, during RALMO acquisition time (30min). However, the ceilometer has been installed in 2018 in Payerne, so that this correction was only applied after this date.

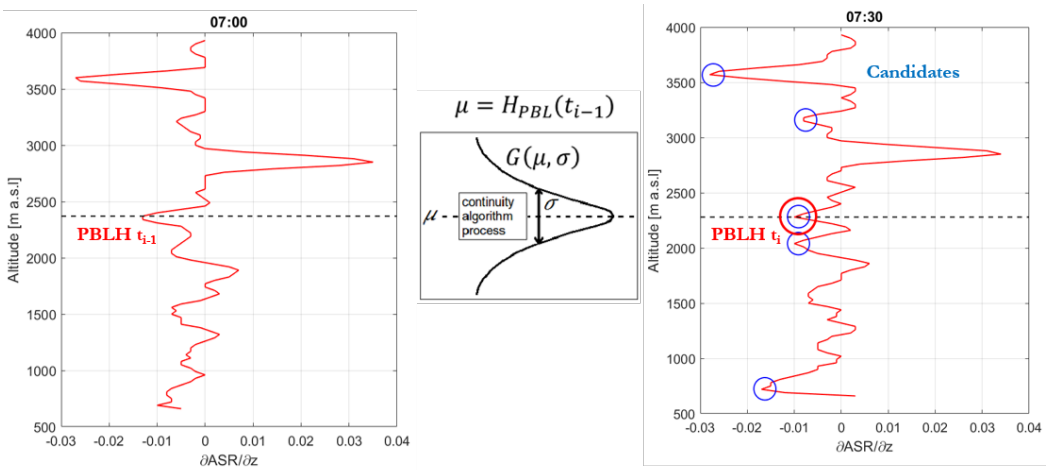

FIGURE 3.3: Continuity algorithm applied on a RALMO/ASR profile from the 2^{nd} of June 2020.

3.3 Method based on wind turbulence profiles

The method used to determine the PBLH, based on the Signal to Noise Ratio (SNR) of the WP, was developed by Liu et al., 2019: the normalized SNR threshold method. A different approach was used by Praz, 2013, and Collaud Coen et al., 2014. Their method was similar to the one applied on RALMO/ASR, taking the maxima of the weighted SNR peaks instead and with the modified condition that the chosen maxima had to be greater than 75% of the absolute maxima. Unfortunately, part of the CBL growth was missing in this method due to the continuity criterion.

The SNR profile is first normalized by its maximum so that all values in the profile are between 0 and 1, using Equation 3.5.

$$SNR_{norm} = \frac{SNR}{max(SNR)} \tag{3.5}$$

The normalized profile is then scanned vertically from ground to find the first value equal to 1 (maximum). We then search above it for the first value equal to a certain threshold. This threshold is set to 0.75 during daytime and 0.9 during nighttime. These values were chosen so that the presence of humidity gradients embedded in the PBL would not directly influence the peak detection of the algorithm, as they may enlarge the extent of measured maximum of turbulence (Compton et al., 2013). If the threshold is met between two vertical levels, we use a linear interpolation with the neighbouring values to retrieve the correct PBLH altitude.

Note that, similarly to RALMO/ASR, SNR is greatly affected by the presence of cloud, so that this method may set the PBLH to the cloud top height in these conditions. Hence, we decided to remove the PBLH where clouds where detected simultaneously by the ceilometer CL31. Again, these instruments were installed in 2018 in Payerne and in 2016 in Grenchen and Schaffhausen, so that this correction was only applied after these dates.

3.4 Clear/cloudy sky differentiation

A flagging system, for cloud coverage classification, has been developed using APCADA data (see Sect. 2.2.7). This process is necessary for a more accurate comparison and description of the results, as the PBL behaviour will vary significantly from a cloudy day to a cloud-free one. For flag's attribution, nights have been separated in two time classes to account for big weather changes during the night: the morning night is comprised between midnight and the sunrise while the evening night is comprised between sunset and 23:59. For daytime, the flag was attributed based on the average CBL growth time, between sunrise + 2h (set to 09:00 if "sunrise + 2h" exceeds 09:00) and 2pm and then assigned to all data between sunrise and sunset.

Moreover, a clear sky flag correspond to a situation with 2 or less than 2 okta, 75% of the time, while a situation with 1 or less than 1 okta, 95% of the time, is flagged as "very clear sky". A cloudy flag is attributed for situations with opposite conditions to the clear sky ones and is further defined as "very cloudy" for situations with 7 okta or more, 80% of the time.

3.5 CBL growth rate computation

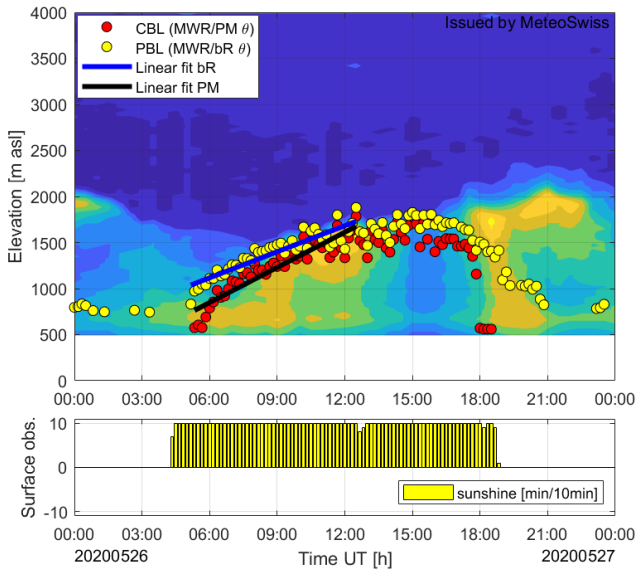

FIGURE 3.4: Linear fit applied on MWR/PM and MWR/bR, between t_1 and t_2, for a clear convective day of May 2020 in Payerne. The background signal is from RALMO ASR.

The growth rate [m/h] of the convective boundary layer (CBL) was computed using a conventional method of linear fit (Pal and Haeffelin, 2015; Moreira et al., 2020; Baars et al., 2008). In this method, the growth rate is defined has the slope of the linear fit between two characteristic times t_1 and t_2 (Fig.3.4), where t_1 correspond to the time of the first detected CBLH after sunrise and t_2 to the time at which the CBLH daily maximum value is found (some of the researches cited before used 0.9% of the CBLH daily max). In most cases, the linear approximation holds and the error introduced is small. In this study, we also chose to constrain the research of the daily maximum CBLH before 14:00, preventing afternoon outliers, due to clouds, to be considered as daily maximum.

3.6 Trend computation

PBLH long-term trend analysis was performed on RS measurements at 11:30. A data set from 1991 to 2020 was used with PM and bR, for a total of 30 years. Two methods were tested, parametric and non-parametric, to assess the trends and their statistical significance.

3.6.1 Non-parametric method

Seasonal Mann-Kendall test (sMK): The Mann-Kendall test, being a non-parametric methods, requires no conditions on the data distribution but must however be applied on a serially independent and homogeneous data set. The latter condition of homogeneity is not met when a seasonality is present, which is the case for PBLH measurements as it will be seen later. This problem can be solved using the seasonal Mann-Kendall test (Hirsch et al., 1982), where each season is treated separately. The global trend can then be recovered, only if seasonal trends are homogeneous. The former condition of independence is not met with autocorrelated data, that may in turn lead to type 1 and type 2 errors in the validation/rejection of the null hypotheses H_0: "*absence of monotonic continuous trend*". Collaud Coen et al., 2020a, proposed a set of 3 prewhitening methods to overcome this problem and remove data autocorrelation. First, two prewhitening methods, the standard prewhitening methods, which removes the lag-1 autocorrelation, and a trend-free, which removes the trend before to compute the lag-1 autocorrelation, were used to determine the significance of the sMK-test. Finally, the Sen's slope is estimated with a variance-corrected trend-free prewhitening method, where the variance of the original data set is restored to the trend-free time series. The combination of these methods limits, to some extent, type

1 and 2 errors and results in more accurate and robust slope estimators. In this report, the statistical significance of the sMK-test has been taken at 90% of the confidence interval.

To compute the trends for various period length and assess the trend modification with time, every possibilities were tested, with window size from 10 to 30 years (with 1-year increment) and starting years from 1991 to 2011.

3.6.2 Parametric methods

Least Mean Square analysis (LMS): Parametric methods can also be used to compute seasonal or yearly trends. These methods however necessitate normally distributed data of the residues. This is, to some extent, the case for PBLH computed with PM and bR using RS, so that no transformation of the data were needed. The least mean square analysis is performed, following the Weatherhead procedure (Weatherhead et al., 2000; Collaud Coen et al., 2020b), on monthly median of RS/PM and RS/bR. The data are fitted with the following statistical model (3.6):

$$Y_t = m + C_t + \rho \cdot (t/12) + M_t, \quad t = 1, ..., n \tag{3.6}$$

where m is a constant, C_t is the seasonal component (sum of *sinus* and *cosinus*), ρ is the yearly trend's magnitude and M_t is the white noise accounting for data autocorrelation.

Similarly to what was done for the sMK-test, every combination of window size (from 10 to 30 years) and starting year of computation (from 1991 to 2011) was tested, with statistical significance of trends set to 90% of the confidence interval.

Chapter 4

Error computation

4.1 Calculation of uncertainties

4.1.1 Error propagation

For a variable y calculated using variables a and b with absolute uncertainty equal to Δa and Δb respectively, the propagation of these errors on y is defined by the following equation:

$$\Delta y \approx \left|\frac{\partial y}{\partial a}\right| \Delta a + \left|\frac{\partial y}{\partial b}\right| \Delta b \tag{4.1}$$

The detailed computation of errors propagation into all variables (p, θ, θ_v, bR_i, etc) is given in Appendix A, Sect. A.2. The variables' errors (see Table 2.2) are constant on the profile and the propagation is only performed on T-related profiles and methods. For PM and bR, a superior and inferior error is associated with each PBLH. Unfortunately, having a constant error profile on the T profile does not allow to retrieve an error value for the SBI height, as the inversion height is the same when the profile is only shifted positively or negatively. Furthermore, no errors are computed for the SBLpt heights since there are no insurance that the vanishing theta gradients peaks correspond to the same atmospheric behaviour when adding or subtracting the error profiles.

4.1.2 Error computation for PM

1st method: In this method, we first add/subtract the error profile on the measured $\theta(z)$ profile and repeat the PM method (see Sect. 3.1.1) on those modified profiles (see Fig. 4.1a). The error on the SMN T measurement at ground is much smaller than the one attributed to the instrument's measurement. However, using this small SMN T error leads to a superior error profile being stable (instead of unstable), thus making the PM unusable. We solved this problem by replacing the true SMN T error by the same one that is used for the rest of the profile. This error computation method however leads to very small errors on the CBLH, as the $\theta(z)$ profile is only translated by a fraction of Kelvin, plus/minus some variations, as T and p are not constant with altitude.

2nd method: A second method consists in taking the same measured $\theta(z_0)$ on the profiles with errors to retrieve the errors with the PM (see Fig. 4.1b). The upper and lower "neighbours" to the CBLH are chosen as superior and inferior error respectively. We now also ignore the condition of instability, as only the closest neighbours in the error envelop are kept. This method can lead to very large CBLH errors, especially for very steep $\theta(z)$ profiles.

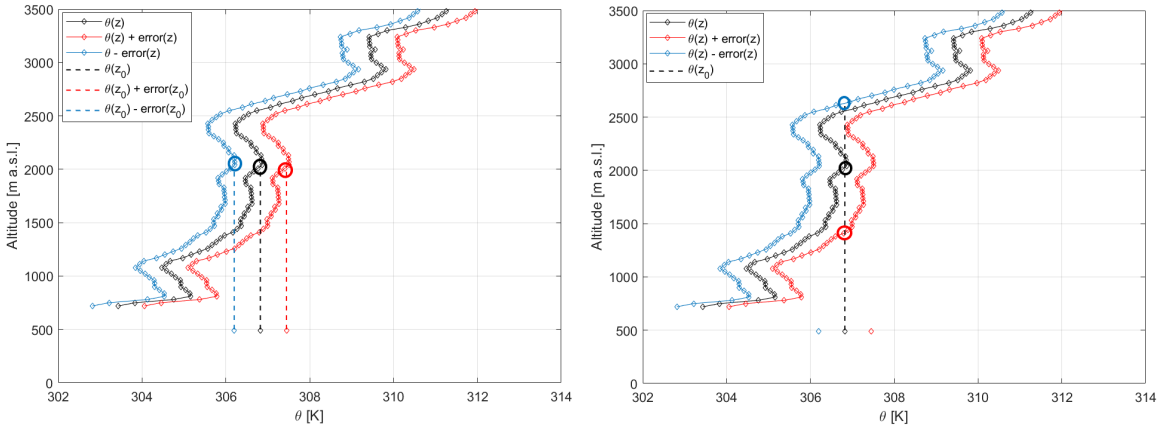

(A) Error computation on PM based on 1st method. (B) Error computation on PM based on 2nd method.

FIGURE 4.1: Graphical illustration of the error computation on PM based on the first method (A) and the second method (B). The profiles used are from RALMO, measured on the 19^{th} of July 2019 at 15:30, in Payerne.

4.1.3 Error computation for bR method

The error computation for the bR method is very similar to the 2^{nd} method applied on PM, where the decisive value is no more $\theta(z_0)$ but Ri_b = 0.22 or 0.33 (Fig. 4.2). Again, only the closest upper and lower neighbours are kept. The resulting PBLH errors are quite large. Furthermore, the errors from radial wind speeds U and V have not been taken into account in the error propagation of Ri_b. Indeed, as this variables appear squared in the denominator of the Ri_b expression (see Eq. 3.4), further elevated to the fourth power in the partial derivatives of the error propagation, the errors will get infinitely large when U and V approach zero. An other approach of the error computation is necessary to deal with this problem.

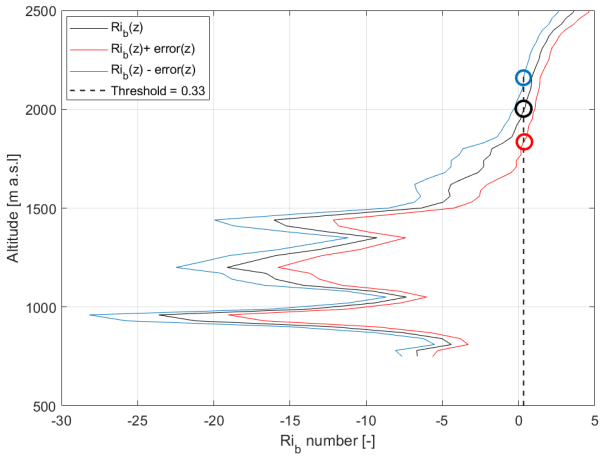

FIGURE 4.2: Graphical illustration of the error computation on bR method, applied on a RALMO Ri_b profile from the 19^{th} of July 2019 at 10:00 in Payerne. The threshold (dashed vertical line) is set to 0.33.

4.2 Errors between 2018 and 2019

To reduce computational cost, the error analysis was performed on a shorter data set from 2018 to 2019. Figures 4.3a and 4.3b show the diurnal variations of the error throughout the months for both 1^{st} and 2^{nd} error computation methods applied on MWR/PM. Here, the error is expressed as the subtraction of the superior and inferior errors. Note the different color scales and their maximum. For the 1^{st} method, this maximum is attained in April, between 14:00 and 15:00, with an error of about 30 m. The errors are also overall greater in mid-afternoon during the summer months, that is, where the CBL is at its maximum

height. After sunrise, and before noon, the computed errors are between 0 and 5 m. These error values are under-estimating what one could expect in terms of transitional width between sub-layers, for the following reasons:

1. The computed errors are smaller than the instrument's vertical resolution (between 50 and 400 m for MWR, depending on altitude).

2. Given the errors associated with the instrument's measurements (see Table 2.2) and the steepness of the profiles, an error of 1 K in the T profile (for MWR) should result in larger errors.

3. The errors are smaller than the depth of the capping inversion and entrainment zone, that was estimated to be between 10 and 40 % of the CBLH (Angevine et al., 1994; Hägeli et al., 2000). Hence, for a CBLH of about 1400 m a.g.l. (summer maximum in Payerne measured with RALMO, Tab. 5.1), the entrainment zone should have a width between 140 and 560 m, which is much more than the error computed here.

For the 2^{nd} method, the maximum is reached in late afternoon ($\sim$ 17:00) when strong instabilities take place and the $\theta(z)$ profile gets nearly vertical, with errors up to 1100 m. In the morning, the error is between 100 and 400 m. This represents between 50% and 100% of the PBLH depending on the season and also exceed the PBLH temporal variability throughout the year, which is thus a clear overestimation of the expected errors. This is for instance much greater than the expected width of the entrainment zone discussed before. Furthermore, in the light of the comparison performed later in this report (Sect. 5.3), where the different instruments/methods agree on the CBLH within 500 m, an error of 1000+ m is probably overestimated. For RALMO, the same behaviour is observed, with smaller maximum errors (20 and 700 m for 1^{st} and 2^{nd} method respectively, see Appendix A, Fig. A.1). This also represent an under and overestimation of the expected errors, following the same arguments presented for the MWR.

The results for the bR method fall in the same range of values than the 2^{nd} method for PM. This is no surprises as these error computation methods are identical and both profiles depend principally on the T error. The error climatology for bR with MWR and RALMO can be seen in Appendix A, Fig. A.2.

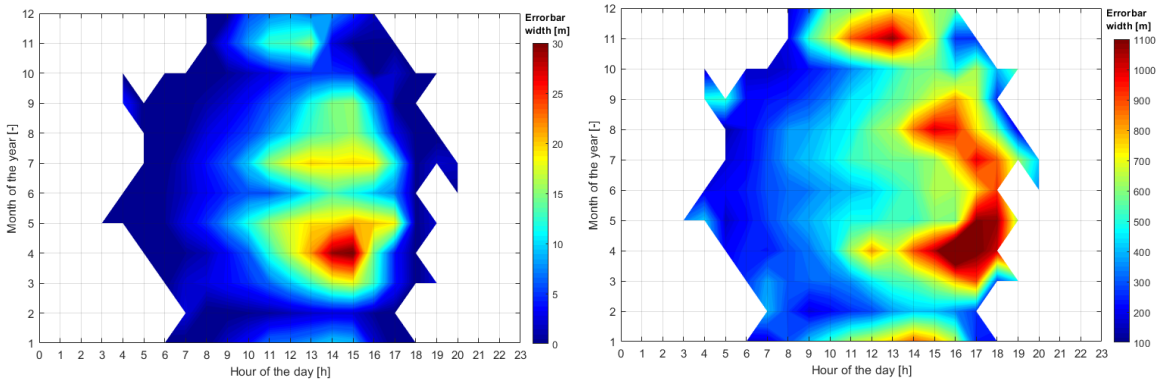

(A) PM based on 1^{st} method.

(B) PM based on 2^{nd} method.

FIGURE 4.3: Climatology of the PBLH error from computation with 1^{st} and 2^{nd} method on MWR/PM, for clear sky conditions in Payerne.

Overall, the error computation methods for PM and bR proposed in this project either under or overestimate what one could expect of the PBL height variations. A different approach is needed, one that would necessitate a common definition of the errors on each

instrument's variable, dependant on altitude and on the acquisition uncertainties. This necessitate a considerable amount of time investment but may benefit to all users of the instruments for further researches. One may also imagine a method based on stochastic generation of profiles to determine the range of uncertainties associated to the PBLH detection. Such work has not been undertaken but represents a great improvement possibility for potential future studies. Instead, most studies treating of the PBLH detection defined the uncertainties as the interquartile range (IQR) of the result's distribution.

Chapter 5

Results and Discussions

5.1 Potential vs. virtual potential temperature

For all T-related methods, both the potential θ and virtual potential θ_v temperature were used. By comparing the PBLH for PM and bR with RALMO and RS in Payerne (Appendix B, Fig. B.1), one can observe a systematic higher PBLH detection using θ_v, with a median bias of $\sim$ 30 m for the entire data set (all data available between 2016 and 2020), regardless of the instrument used. This is due to the fact that moist air is lighter than dry air, allowing deeper convective rise. The PBLH difference using these two variables can however rise to 1000 or even 2000 m in some cases of elevated air relative humidity. For RALMO/PM, only 0.71% of the differences are above 1000 m and 4.1% are above 500 m. These percentages are lower for RALMO/bR and RS. The fitted linear regressions also suggest that the difference between the altitude retrieved with θ and θ_v increases with higher PBLH. Except for the inter-comparison of instruments and methods, θ has been used over θ_v for this study, notably for the greater data availability and reliability of the former.

5.2 Operational and automatic PBLH computation

An automatic procedure retrieves the REM data and applies the methodology described in Chapter 3 to compute the daily PBL heights.

5.2.1 Clear sky condition

An example of such results is given in Figure 5.1, for which the different theoretical PBL layers of a clear convective day (see Fig. 1.1) are retrieved in Payerne. In this figure and all others similar in this report, red, yellow, cyan and blue correspond to the detection methods: PM, bR, SBLpt and SBI respectively; while circles, diamonds, large triangles and small triangles correspond to instruments: MWR, RALMO, RS and KENDA respectively. One can differentiate between three distinctive periods:

Between midnight and sunrise ($\sim$ 06:00): The SBI close to ground is detected by the MWR (blue circles, $\sim$ 600 m a.s.l.) and, at a slightly higher altitude, RALMO (blue diamonds, $\sim$ 750 m a.s.l.). The SBLpt is not retrieved by the MWR here (θ gradient never vanishes along the profiles) and RALMO (cyan diamonds) only exhibits dispersed data points that can hardly be attributed to a continuous stable layer, but are in any case higher than the SBI. At the same time, the bR method applied on KENDA (yellow triangles) retrieves a PBLH at a similar height than MWR/bR (yellow circles), RALMO/SBI and WP/SNR (white squares). Finally, the top of the residual layer, marked by a sharp decrease in atmospheric aerosols' concentration, is retrieved by the ASR gradient method (black diamonds).

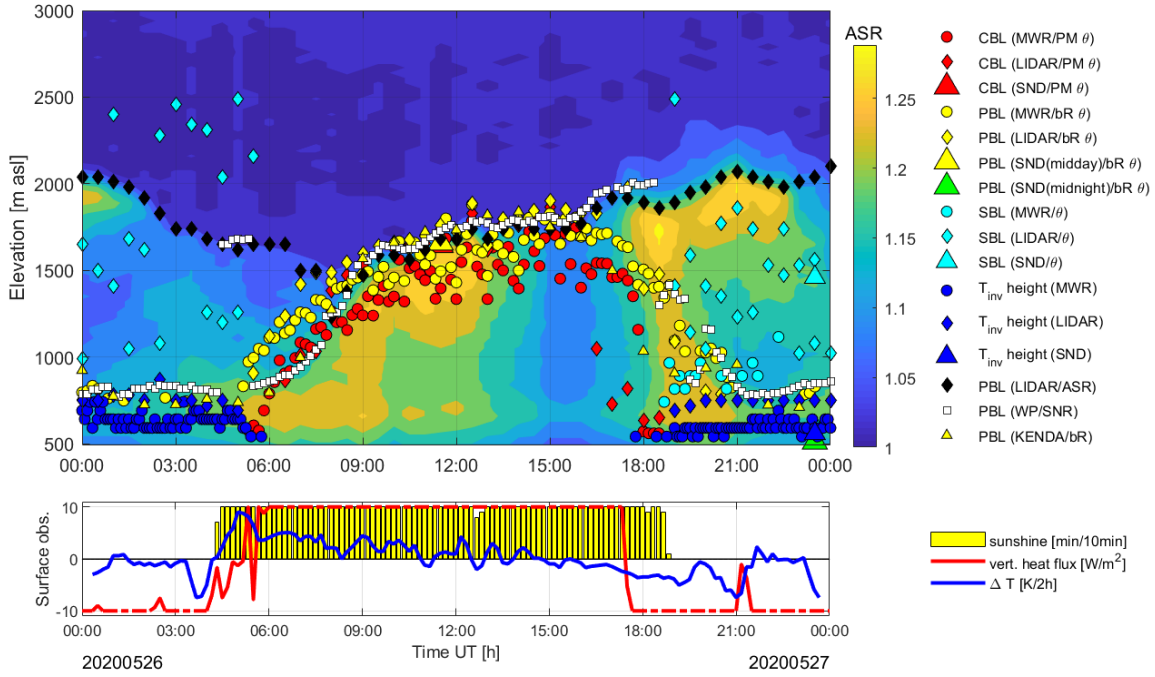

FIGURE 5.1: Upper panel: automatic PBLH detection for all instruments and methods, including KENDA model, for a clear convective day of May 2020 in Payerne; the background signal corresponds to RALMO's ASR. Lower panel: sunshine duration, vertical heat flux and surface T temporal gradient measured by the SMN station for that same day; vertical heat flux greater or smaller than 10 or -10 W/m^2m, respectively, are indicated with a dashed line.

This layer decreases in height (from 2000 m a.s.l. to 1500 m a.s.l.) until it meets the CBL growth after sunrise and start increasing again.

Between sunrise and sunset ($\sim$ 19:00): The CBL growth, from sunrise to about 1pm, is greatly retrieved with all T-related methods. Also note how the starting time of growth correlates with rapid increases in vertical heat flux and surface T gradient. The bR method for MWR and RALMO (yellow circles and diamonds respectively) show higher CBLH heights than with the PM (red circles and diamonds) due to the positive threshold applied on the bR and the consideration of the horizontal wind component. The WP/SNR also reproduces the CBL growth, in a very similar way to the other methods. The radio-sounding at 11:30 (red and yellow large triangles for PM and bR respectively) serves as a comparison to establish that all methods are coherent in terms of timing and values' range, which is here the case. Furthermore, the CBL reaches its maximum height between noon and 15:00 ($\sim$ 1700 m a.g.l.), but the results with the different instruments and methods are more scattered, from one hour to another. It is however worth noticing how RALMO/bR, RALMO/ASR, WP/SNR and KENDA/bR retrieve the same CBLH maxima ($CBLH^{Max}$) between 12:00 and 16:00. A period of stagnation is observed once the maxima is reached, until 17:00, where the vertical heat flux starts decreasing before being negative and where the CBL is ultimately falling, as measured by PM, bR and (with a time delay an to some extent) WP/SNR.

Between sunset and midnight: After sunset, the SBI is well retrieved at $\sim$ 650 and 750 m a.s.l. by both the MWR and RALMO, respectively. Also note how the layer grows, before reaching a maxima around 21:00. For the SBLpt, the MWR retrieves a layer around 900 m a.s.l. These values are lower and less dispersed than the ones retrieve with RALMO.

Indeed, the higher resolution of RALMO leads to several SBLpt layers being detected at once (see Sect. 3.1.3). In general, the SBLpt is found, as expected, at higher altitude than the SBI. Moreover, the midnight RS detects the SBI (blue large triangle) at the same height than the MWR and its bR measurement is almost at ground. Finally, it can also be seen that RALMO/ASR keep on measuring the RL after sunset, while WP/SNR drops around 19:00 to the approximate height of the SBI measured by RALMO (750 m a.s.l., same as in the morning).

5.2.2 Cloudy sky condition

A dry-cloudy day PBLH detection is shown in Figure 5.2, for the station of Schaffhausen. During the night, stable conditions are observed with a continuous cloud base at 1100 m a.s.l. (black stars). During daytime, the atmosphere gets unstable, which allows to retrieve a CBL with MWR/PM, while the cloud base rises to 1300 m a.s.l. Throughout the day, the SBI, SBLpt and PBLH/bR are found at constant heights. The SBI is found at the ground (490 m a.s.l.), the SBLpt is shallow over the SBI ($\sim$ 650 m a.s.l.) and the PBLH computed with KENDA/bR and MWR/bR are slightly above the CBH in the morning, and under after 12:00. In case of high wind speed and weakly stable atmospheric conditions, the Ri_b number might get to a very high altitude before crossing the 0.22 threshold (see Eq. 3.4). The bR method retrieves consequently at night, either a PBLH very close to ground (stable condition, low wind speed) or up high (weakly stable, high wind speed). In this particular case, it corresponds to the cloud base height. Unfortunately, the SNR algorithm necessitate that no continuous cloud cover is present, thus the reason why WP/SNR data points are missing for this day. This was introduced so that the algorithm would not get stuck in the clouds at constant altitude. Here, it is safe to assume that the WP/SNR would have coincide with the bR if it had been computed. Finally, while this kind of weather creates these constant and continuous sub-layers, the cloudy category also includes rainy/snowy days that may greatly influence the PBL detection, leading to the computation of dispersed data points hardly analyzable.

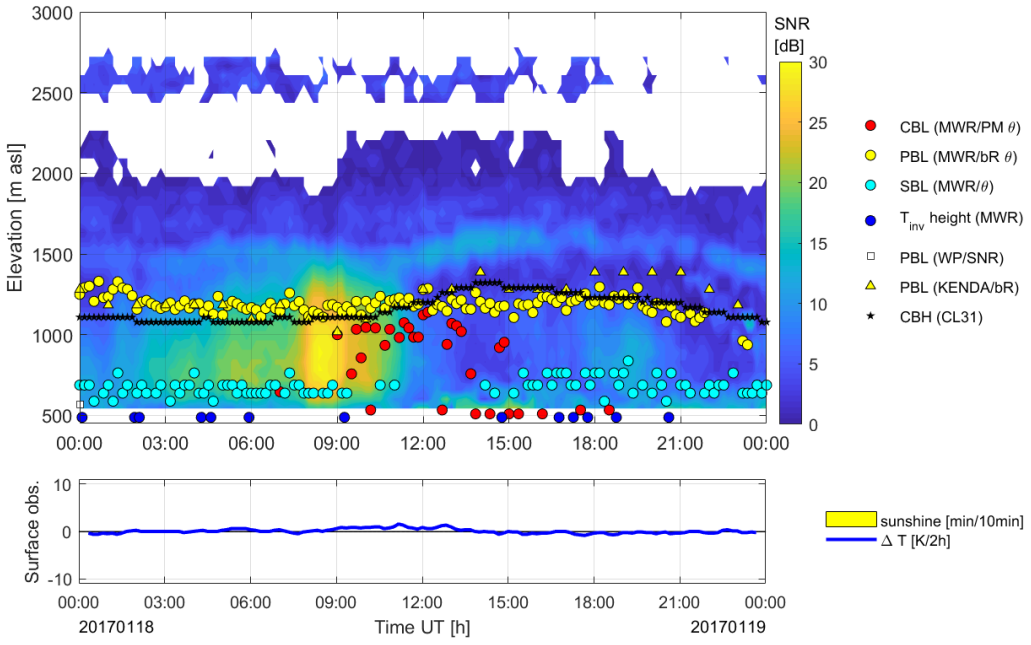

FIGURE 5.2: Automatic PBLH detection for all instruments and methods, including KENDA model, for a cloudy day of May 2020 in Schaffhausen; the background signal corresponds to the WP's SNR. See Fig.5.1 for legend description.

5.3 Comparison instruments/methods

The different instruments and methods used to retrieve the PBLH have been compared with RS/PM from 12:00. For both clear and cloudy sky conditions (Fig. 5.3 and 5.4 respectively), θ_v is used, for consistency with KENDA model. As 12:00 is the RS expected exploding time at maximum height ($\sim$ 30 km), we compare the instruments at 11:30, time at which the profiles of all instruments should roughly correspond to the one of the radiosonde.

As expected, the bR method gives slightly higher PBLH than the PM for all instruments (RS, MWR and RALMO) in both clear and cloudy sky conditions. Furthermore, the PBLH computed with MWR PM and bR is lower (median $\approx$ -250 m and -100 m for clear and cloudy sky conditions respectively) than values computed using RS and RALMO θ_v profiles. It is known (M. Hervo and G. Martucci, personal communication, Jin et al., 2021) that an overheating of the radiometer causes a positive bias in T measurements and ultimately a lower computed PBLH (for an equal $\theta(z_0)$ value, the PBLH decreases if $\theta(z)$ is positively biased). This phenomenon is particularly intense for cloud-free, hot summer months, as it will be discussed later in Sect. 5.4.

For both RALMO and KENDA model, the comparison results in a Gaussian-like distribution, centered around 0, with a reasonable interquartile range (IQR) containing half the data. For RALMO, this IQR is of about 400 m for PM and 350 m for bR; for KENDA a smaller IQR of 300 m is found. This way, these data sets may serve as reference for later comparison. While similar results between RS and RALMO were expected (T profile validation by Martucci et al., 2021), the good fit of the KENDA model for both clear and cloudy sky conditions is more surprising. Indeed, Collaud Coen et al., 2014 showed a global overestimation of the COSMO-2 model. It was later shown by Barton, 2015, that the soil model TERRA was erroneous in estimating ground temperature and humidity. Since then, higher resolved and better quality external parameters such as soil types were used in the model (Marco Arpagaus, Daniel Leuenberger, personal communication). Further studies are nonetheless needed to determine if changes in TERRA are sufficient to explain the better observed PBLH prediction of KENDA.

Finally, RALMO/ASR and WP/SNR are also compared with the noon radio-sounding, despite not being based on T profiles. It is expected that at 11:30, RALMO/ASR measures the top of the CBL with equal values to the other methods. Here, we observe a small underestimation (median $\approx$ - 100 m) compared with RS/PM and a larger IQR ($\sim$ 500 m). Regarding the SNR, the method provides a less accurate height for the CBL (median $\approx$ -250 m) and the IQR is around 600 m. Indeed, the SNR measures the top of turbulent structures, that are not necessarily matching with the CBLH.

Overall, the results are similar in cloudy conditions, but with medians closer to 0 and wider IQRs. While clouds tend to stabilise the atmosphere and favor coherent detection of CBLH by the different instruments and methods, this category also includes a large variety of weather conditions affecting the instruments and detection methods, leading to wider IQRs. Also note that the number of cases in this category is between 1.5 and 2 times larger than in clear sky conditions.

The same comparison is made between RALMO/PM and the other data sets by taking the median PBLH between 12:00 and 15:00. Indeed, the CBLH is not yet at its maximum at the RS time (11:30) so that the median between 12:00 and 15:00 is expected to correspond to the CBLH daily maxima ($CBLH^{Max}$). The results for both clear and cloudy sky conditions are shown in Appendix B, Fig. B.2 and B.3. As one could expect, the result are similar with those discussed above, as the PBLH computed with RALMO T profiles are in the same range of values than the one computed with RS. Also, such comparisons are pointless for

Grenchen and Schaffhausen stations as MWR cannot be used as a reliable reference instrument.
A comparison at night is also irrelevant as the detection methods measure different nocturnal sub-layers of the PBL. Of course, it is possible to compare only pairs of instruments (e.g. MWR/SBI vs. RALMO/SBI), so that these results will be presented later in the climatology analysis (Sect. 5.4).

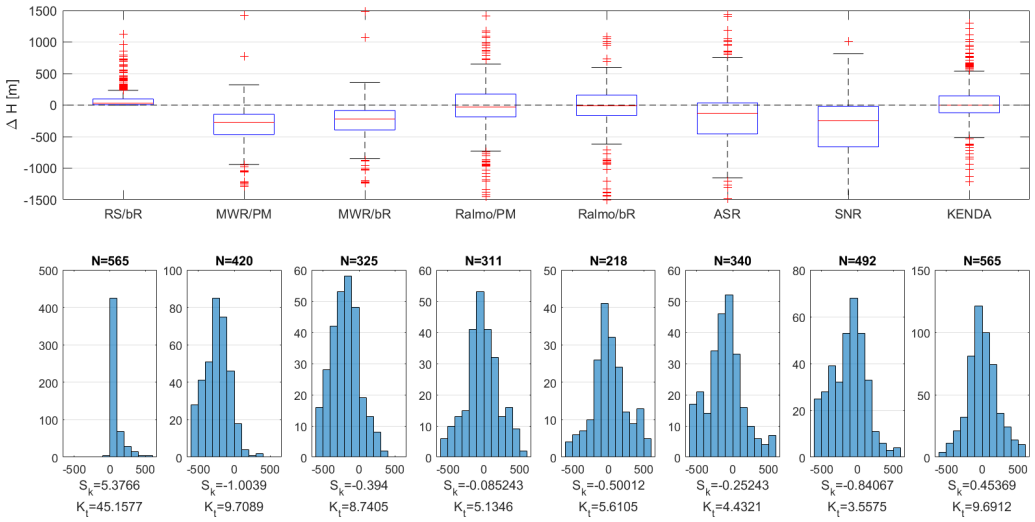

FIGURE 5.3: Comparison between RS/PM and the other instruments/methods at 11:30 between 2016 and 2020 for clear sky days in Payerne ($X(i)$ - RS/PM, where $X(i)$ correspond to each instrument/method pair, θ_v is used for T-related methods). Upper panel: Boxplot representation with the median as the red horizontal line, quantiles 25 and 75% as the lower and upper edges of the box, respectively, lower and upper outlier limits as the black horizontal whiskers and outliers as red crosses. Lower panel: histogram of the comparisons' distribution, the shape is evaluated with the skewness coefficient S_k and the kurtosis coefficient K_t.

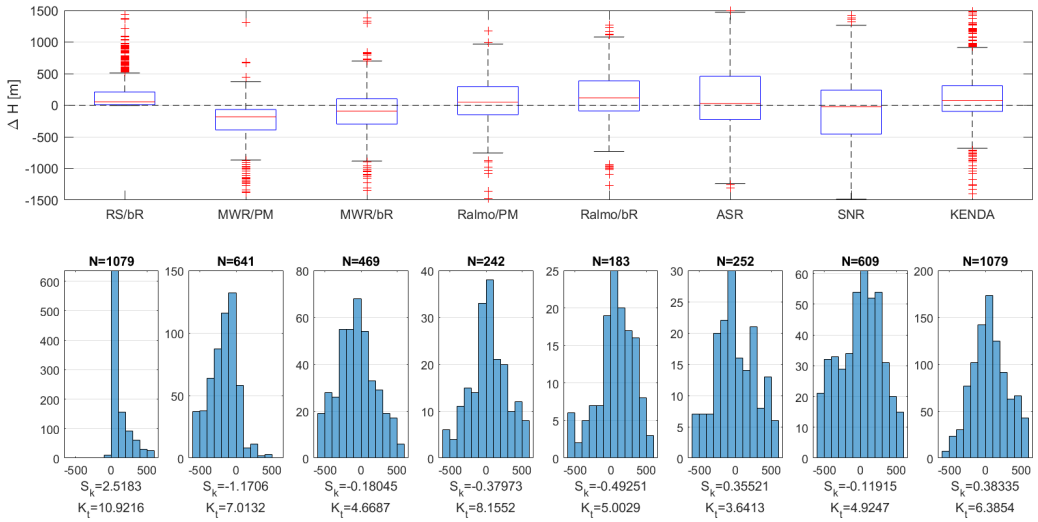

FIGURE 5.4: Comparison between RS/PM and the other instruments/methods at 11:30 between 2016 and 2020 for cloudy days in Payerne. See Fig. 5.3 for legend description.

5.4 Climatology

5.4.1 12:00-15:00 climatology

The 5-year (2016-2020) climatologies of CBLH in Payerne is shown in Figure 5.5 for both clear and cloudy sky conditions. These values are obtained by taking the monthly median of the median between 12:00 and 15:00, which should coincide with the $CBLH^{Max}$. Furthermore, it is required to have at least 50% of potential maximum data availability during this time interval (e.g. with an effective time resolution of 10 min, the MWR can have up to 19 CBLH measurements between 12:00 and 15:00, from which we require at least 9 to compute the median).

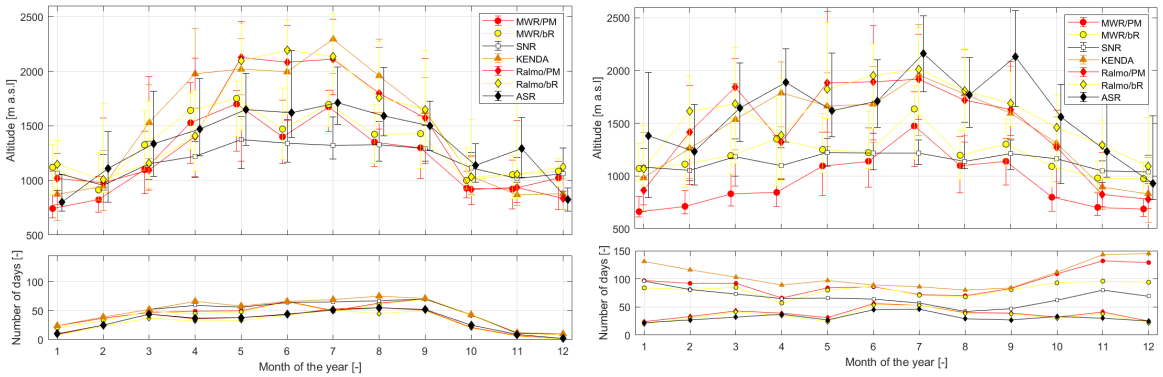

(A) Clear sky (B) Cloudy sky

FIGURE 5.5: Climatology (2016-2020) of the $CBLH^{Max}$ for clear and cloudy sky conditions in Payerne. The "error bars" correspond to the quantiles 25 and 75%. Lower panel: number of monthly cases.

Clear-CBL: A net seasonality is observed for the $CBLH^{Max}$, with minimum at 700-1100 m a.s.l. during the October-February period and maximum at 1400-2300 m a.s.l. during the May-August period, depending on the instrument/method used. Also note the seasonality in data availability, from around 10 total days in December up to 70 total days for August, due to increased amount of cloudy days in winter. RALMO and KENDA produce similar $CBLH^{Max}$ throughout the year, with a slightly higher values for KENDA in March and April. RALMO/bR reaches a minimum in February at 1000 m a.s.l. and a maximum in June at 2200 m a.s.l., while KENDA/bR is lowest in November-January at 900 m a.s.l. and maximum in July at 2300 m a.s.l. Furthermore, taking RALMO as a reference, MWR/PM and MWR/bR underestimate the $CBLH^{Max}$ during the summer month with a difference of about 500 m where no bias is visible during winter time. This supports the hypothesis that MWR is over-heated during the summer, causing a negative bias in the CBLH retrieval. Another feature of interest is the $CBLH^{Max}$ decrease in June, intensely marked with MWR/PM and bR, less so with KENDA and RALMO/PM and not visible with RALMO/bR. This finding is also observed for the other stations (Appendix B, Fig. B.4) and found all over Switzerland using KENDA model and CABAM detection algorithm on ceilometers (D. Ifergan, personal communication).

In case of unstable conditions, the RL measured by RALMO/ASR is replaced during the day by the CBLH, hence explaining the clear seasonal cycle observed. Indeed, as the convective layer grows after sunrise, the aerosols also rise convectively and a sharp decrease in concentration is observed at the boundary between the CBL and the free troposphere. Here, this layer height is underestimated by about 500 m during the summer compared

to RALMO/PM and bR. One explanation could be that the mixed layer height (measured with RALMO/ASR) is lower than the mixing layer height (measured with RALMO/PM and bR) between 12:00 and 15:00, suggesting that a time lag may exist between the two. WP/SNR also exhibits a clear, yet less pronounced, seasonal cycle due to vertical turbulence, caused by convection, being stronger in summer than in winter. The maximum of turbulence measured is however lower than the $CBLH^{Max}$ computed with the other methods/instruments in summer ($\sim$ 250 m under RALMO/ASR and 750 m under RALMO/PM and bR) and almost equal during winter time.

The ranges of values on the annual cycle of the clear-$CBLH^{Max}$ presented here correlate with other studies around Europe, for which the results are summarized in Table 5.1. In Palaiseau, Pal and Haeffelin, 2015, found mean seasonal $CBLH^{Max}$ around 1900 and 1000 m a.g.l. for summer and winter respectively, using aerosol lidar observations. These values are slightly greater to the one we found in Payerne using RALMO/ASR. First, Palaiseau station is located at lower altitude than Payerne, with a higher mean T throughout the year; then, the station is located in a very flat area with no effects of the neighbouring topography as it the case in Payerne. Baars et al., 2008, found slightly lower values in Leipzig than in Palaiseau, also using aerosol lidar observations. In Leipzig, the urban environment greatly influences the PBLH dynamics, by providing higher air T and turbulences due to asphalt and buildings. Moreira et al., 2020, found high mean seasonal $CBLH^{Max}$ in Granada, using MWR/PM (2000 and 1000 m a.g.l. for summer and winter respectively). Although Granada station is at higher altitude and, to some extent, in a mountainous terrain, the lower latitude and hence higher seasonal T favor a deeper CBLH formation. Finally, Seidel et al., 2012, found $CBLH^{Max}$ of respectively 1800 and 1000 m a.g.l. for summer and winter over Europe, using IGRA radiosonde data archive with bR. This is in the same order of values than what we computed for Payerne, also using RS/bR.

Overall, the differences observed here arise from different mean seasonal air T, humidity, amount of sunny days and topography, from site to site. The instruments and methods used also differ to some extent, resulting in a coherent, yet site-dependant, CBLH detection over Europe with limited interpolation possibilities.

	lidar/PM	lidar/bR	lidar/ASR	MWR/PM	MWR/bR	RS/PM	RS/bR	KENDA
Payerne (490 m a.s.l.)	1430/710	1480/790	1270/760	870/320	950/630	1600/620	1610/640	1450/700
Grenchen (428 m a.s.l.)	-	-	-	1160/420	1230/690	-	-	1500/620
Schaffhausen (438 m a.s.l.)	-	-	-	1110/470	1200/680	-	-	1600/670
Granada (680 m a.s.l.) (Moreira et al., 2020)	-	-	-	2000/1000	-	-	-	-
Palaiseau (160 m a.s.l.) (Pal and Haeffelin, 2015)	-	-	1900/1000	-	-	-	-	-
Leipzig (113 m a.s.l.) (Baars et al., 2008)	-	-	1800/800	-	-	-	-	-
Europe (Seidel et al., 2012)	-	-	-	-	-	-	1800/1100	-

TABLE 5.1: Summer/winter $CBLH^{Max}$ [m a.g.l.] in the three stations of interests and in other studies in Europe, using multiple instruments and methods. The mean seasonal (summer and winter) $CBLH^{Max}$ comprise all weather conditions (clear and cloudy included).

Cloudy-CBL: For cloudy conditions, the seasonality is less pronounced, with minimum between 600 and 1400 m a.s.l. in winter to 1500-2100 m a.s.l. in summer. One should also notice the greater data availability for this category, up to three times the amount of data available in clear sky conditions for some instruments. MWR/PM and, to a lesser extent, MWR/bR, present lower cloudy-$CBLH^{Max}$ throughout the whole year, taking KENDA and RALMO as reference. The hypothesis of instrument's heating holds as the difference is larger in summer. However, the number of cases for each month is up to four times lower

with RALMO than MWR (see lower panel of Fig. 5.5b), occurring during days without precipitation or low cloud cover. These conditions favor higher cloudy-CBLH and a positive bias of RALMO. If we restrict MWR to the same cases as RALMO (Appendix B, Fig. B.5), the difference between the two instruments is then reduced by about 200 m throughout the year.

RALMO/ASR also exhibits a seasonality with values about 500 m higher than in clear sky conditions, falling in the same range of values than KENDA/bR or RALMO/bR. This behaviour, that was not observed for clear sky conditions, could be explained with one of the following hypothesis:

1. Cloudy conditions reduce the time-lag between mixing and mixed layer height, making them coincide when the CBLH maximum is reached.

2. The signal is affected by passing clouds and the PBLH is set to the cloud height. Indeed, even if the cloud flagging system should not allow PBLH to be computed when clouds are detected by the ceilometer CL31 (after 2018), RALMO and CL31 don't have the same temporal resolution, so that there may be clouds during RALMO acquisition time (30 min) but not at the time at which the profile is attributed. Hence, a possible improvement would be to extend the cloud flagging system to the 30 min during which RALMO retrieves one single profile.

Regarding WP/SNR, no seasonality is observed, with a constant annual height at around 1200 m a.s.l. The same flagging system than for RALMO/ASR is used, so that clouds should have, in theory, no influence on the computed PBLH with WP/SNR. This flagging system was however only available after 2018 since no CL31 was installed before that. Such a constancy could be explained by the fact that humidity structures, influencing the turbulent ones, are found at constant heights throughout the year. Interestingly, 1200 m a.s.l. is about the height of the neighbouring Jura mountains. More researches are needed here to elaborate hypotheses and validate them.

It can also be seen that the difference between the PM and bR is larger in cloudy conditions (up to 500 m between MWR/PM and bR in April, or 500 m between RALMO/PM and bR in November) than in clear sky conditions (no more than 200 m throughout the year). As these two methods mostly differ in the consideration of radial wind speed by the bR, it is safe to assume that the observed differences can be attributed to this variable. Indeed, the difference is larger in winter, where the bR is found at much higher altitude than PM, meaning that strong radial winds decrease the value of the Ri_b and the PBLH is consequently set at higher altitude.

Finally, the IQR is on average larger for cloudy conditions than clear sky ones, with annual median IQRs for RALMO/ASR, RALMO/PM and KENDA/bR of respectively 793, 820 and 671 m for cloudy conditions and 585, 758 and 531 m for clear sky conditions. This is coherent with what was found and discussed in Figures 5.3 and 5.4 for the comparison of instruments and methods. The annual median IQR is however the same for the MWR in clear or cloudy conditions. Furthermore, the median IQR for summer is not different from the one for winter for all instruments/methods, suggesting that the PBLH monthly data dispersion is not influenced by the season.

5.4.2 00:00-03:00 climatology

The same procedure of monthly median is applied for all data between 00:00 and 03:00 to obtain the nocturnal PBLH climatology for clear and cloudy sky conditions in Payerne (see Figure 5.6). Overall, KENDA/bR is at the lowest altitude throughout the year, then we find the SBI measured with MWR and RALMO, followed by bR and WP/SNR. The SBLpt measured with MWR and RALMO is found at higher altitude and finally RALMO/ASR (RL)

corresponds to the highest layer. This is coherent with the theory exposed in Chapter 1, in terms of layers height and differences. The layers are discussed in more details hereafter.

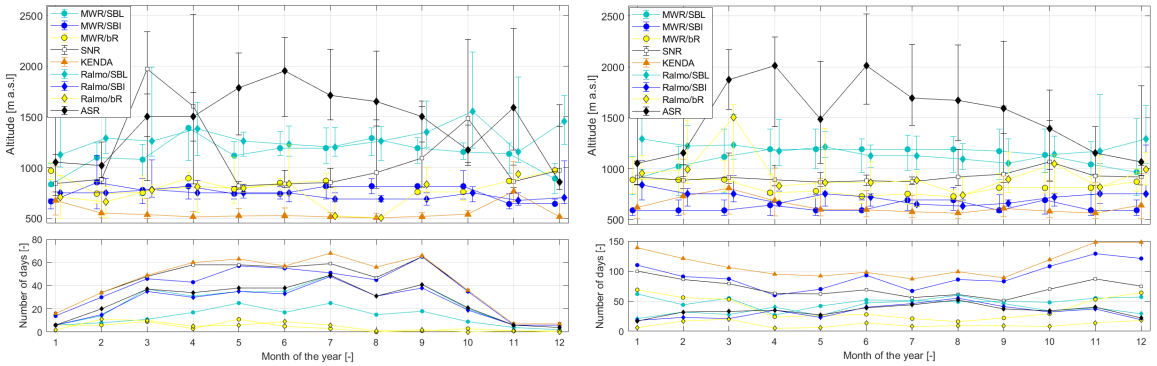

(A) Clear sky (B) Cloudy sky

FIGURE 5.6: Climatology (2016-2020) of the nocturnal PBLH taking the monthly median of the median between 00:00 and 03:00, for clear and cloudy sky conditions in Payerne. The "error bars" correspond to the quantiles 25 and 75%. Lower panel: number of monthly cases.

RL: A well-defined seasonality is observed for RALMO/ASR in both clear and cloudy sky conditions. During the night, the RL height is dependant on the maximum CBLH attained on the previous days. Looking at Fig. 5.5, it can be observed that the climatology of RALMO/PM, RALMO/bR and KENDA, taking the median between 12:00 and 15:00 ($CBLH^{Max}$), is very similar to the one of RALMO/ASR, taking the median between 00:00 and 03:00 (RL), with a maximum attained in June at about 2000 m a.s.l., and globally about 200 m lower than the former. Furthermore, this difference is smaller that the one obtained taking RALMO/ASR between 12:00 and 15:00 ($CBLH^{Max}$), up to 500 m in summer. As discussed before, a time lag could explain this difference between mixing and mixed layer height as the layer height measured with RALMO/ASR keeps on increasing after 15:00.

WP/SNR: The RL height is not retrieved as it was the case with the algorithm used by Collaud Coen et al., 2014. Indeed, the continuity criterion applied in the latter makes it so that, when the cloud base height or RL is detected, the layer is followed for the next time steps. Instead, with the algorithm used in this project, a layer at constant height is found ($\sim$ 900 m a.s.l.) with very large increase in March-April and August-October in clear sky conditions. It is not fully understood why we have these sharp increase at these time but the main hypothesis is that massive bird migrations strongly affect the WP signal and the corresponding PBLH. Indeed, bird migrations happen only at night, usually from March to June and from September to November, with flying heights corresponding to the anomalies that we observe (> 1500 m). For the measured radial wind velocities, a flagging system is used to detect data corrupted by bird migrations based on a Gabor-frame-expansion-filtering of the raw signal (Lehmann, 2012). However, this method is not applicable on the SNR directly. For technical reasons, the raw signal could not be retrieved, nor the attributed bird flagging.

SBLpt: The SBLpt, retrieved with RALMO and MWR, has no evident seasonality in clear and cloudy sky conditions. However, we see that the SBLpt is slightly higher in clear sky conditions due to stronger radiative cooling ($\sim$ 1200-1400 m a.s.l. throughout the year) than in cloudy conditions ($\sim$ 1000-1200 m a.s.l.). Some differences are also observed between RALMO and MWR, where the SBLpt is usually higher with RALMO. However, due to a

large difference of instrument's vertical resolution, the comparison of the two may not be relevant. Also note how the data availability of the radiometer for the SBLpt is significantly lower than with RALMO, due to a low vertical resolution that, most often, does not allow to recover altitudes of neutrality in θ profiles.

SBI: A very weak seasonality is observed for the SBI retrieved with RALMO and MWR. In clear conditions, this layer is located around 700 m a.s.l. at its maximum, which is much lower than the SBLpt, as expected. In cloudy conditions, the layer is closer to the ground ($\sim$ 600 m a.s.l.) due to a less intense radiative cooling and a hence higher ground T. A significant difference is observe in the layer's height retrieved by the two instruments in August and September in clear sky conditions. Indeed, at the inter-season, their are more small variations along the T profiles, which leads to a lower SBI detection by RALMO, as its vertical resolution recover short inversions heights. This is not the case for the radiometer that usually only retrieve one inversion in the T profile.

bR: During the night, the bR method is applied on RALMO, MWR and KENDA T profile. The latter predicts a constant layer throughout the year near the ground ($\sim$ 20 m a.g.l. and 100 m a.g.l. for clear and cloudy sky conditions respectively). For most stable cases, the Ri_b number exceeds its threshold at the first altitude range, thus setting the PBLH just above ground. In cloudy conditions, conditions of weak stability rise this layer to some extent. However, the results with RALMO and MWR are quite different, with more variations throughout the year at globally higher altitudes. It is arguably safe to assume that these values are wrong and biased. Indeed, as mentioned already, the data availability of the WP for radial wind speed components is very low near ground. As a result, only cases of very weak stability, where Ri_b can still be inferior to the threshold at the altitude of first WP data available, allow for a PBLH detection. This causes the PBLH data not only to be positively biased, but also very sparse as it can be seen in the lower panel of data availability.

5.4.3 Diurnal cycle climatology

The climatology of the diurnal and monthly cycles is performed by taking the hourly median for each days and months of the year.

bR throughout the day: Conveniently, the bR method allows to retrieve PBLH continuously throughout days and nights. The results for KENDA/bR for clear, cloudy and very cloudy conditions in Payerne are shown in Figure 5.7. The data for RALMO/bR and MWR/bR are however too sparse and unreliable during the night (positive bias discussed in Sect. 5.4.2) to perform the same climatology.

In clear conditions (Fig. 5.7a), both diurnal and seasonal cycles are clearly exposed, with a maximum PBLH at about 2200 m a.s.l. between 13:00 and 14:00 in July, corresponding to the CBLH^{Max}, and a minimum around 550 m a.s.l. during the night throughout the whole year. The CBL starts to grow, with a small delay ($\sim$ 20 min), after sunrise and decay shortly after the maximum is reached between 12:00 and 14:00. Consequently, the CBL extends higher and longer during the summer, when the days are at their longest, than in winter where the CBL hardly reaches 1000 m a.s.l. During the night, however, the data are quite uniform throughout the year. Indeed, as mentioned in the previous section, it is rather unclear what this nocturnal layer of low altitude corresponds to when using bR to compute the PBLH. The lower CBLH^{Max} in June is also visible here, with an altitude of 1800 m a.s.l. compared to the 2200 and 2000 m a.s.l. of July and May respectively.

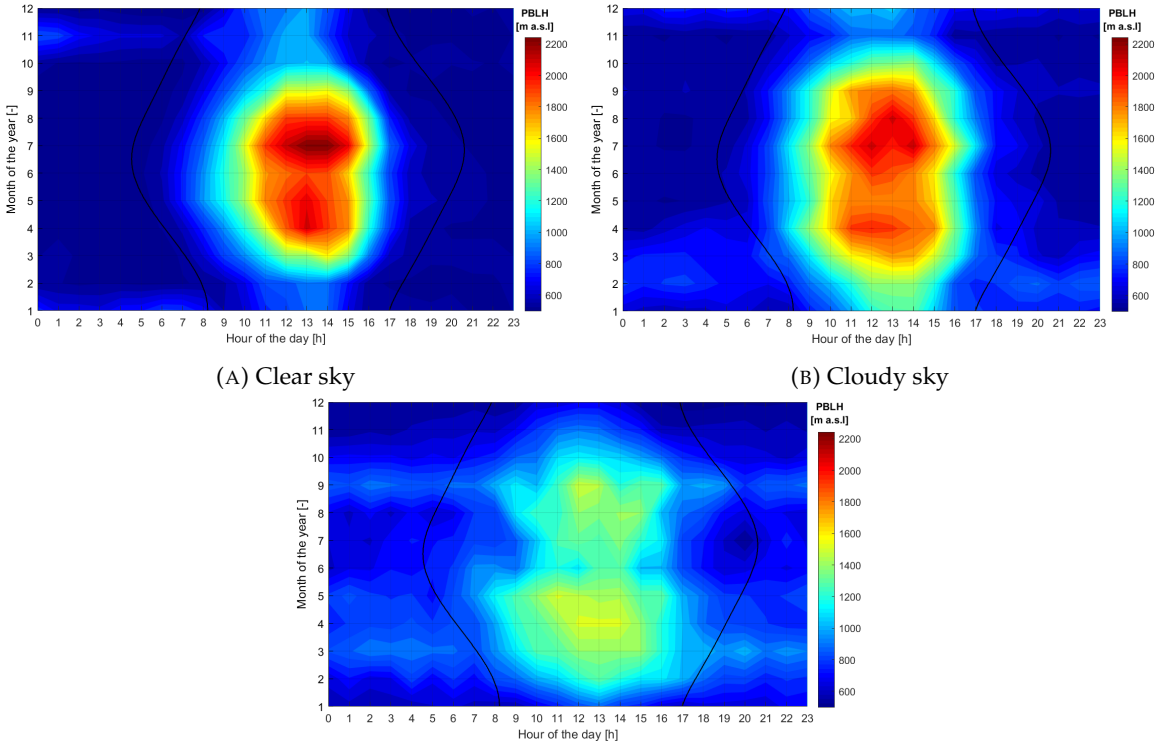

(A) Clear sky

(B) Cloudy sky

(C) Very cloudy sky

FIGURE 5.7: Climatology (2016-2020) using KENDA/bR in Payerne for clear, cloudy and very cloudy sky conditions. PBLH values are interpolated between each node of the grid. The black curved lines indicate sunrise and sunset hours throughout the months. Note that the color scale is the same for all figures.

In cloudy conditions (Fig. 5.7b), the maximum in July decreases by some 200 m, due to the reduced solar heating and hence, convective forces. Nonetheless, the PBLH is higher around noon in October and between January and March compared to clear conditions. The timing of CBL growth, maximum and decay isn't affected by the cloudiness.

Finally, for very cloudy conditions ($\geq$ 7 okta, Fig. 5.7c), the decrease in PBLH maximum during the day is even more pronounced, for all months. The maximum is now reached in April, with a PBLH at about 1500 m a.s.l. between 12:00 and 14:00. The decrease in June is also well observed with ,additionally, shorter growth and decay time of the CBL. Interestingly, during the night, the PBLH is higher at the inter-season in March and in September. This corresponds to a prevalence of situations such as the one described earlier in Figure 5.2, with a low cloud cover and high wind speed, affecting the PBLH detection with bR.

For the stations of Grenchen and Schaffhausen, the results are available in Appendix B, Fig. B.6 and B.7 respectively. Similarly to Payerne, the CBL reaches a maximum altitude in July, between 12:00 and 14:00, at about 2200 m a.s.l. The lower PBLH in June during daytime is also observed for both stations and a higher nighttime PBLH is found for very cloudy sky conditions in March and, to a lesser extent, in September. This suggest that due to their resemblance in topography and nearby land-use, the PBL over these 3 stations behave similarly.

SBI during nighttime and PM during daytime: As PM only works for unstable atmospheric conditions (i.e. during the day mostly), another method is needed to cover nighttime in the climatology's diurnal cycle. It is convenient to use the SBI due to its great data

availability (see Fig. 5.6 lower panel). SBLpt is however too sparse and dependent on vertical resolution of the instrument, so that the climatology would be irrelevant. Figures 5.8a and 5.8b show the climatology using SBI and PM in Payerne, for RALMO and MWR respectively, in clear sky conditions.

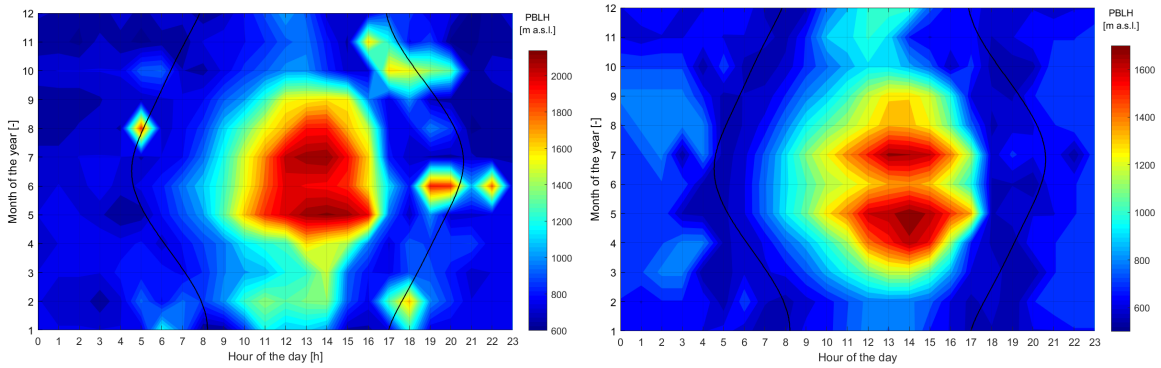

(A) RALMO SBI + PM (B) MWR SBI + PM

FIGURE 5.8: Climatology (2016-2020) using SBI during the night and PM during the day, with RALMO (left) and MWR (right), in Payerne for clear sky conditions. PBLH values are interpolated between each node of the grid. The black curved lines indicate sunrise and sunset hours throughout the months. Note that the color scale is not the same in each figure.

For RALMO, the climatology presents a maximum CBLH in July and May, between 12:00 and 14:00, at about 2100 m a.s.l., corresponding with what was found earlier for KENDA/bR in clear sky conditions. The CBLH is also higher in winter and spring (1200-1400 m a.s.l.) than in autumn (800-1000 m a.s.l.). The $CBLH^{Max}$ decrease in June (1900 m a.s.l.) is also found. Outliers are observed at sunrise and sunset, with PBLH superior to 1400 m a.s.l. Indeed, the climatology algorithm first takes the available SBI heights and then replace them with PM if a value is available at the same time. These values correspond to rare situations of strong morning and evening instabilities and can hence be discarded in the analysis of this 5-year climatology. During the night, the SBI is located between 800 and 1000 m a.s.l. As expected, this is higher than what is found using KENDA/bR. In cloudy conditions (Appendix B, Fig. B.8a), the climatology is very similar, with however higher CBLH in March (1600 m a.s.l. between 12:00 and 14:00) and in October (1500 m a.s.l. at 13:00), due to stronger instabilities at the inter-season.

The same climatology using MWR/PM yields different results. As it was already observed in other representations, the CBLH is globally lower than with KENDA/bR and RALMO, with a maximum at 14:00 in May at about 1800 m a.s.l. The decrease in June is also more intense, with a $CBLH^{Max}$ at 1400 m a.s.l., suggesting that an additional effect of instrument's heating enhances this observed phenomenon. During the night, similarly to RALMO, the SBI is located at about 800 m a.s.l. This is also higher than what is found with the PM in early morning and late afternoon ($\sim$ 600 m a.s.l.). In cloudy conditions (Appendix B, Fig. B.8b), the decrease in June disappears and the CBL rises lower, with a maximum in June at 1400 m a.s.l. between 11:00 and 14:00.

RL with RALMO/ASR We discussed earlier how the RL height is related to the CBLH and its seasonality throughout the year. It is hence convenient to analyse the diurnal climatology of RALMO/ASR and compare it with RALMO/PM. Figure 5.9 shows this representation for both clear and cloudy sky conditions.

We observe a well defined seasonality and diurnal cycle for the PBLH retrieved with RALMO/ASR in both clear and cloudy sky conditions: the layer is at maximum height

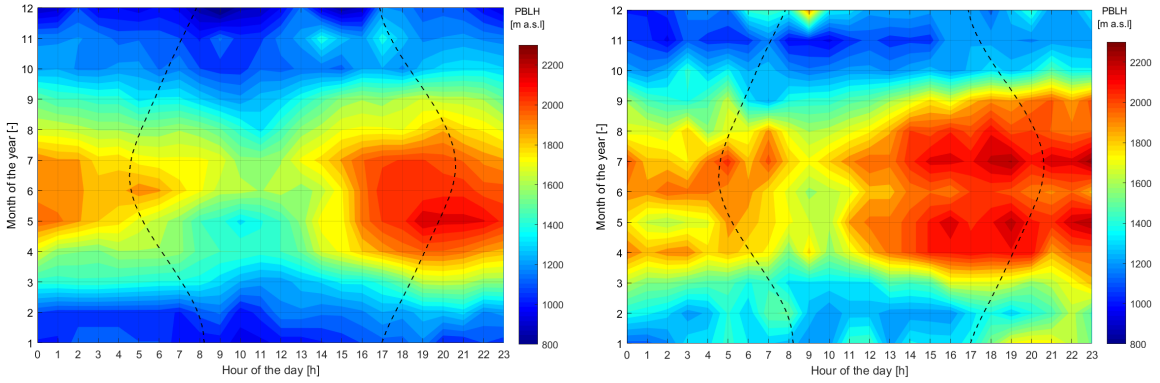

(A) Clear sky

(B) Cloudy sky

FIGURE 5.9: Climatology (2010-2020) using RALMO/ASR in Payerne for clear and cloudy sky conditions. PBLH values are interpolated between each node of the grid. The dashed black curved lines indicate sunrise and sunset hours throughout the months.

between 16:00 and 00:00 ($\sim$ 2100 m a.s.l.) and lowest between 08:00 and 15:00 ($\sim$ 1600 m a.s.l.). From October to February, the diurnal variability disappears and the layer is kept at almost constant height ($\sim$ 1000 m a.s.l.). This could be explained by the fact that, due to a strong decrease in convective forces at this period, the mixing layer height is defined, no more by convective forces, but by turbulent ones. The constant height observed here also correspond with the WP/SNR yearly constant height in cloudy conditions (clear sky conditions to a lesser extent), as seen in Figure 5.6, supporting the above hypothesis. In spring and summer, a maximum is found in late afternoon and is kept almost constant until midnight. In clear sky conditions, this maximum is attained at 19:00 in May, at about 2100 m a.s.l. This corresponds to the CBLH^{Max} found with RALMO/PM earlier. However, a time lag of almost 3 hours is observed between these 2 maximum, suggesting that it takes more time for the aerosols to mix in the CBL (mixed layer) than what is theoretically predicted with the PM (mixing layer). Kotthaus et al., 2020, also found a maximum around 18:00-19:00 using STRATfinder and CABAM algorithms on lidars ceilometers measurements. Surprisingly, this time lag is reduced to zero in cloudy conditions. This finding strengthen the hypothesis that cloudy conditions favor a more coherent detection of the PBL with different instruments and method, by providing conditions of weaker instabilities and a more stratified atmosphere through less intense convective forces. Finally, the decrease of the RL after sunrise can be explained by movements of subsidence associated with convective cells, while in winter, the lack on convection (also seen with the PM) results in a constant RL height.

5.4.4 June CBLH decrease

Every climatology presented earlier show a lower PBLH during daytime in June, with all instruments/methods and in all three stations of interest. This singular behaviour has, to the day, found no clear explanation. We here present the tested hypotheses and propose new ones to uncover the physical origins of these observations. Among all the variables influencing the CBLH, air temperature is one of the most important ones. However, historic measurements across Switzerland (Appendix B, Figure B.9) show no negative anomalies in the June monthly T measurements. Quite oppositely, between 2016 and 2020, June has been on average very warm, dry and sunny, with June 2017 and 2019 being respectively the second and third hottest June months since 1961 at the northern-Switzerland scale. A climatology of KENDA/bR for clear sky conditions where each year is treated separately

is given in Appendix B, Fig. B.10. There, we observe that the PBLH decrease is especially marked in 2019. However, as stated before, June 2019 was very hot, which should theoretically correspond to a higher PBLH. While July 2019 was also a hot month, it is not the case for the month of May that saw its monthly temperature drop by 2.5 °C compared to the 1981-2010 reference, in addition to being wet (+ 5 % precipitation). Zhang et al., 2013, established, with a RS/bR data set over Europe (>25 y), that PBLH was negatively correlated to surface relative humidity. By saturating the soil in water, the strong precipitations in May could have then limited the growth and extent of the CBL in June. There are nonetheless no proofs to support the hypothesis that the weather of the previous month could influence the PBLH of the next one. Pressure is also a variable that strongly influences the PBLH. An analysis of the synoptic weather conditions over Switzerland for the period of the study (2016-2020), using the GWT26 classification from the COST 733 data set (Huth et al., 2015), revealed no particular behaviour in June compared to the other months (see Fig. B.11 in Appendix B). Interestingly, it is in May that a strong decrease of anticyclonic conditions and increase of cyclonic ones is observed, theoretically enhancing convection. Collaud Coen et al., 2011 performed a similar climatology between 1995 and 2008, using SYNALP weather classification, and found a net increase of anticyclonic conditions in June, contrasting with our findings. As anticyclonic conditions favor subsidence, an increase of this weather type in June should correlate with our observations of decreased PBLH during this month. The discrepancies in the climatologies performed with different weather classifications may be explained by the different threshold used in the attribution algorithms (Philipp et al., 2014), which makes it difficult to compare synoptic weather types obtained with different classification methods. The different investigations have not been conclusive in finding the origins of the lower observed PBLH in June, making it a thrilling research topic for further studies.

5.5 Growth rate

The CBL growth rate has been computed for different instruments and methods, taking the slope of the linear regression between the first value after sunset and the $CBLH^{Max}$. The results for Payerne are shown in Table 5.2 and those for Grenchen and Schaffhausen can be found in Appendix B, Tab. B.1 and B.2 respectively. The distributions of seasonal growth rate, computed with KENDA/bR in Payerne, are given in Figure 5.10. Overall, KENDA and RALMO fall in the same range of values for all season, with maximum in summer at 246, 226.3 and 231.1 m/h for KENDA/bR, RALMO/PM and RALMO/bR respectively. Note that summer is also the season with most available cases to compute the growth rate. Oppositely, autumn has the smallest CBL growth rate with 104.3, 93.6 and 87.1 m/h for, respectively, KENDA/bR, RALMO/PM, RALMO/bR and the less amount of available cases. This seasonality in growth rate is caused by the variation in solar heating and air temperature, that causes the CBL to convectively grow faster and higher in summer than in winter or autumn. In spring, the CBL growth rate is also high due to strong atmospheric instabilities at this time of the year. The winter and autumn distributions for KENDA/bR (Fig. 5.10) show an asymmetric shape (S_k^{winter} = 0.6, K_t^{winter} = 2.5, S_k^{autumn} = 1.6 and K_t^{autumn} = 6.1), meaning that CBL growth rate is most often limited in theses seasons but there exists some cases of rapid growth for sunny days with instabilities. In spring and summer, CBL growth rates are more Gaussian-like distributed around the median (S_k^{spring} = 0.8, K_t^{spring} = 3.9, S_k^{summer} = 0.1 and K_t^{summer} = 2.6).

The growth rate measured by MWR/PM and MWR/bR is much smaller, with weak seasonality, than for the other methods cited before. In autumn and winter, the difference with KENDA and RALMO is less marked than in spring and summer, with a difference

	Winter	Spring	Summer	Autumn
KENDA/bR (N)	116.6 (110)	223.9 (182)	246.0 (215)	104.3 (64)
RALMO/PM (N)	128.3 (67)	193.1 (99)	226.3 (147)	93.6 (30)
RALMO/bR (N)	108.2 (67)	173.4 (98)	231.1 (143)	87.1 (28)
MWR/PM (N)	104.0 (105)	133.5 (155)	133.2 (180)	103.6 (61)
MWR/bR (N)	95.7 (100)	124.4 (149)	139.3 (178)	101.7 (61)
SNR (N)	87.7 (106)	88.4 (167)	85.6 (198)	85.3 (57)

TABLE 5.2: Seasonal CBL median growth rate [m/h] in Payerne (2016-2020) with different instruments and methods. The numbers in parenthesis (N) correspond to the number of days available for computation.

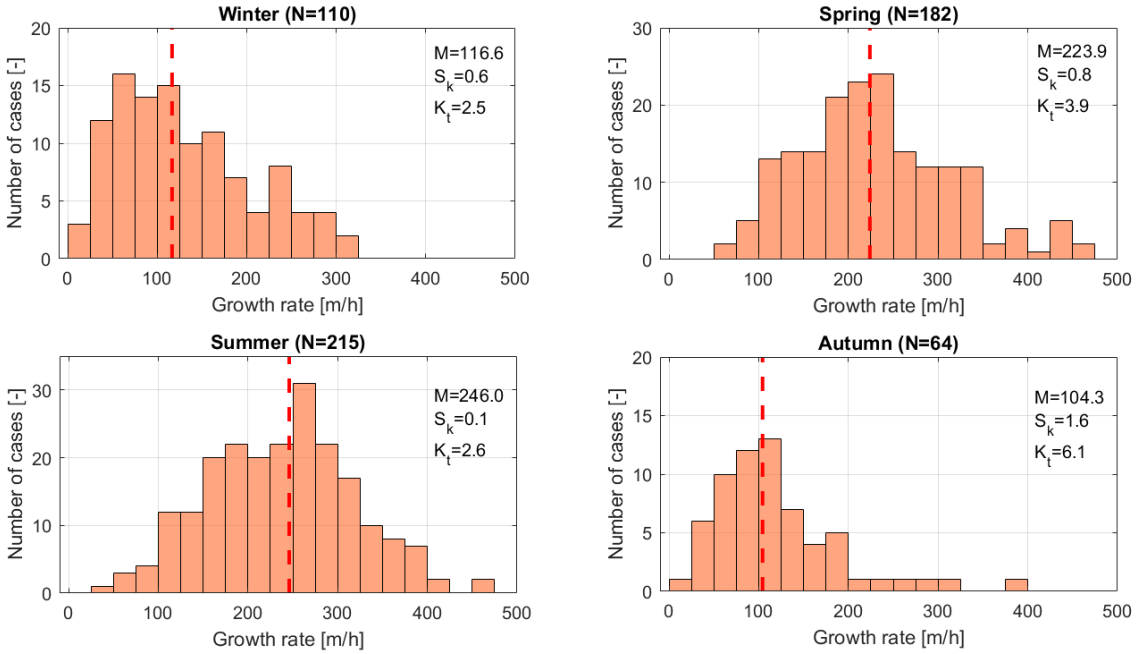

FIGURE 5.10: Seasonal CBL growth rate histograms, computed with KENDA/bR (2016-2020) in Payerne. The red dashed lines correspond to the medians (M) of the distribution. For each histogram, the skewness (S_k) and kurtosis (K_t) coefficient are computed.

between MWR/PM and RALMO/PM of 93.1 and 24.3 m/h in summer and winter respectively. This can be attributed to the instrument's heating in spring and summer, that lowers the CBLH and consequently, the growth rate.

The growth rate computed using WP/SNR show no seasonality, at about 85 m/h all year long. In summer however, the skewness coefficient of the data distribution is of 10.1, against 3 in winter, suggesting that their are more cases of high growth rate in summer. As we saw earlier in Sect. 5.4.1, the CBLH^{Max} is found at lower altitude when using WP/SNR, with little to no seasonality. This is coherent with what we observe here, where the measured maximum of wind turbulence yields a constant growth rate throughout the year. This instrument/method is hence to be discarded for CBL growth rate computation.

The seasonal growth rates found with KENDA and RALMO in Payerne coincide with what was found in summer in Palaiseau, using lidar observations and the same growth rate computation method (Pal and Haeffelin, 2015). They reported growth rates of 220, 250, 200 and 150 m/h for spring, summer, autumn and winter respectively. The lower

altitude of Palaiseau station (i.e. 160 m a.s.l.) and its milder winter condition could explain why they observed faster growth rate in autumn and winter. Furthermore, Moreira et al., 2020, reported growth rates of 300, 400, 230 and 220 m/h for spring to winter, using MWR measurements and PM in Granada. There, the climatological conditions, being hotter and drier, make for a fast CBL growth, that also extends higher.

In Grenchen and Schaffhausen, the results are similar for KENDA, but the growth rate computed with MWR/PM and bR is significantly higher than in Payerne (203.6 and 165.1 m/h in summer with MWR/PM). This corresponds with a higher measured $CBLH^{Max}$ in these two stations, using MWR/PM or bR (see Table 5.1).

5.6 Long-term trends

The long-term CBLH trends were computed using RS measurements at 12:00 UTC with PM and bR. The initial time series covered 50 years worth of data, from 1970 to 2020 for both PM and bR (see Fig. 5.11 and 5.12 respectively). Due to inhomogeneities in the time series, a shorter data set of 30 years, from 1991 to 2020 was chosen. Indeed, missing pressure measurements for 1981-1982 at Payerne SMN station resulted in a hole in the data set. Additionally, the radiosonde replacement in April 1990 (from mechanical to electronic radiosondes, see Sect. 2.2.2) changed drastically the vertical resolution of the instrument. This can be observed in the RS/PM timeseries, for which a rupture in the mean (decrease) occurs at the mentioned date of radiosonde replacement. For RS/bR, this rupture is not visible but an other one is observed at the end of 2006, where the minimum yearly values are decreased to some extent. It remains unclear why this rupture happens as no important instrument modifications were recorded at that date.

While a trend computation on the SBI or SBLpt would have been interesting, this was not possible due to strong inhomogeneities in the time series, even between 1991 and 2020. Indeed, as the radiosondes model changed in 2011 (see Sect. 2.2.2), the vertical resolution was further improved, from about 15-20 m to 5 m. For SBI and SBLpt, this change in vertical resolution is observed in the time series with large decrease in the mean and variance (see Appendix B, Figures B.12 and B.13).

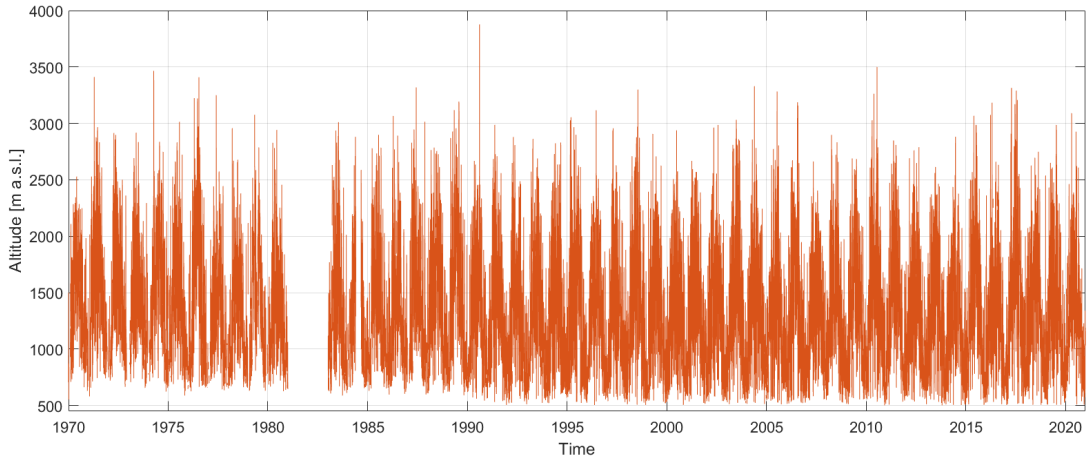

FIGURE 5.11: RS/PM timeseries between 1970 and 2020.

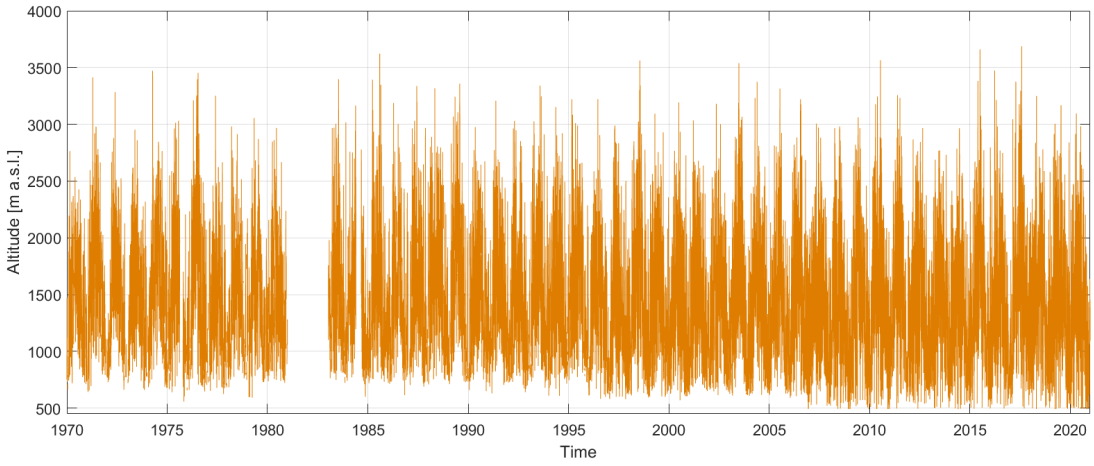

FIGURE 5.12: RS/bR timeseries between 1970 and 2020.

Trends computed with Mann-Kendall test: The results of the seasonal Mann-Kendall test associated with the Sen's slope, using RS/PM, are presented in Figure 5.13 and in Appendix B, Figure B.14 for RS/bR. As stated in Sect. 3.6, the yearly trend can only be computed if the seasonal ones are homogeneous, which was here not the case due to a mix of positive and negative seasonal trends. For RS/PM, out of the 231 combinations of starting year and window size, only 26 seasonal trends are homogeneous, allowing yearly trend computation, but only 2 of them are statistically significant (SS). The yearly trends have still been computed with the median of the seasonal ones (see Figure 5.14) to allow a comparison with the other trend computation method.

For RS/PM, three main features are observable and similar for all seasons:

1. Vertical lines (such as the one observed with starting year in 1996/97 and 1999/2000 in summer or in 1995-1998 in winter) should correspond to a strong influence of the starting years, that is, with lower CBLH if the trends are positive. On the other end, diagonal lines (for instance in spring, with trends ending in 2020) correspond to a strong influence of the ending years, with higher CBLH at the end if the trends are positive.

2. There is an alternation of positive and negative trends, depending on the starting year of computation, due to climate decadal variability . In summer for instance, the trends with starting year between 1991 and 1996 are negative, positive between 1996 and 2002, negative between 2002 and 2007 and finally positive again between 2007 and 2011. These oscillation periods are observed, with some minor differences, for all seasons. These variabilities need further researches to be fully understood and characterised.

3. The magnitudes of the trends, positive or negative, decrease with increasing window size. This suggests that, overall, taking a longer period of analysis tend to make the decadal variability discussed above disappear and illustrates how extreme values strongly influence the trend computation for short time series. It is hence commonly admitted that time series of 20-30 years are necessary for reliable long-term trend results, while 10 years are insufficient.

We observe that, for RS/PM, no trend is SS in spring and summer and only a few are significant in autumn and winter (black dots). In autumn, trends ending in 2017-2020 are SS positive for window sizes of 25-30 years and 18-19 years (part of a diagonal line

mentioned before), while in winter, trends starting in 1994-1998 are SS positive for 10-21 years windows (part of a vertical line). Taking the maximum window size (i.e. 30 years), the trends are slightly negative for all season, with about -1 m/y in spring and winter and -0.5 m/y in summer and autumn. These values are however not SS. The maximum trend is found in summer, with starting year in 1997 and a window size of 10 years (1997-2006), at a positive rate of 15 m/y (SS). Oppositely, a negative trend of -7 m/y (not SS) is found taking a data set between 1993 and 2002 or between 2003 and 2012, also in summer.

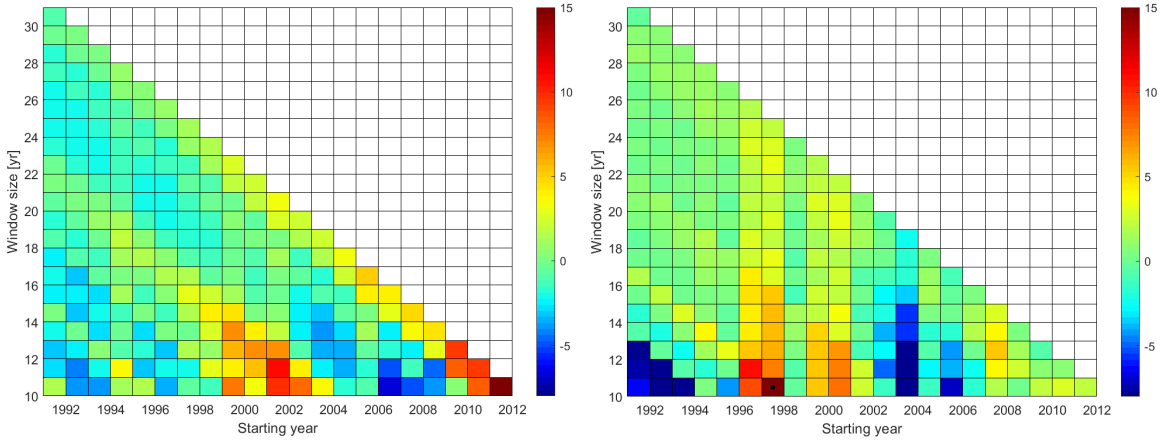

(A) Spring

(B) Summer

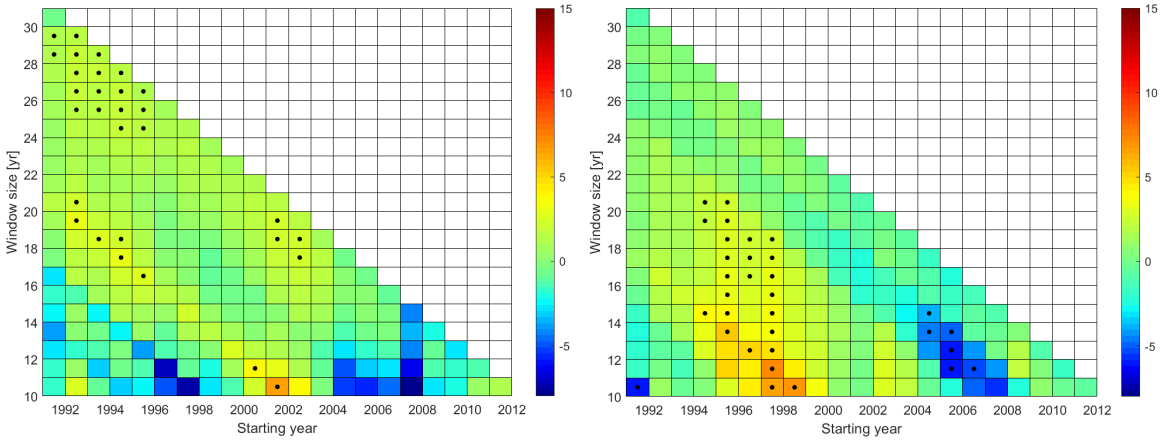

(C) Autumn

(D) Winter

FIGURE 5.13: Seasonal Mann-Kendall trend detection on RS/PM with a 1991-2020 data set. The color scale corresponds to the associated Sen's slope [m/year] for each set of starting year (x-axis) and window size (y-axis). Black dots indicate that the trend is significant on a 90% confidence interval.

The results for RS/bR follow the same pattern with on average, more negative trends. In spring, SS negative trends are found for starting years in 1991/92 and 23-29 years windows. Summer trends with RS/bR are almost identical to RS/PM and autumn ones are similar at the exception that trends ending in 2017-2020 are not SS and are on average more negative. Finally, in winter, SS negative trends are found for starting years before 1995 (i.e. 1991-1995) and 13-30 years windows, as well as for ending years in 2006-2008 and periods of 13, 15-19 and 23-27 years. This is quite different from what was observed with RS/PM, for which the trends were mostly positive.

Finally, the yearly trends for RS/PM and bR follow the same three patterns exposed above, with trends of lesser magnitude, mostly positive for PM and negative for bR. These

values should be regarded as informative only, as the condition of homogeneous seasonal trends was not respected to compute the yearly ones. Nonetheless, homogeneous and SS positive trends are found for starting year in 1999 and window size of 13-14 years, for RS/PM. Oppositely, for RS/bR, homogeneous and SS negative trends are found for starting year in 1991 and window size of 13-14 years too.

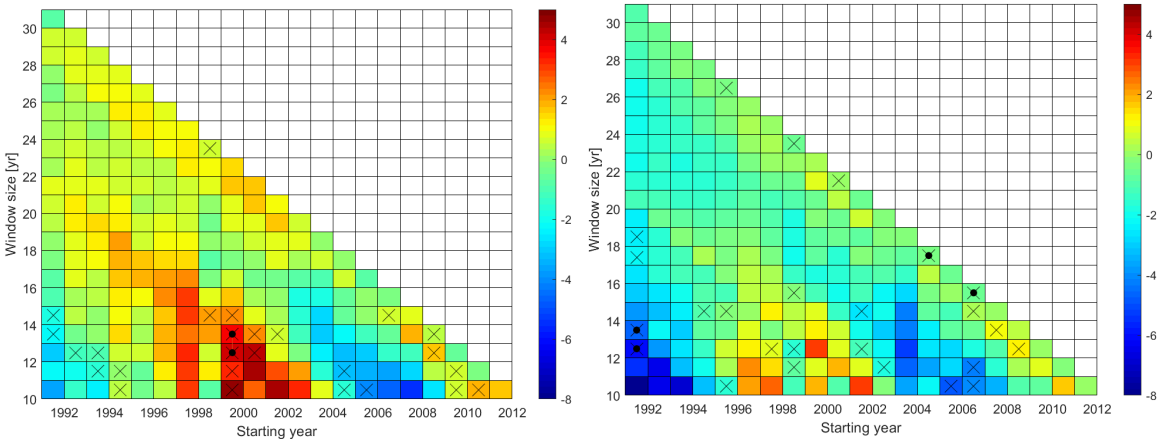

(A) RS/PM (B) RS/bR

FIGURE 5.14: Mann-Kendall trend detection on RS/PM (A) and RS/bR (B) with a 1991-2020 data set. The color scale corresponds to the associated Sen's slope [m/year] for each set of starting year and window size, as the median of the seasonal trends. Crosses indicate that the seasonal trends are homogeneous and black dots indicate that the trend is significant on a 90% confidence interval.

Trends computed with Least Mean Square fit: The LMS method yielded yearly trends for both RS/PM and RS/bR (see Figure 5.16). However, unlike the sMK method, LMS does not provide the seasonal trends. The LMS fit and associated slopes for the various periods are shown in Figure 5.15 a). Figure 5.15 b) shows that the residues are normally distributed, so that the requirements of the LMS method are met. More SS values are found using PM than bR method. A small positive trend is found using the maximum window size (i.e. 30 years), with about 1 m/y using PM (not SS) and a negative trend of -0.5 m/y for bR (not SS). For RS/PM this value is slightly superior to what was found with the sMK-test and equivalent for RS/bR.

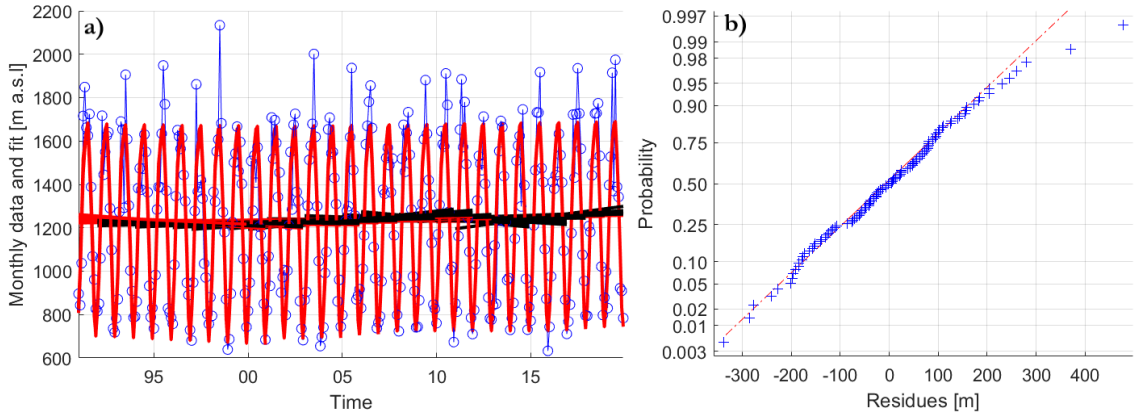

FIGURE 5.15: (a): LMS fit on monthly RS/PM data and trends. (b): Normal probability plot of the residues.

As it was the case with the sMK-test, there is an alternation of positive and negative trends depending on the starting year, for both PM and bR. These oscillation periods are the same one that were found with the sMK-test. A similar tendency of the trends' magnitudes to decrease with increasing window size is also observed. As a matter of fact, the yearly trends for both PM and bR are almost identical to the (inhomogeneous) ones found with the Mann-Kendall test, with nonetheless trends of higher magnitude. For RS/PM, the SS positive trends for ending years between 2007 and 2011 and window sizes between 10 and 19 years correspond with what was observed earlier with the sMK-test for starting years between 1998 and 2002 in spring, summer and mostly in winter, for which the results were SS. For RS/bR, the SS negative trends associated with data sets starting before 1995 correspond with the ones observed in winter with the sMK-test. This hence suggests that between 1991 and 1994, the CBLH was higher than for the next years, resulting in negative trends for the period including these years. Similarly, for PM, periods that include 2017 to 2020 show SS positive trends, so that these years had higher CBLH than the previous ones. Overall, it seems that for both PM and bR, the winter month has the largest impact on the yearly trend computation, especially for small periods affected by extreme values.

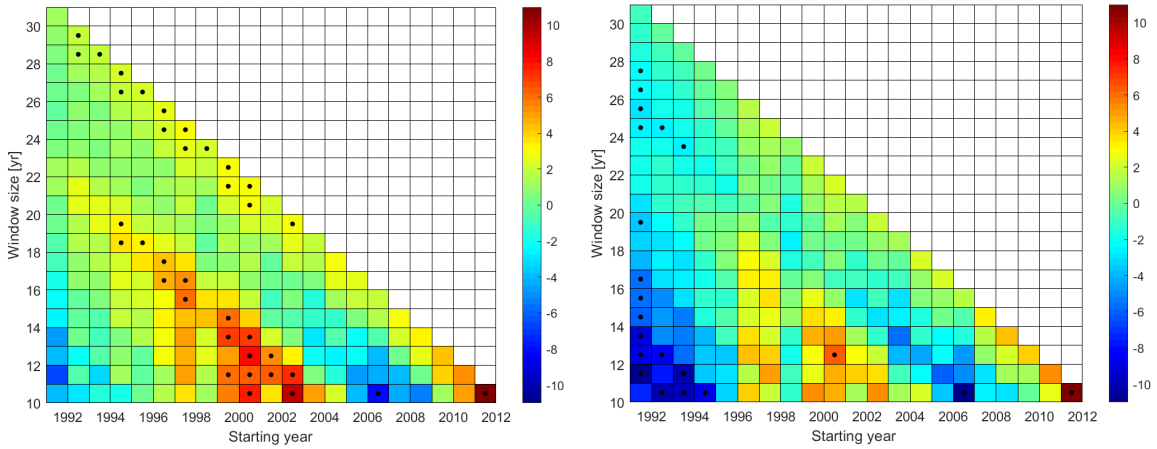

(A) RS/PM (B) RS/bR

FIGURE 5.16: Slope (trend [m/y]) on the Least Mean Square (LMS) fit applied on the monthly median of RS/PM (A) and RS/bR (B) with a 1991-2020 data set. Black dots indicate that the trend is significant on a 90% confidence interval, for each set of ending year (x-axis) and window size (y-axis).

Overall, on the long-term, taking the median of all yearly trends with window sizes larger or equal to 20 years yielded for the sMK-test (LMS) 0.7 (1.3) and -0.9 (-0.95) m/y for RS/PM and RS/bR respectively. The weak positive trend for RS/PM results in a PBLH increase of about 30 m over 30 years and -30 m taking RS/bR. The non statistical significance of most of these results and the small magnitude of trends suggest that no long-term trends are observed for the period 1991-2020. Following the discussion on the errors (see Chap. 4), these could also well correspond to the internal variability of the PBLH and to the uncertainties associated with the depth of the entrainment zone. However, on smaller time scales (< 20 years) more significant trends are observed due to stronger decadal climate oscillations. Maximum SS positive trends of about 10 m/y will results in PBLH increase between 100 and 200 m over 10 and 20 years respectively, oppositely for minimum SS trends of -10 m/y.

Zhang et al., 2013, found an average positive trend of 7.6 m/y over Europe, using RS/bR at 12:00 UTC with data sets of 25 to 37 years, from 1973 to 2010, depending on

the stations. If we shorten our data set to 2010, these results are still far larger than the ones we found with the sMK-test and LMS. In their study, trends were computed using the nonparametric median of pairwise slopes method. However, yearly mean were used, leading to only 25 to 37 values to compute the trends. It was shown by Collaud Coen et al., 2020b, that a low number of data usually lead to an overestimation of the slope and of the statistical significance if the autocorrelation is not taken into account. Li et al., 2020, found, using RS/PM at 12:00 UTC between 1973 and 2013, positive trends in the order of 10 m/y over Europe, Central US or East and South Asia. Mann-Kendall test associated with the Sen's slope was used in their study and SS positive trends were higher in spring and summer than in autumn and winter, similarly to our findings. The method proposed by Yue et al., 2002, was used for pre-whitening in their study. It was however shown by Collaud Coen et al., 2020b that this pre-whitening method tends to generate a lot of type 1-errors (over-estimation of the statistical significance) and virtually increase the slope of the trend. The two studies cited above made use of the Integrated Global Radiosonde Archive (IGRA) data sets, for which the vertical resolution is very low, so that even with a linear interpolation in the PM and bR method, the computed CBLH is greatly impacted.

To this day, these are (to the author's knowledge) the only long-term trends studies available for Europe. An other recent study by Li et al., 2021, covers PBLH trends over the whole globe. Guo et al., 2019, focused their researches on China and Díaz et al., 2019 analyzed long-term trends of the marine boundary layer across the Earth. The lack of studies and the problems of methodology linked to homogeneity, vertical and temporal resolution makes the comparison and validation of the results difficult.

Chapter 6

Conclusion

In this report, the different physical characteristics and variability of the PBLH have been analyzed using a combination of several remote sensing instruments and methods, with a 5-year data set from 2016 to 2020. A total of 9 pairs of instrument/method were used to characterize PBL dynamics during the day and 10 during the night, with some of them providing continuous diurnal measurements. Following the work of Praz, 2013, and Collaud Coen et al., 2014, some of the algorithms were recovered and modified for the purpose of this project. In particular, the automatic PBLH detection algorithm was adapted to take into account RALMO, for which T and RH profiles were not computed at the time of their researches. A new algorithm has been tested on the WP/SNR, based on the work of Liu et al., 2019, mostly different in the sense that no continuity criterion was applied. A methodology for error computation applied on the PM and bR method has also been proposed and the results from different sets of instruments and methods have been compared and validated against RS measurements. A seasonal climatology applied to CBLH and nocturnal-PBLH have been computed for both clear and cloudy sky conditions. The diurnal and seasonal cycles were further analyzed with a climatology applied on KENDA, MWR and RALMO. The CBL growth rate has been computed and discussed for different instruments and methods. Finally, a long-term trend analysis has been applied on a 30-year RS data set, using both PM and bR methods, where two trend computation methods were tested and compared.

The similarities and discrepancies, between each instrument/method, observed in this report, originate from various factors influencing the detection:

1. The vertical resolution of each instrument has been shown to have a large impact in some detection methods. While methods including a linear interpolation between ranges (PM, bR) are not much impacted by the vertical resolution, SBI and SBLpt detection methods strongly depend on it (Fig. 3.2). The applied SBI rule is to take the first point with decreasing T, so that when the vertical resolution is high, small variations along the profile are observed resulting in a potential underestimation of the SBI height. The procedure for the SBI detection should hence be revised to overcome this problem. Similarly, for the SBLpt, the augmentation of the vertical resolution results in a higher determination uncertainty as multiple candidates along one profile then respect the criterion of vanishing θ gradient. This influence of the vertical resolution on the PBLH detection methods, also pointed out by Seidel et al., 2010, plays an important role in long-term trend analysis, as time series should respect a certain homogeneity. This is for instance what prevented us from computing trends on RS/SBI and RS/SBLpt, for which significant ruptures in the time series were observed due to changes of vertical resolution after new radiosonde models were introduced.

2. The retrieval temporal resolution greatly differs between each instrument, from 10 min for MWR up to 12 hours for RS. Some physical processes in the atmosphere have

a time resolution inferior or superior to the ones of the instruments. In the 30 min average of RALMO's profiles, many clouds may have formed, eddies developed and T raised or dropped, ultimately impacting the resulting variables' profiles. The 12 h resolution with RS does not allow to recover the PBLH dynamics and is hence more used as a reference/control for the other instruments.

3. The instruments are not subjects to external forcing the same way due to their different profile's acquisition methods and requirements. For instance, while RALMO is covered by a shed with a unique opening in the roof to let the laser beam go through, the radiometer is outdoor and hence subjected to being intensely heated by the sun. This results in the MWR T profiles being positively biased, especially during the day in summer. For an equivalent ground T (the one measured at the SMN station), a positive bias of the T profile ultimately results in an underestimation of the CBLH and CBL growth rate, as we observed in the different comparisons and climatologies involving the radiometer in this project. Discussions are undergoing at MeteoSwiss to find an effective way to tackle the problem (by post-correction of the T profile or through a more effective instrument's cooling). Additionally, MWR does not measure under rain, nor does RALMO which is further shut down in case of low cloud cover. The WP is strongly affected by noise problems at low altitude (ground clutter) and bird migrations in spring and autumn, at higher altitude, for which a correction, using the Gabor filter on the raw signal, could be brought in future work. The fact that the instruments are not able to detect the PBLH in all weather conditions make the comparison more difficult. A large increase of missing data is also observed for methods using the profiles from several instruments (e.g. bR methods, for which the T profile of RALMO or MWR is used jointly with wind data from WP).

4. The continuity criterion applied on RALMO/ASR (also applied on WP/SNR in Collaud Coen et al., 2014), has the advantage of providing a continuous layer less affected by strong signals such as passing clouds or local phenomenon of aerosols advection. On the other hand, one could also want to retrieve this more local phenomenon that could correspond to specific sub-layers. It is mostly for this reason that we decided not to use any continuity criterion for the WP/SNR method, so that local maximum of strong turbulences could be chosen over the larger standard diurnal cycles.

5. An effective way of assessing the uncertainties associated with each computed layer's height is through the propagation of the instruments' variance in the detection methods. This has been tried in this project but resulted in either an under or overestimation of the errors, relative to what one could expect in terms of PBL height variations. A more thorough computation of the errors associated with the PBLH determination is then needed to compare the results provided by each set of instrument and method. This will be achieved through a common definition of the instrument's error for each variable along the vertical profile.

The fact that some methods are applied similarly on instruments that are very different in some ways is a challenge that demands cautiousness. However, it has been shown with this project that each instrument/method plays a unique role in characterizing and understanding the PBL dynamics and its complex sub-layers structures.

An inter-comparison of the different instruments/methods, taking RS/PM at 11:30 as reference, has shown the good CBLH retrieval abilities of RALMO and the KENDA model, making them good candidates for PBLH long-term analyses. MWR, on the other hand,

has shown a clear tendency to under-estimate the CBLH and CBL growth rate in summer compared to RS, RALMO and KENDA, mostly due to the instrument's heating discussed earlier. Caution has to be drawn when using RALMO/ASR to retrieve the CBLH. Indeed, while this instrument/method has shown great results in estimating the CBLH, a time-lag was observed compared to PM and bR applied on RS and RALMO. This time-lag, up to 3 hours, highlighted the possible difference between the theoretical mixing layer height and the mixed layer height measured with aerosols concentration gradient. Other atmospheric effects could be at the origin of these observations, such as mesoscale flows or advections. The method applied on the WP/SNR in this project has shown important limitations in estimating the CBLH during the day, with a measured maximum of turbulence height most often found below the CBLH.

During the day on the Swiss plateau, it has been shown, among other findings, that the CBLH reaches a maximum in summer, between 12:00 and 14:00 ($\sim$ 2100 m a.s.l.) and a minimum during wintertime ($\sim$ 1000 m a.s.l.). Same goes for the CBL growth rate after sunrise, that is more rapid under the strong convective summer conditions characterized by steep increase in the vertical heat flux. A decrease in CBLH in June has been observed, with all instruments and methods. Although no definitive answers have been brought on the nature of these observations, hypotheses were made and further researches on that topic could help validate these hypotheses or formulate new ones. During the night, the results were more scattered and difficult to interpret due to a multi-layering of the PBL. Nonetheless, the stable boundary layer was well retrieved by RALMO and MWR, with the SBI being lower, at any time, than the SBLpt. The RL, retrieved with RALMO/ASR, has shown to be closely related to the CBLH^{Max}, as the extent of the former depends on the latter. WP/SNR however yielded a layer at constant annual height, close to the SBI, suggesting that the height of maximum turbulence during the night is constant throughout the year. Finally, the bR method applied on KENDA model, RALMO and MWR has shown to be incoherent during the night. The result of KENDA/bR are very close to the ground throughout the whole year due to the Ri_b threshold being rapidly attained in stable conditions. Meanwhile, the bR applied to RALMO and MWR are biased due to the lack of WP data near the ground, artificially rising the rarely detected layer to the first level of available wind measurement. Overall, the results that have been found for the Swiss Plateau relate to other studies in Europe, with differences attributed to site-dependant parameters (mean seasonal T, humidity, sunshine,...).

In this project, unlike most studies on the topic (Kotthaus et al., 2021), an important differentiation has been made between clear and cloudy sky conditions. During the day, it has been observed that an increase in cloudiness correlated with a decrease in the CBLH measured with RALMO, MWR and KENDA. Daily maximum of 2200, 2000 and 1500 m a.s.l. for respectively, clear, cloudy and very cloudy sky conditions were observed using KENDA/bR in Payerne. During the night, it appeared that cloudiness didn't have a significant impact of the sub-layers heights of the nocturnal-PBL. While conditions of clear and cloudy sky were mostly discussed throughout this project, very-clear and very-cloudy conditions were also tested ($\leq$ 1 okta and $\geq$ 7 okta, respectively). Unfortunately, these conditions were quite limiting for the number of available data and only KENDA/bR had a sufficient data availability to allow the use of these 2 extreme conditions. RALMO has often been used as a reference instrument in this project for its great comparison with RS; however, its incapacity to measure under low cloud cover raises the question of which instrument should be used as reference in cloudy sky conditions. Then, MWR is probably sufficient, as it is also less impacted by artifacts due to instrument's heating when a cloud cover is present.

In the light of these project's results and the discussion above, the author concludes

that RALMO is probably the most reliable instrument available in Payerne to detect the atmospheric boundary layers and its sub-layers. Indeed, the retrieved T and RH profiles make it possible to use the PM and bR method to detect the CBLH during the day. During the night, the SBI and SBLpt methods are used on the T profiles to detect the stable layer and the ASR is used to detect the RL. Nonetheless, using the bR method during the night provided incoherent and hardly analysable results. A combination of instruments working in parallel is nonetheless preferred, so that profiles can be compared and validated to allow a PBLH detection under all kind of weather.

Further researches should hence be directed towards enlarging the data set available for computation and solving the main problems addressed in this report. This includes statistical analyses to assess the different correlations between each variable and their role in the PBL dynamic. Additionally, a similar long-term climatology study would be interesting for mountainous terrain, for which the PBL behaviour is very different than the one for flat topography. Unfortunately, instruments such as RALMO and RS are only available at Payerne for the moment, but ongoing studies at MeteoSwiss aim to implement an automatic PBLH detection using ceilometers CL31's aerosols backscattering profiles, across Switzerland (including in the Alps).

Bibliography

Allabakash, S., P. Yasodha, L. Bianco, S. Venkatramana Reddy, P. Srinivasulu, and S. Lim (2017). "Improved boundary layer height measurement using a fuzzy logic method: Diurnal and seasonal variabilities of the convective boundary layer over a tropical station". In: *Journal of Geophysical Research: Atmospheres* 122 (17), pp. 9211–9232. ISSN: 21698996. DOI: 10.1002/2017JD027615.

Angevine, W.M., A.B. White, and S.K. Avery (1994). "Boundary-layer depth and entrainment zone characterization with a boundary-layer profiler". In: *Boundary-Layer Meteorology* 68 (4). ISSN: 0006-8314. DOI: 10.1007/BF00706797.

Baars, H., A. Ansmann, R. Engelmann, and D. Althausen (2008). "Continuous monitoring of the boundary-layer top with lidar". In: *Atmos. Chem. Phys* 8, pp. 7281–7296. URL: www.atmos-chem-phys.net/8/7281/2008/.

Barrera, Y.D., T. Nehrkorn, J. Hegarty, M. Sargent, J. Benmergui, E. Gottlieb, S.C. Wofsy, P. DeCola, L. Hutyra, and T. Jones (2019). "Using Lidar Technology To Assess Urban Air Pollution and Improve Estimates of Greenhouse Gas Emissions in Boston". In: *Environmental Science and Technology* 53.15, pp. 8957–8966. DOI: 10.1021/acs.est.9b00650.

Barton, Y. (2015). *Comparison of planetary boundary layer height measured by radio-sounding and estimated by COSMO-2*. Internship project at MeteoSwiss.

Bruno, D. and R. Philipona (2004). "Automatic amount detection by surface longwave downward radiation measurements". In: *Journal of Geophysical Research* 109. DOI: 10.1029/2003JD004182.

Calpini, B., D. Ruffieux, J. M. Bettems, C. Hug, P. Huguenin, H. P. Isaak, P. Kaufmann, O. Maier, and P. Steiner (2011). "Ground-based remote sensing profiling and numerical weather prediction model to manage nuclear power plants meteorological surveillance in Switzerland". In: *Atmospheric Measurement Techniques* 4 (8), pp. 1617–1625. ISSN: 18671381. DOI: 10.5194/amt-4-1617-2011.

Camilo, R.S., S. Wharton, J. Vilà-Guerau de Arellano, K.T. Paw, K.S. Hemes, J.D. Fuentes, J. Osuna, D. Szutu, J.V. Ribeiro, J. Verfaillie, and D. Baldocchi (2021). "Evaluation of Atmospheric Boundary Layer Height From Wind Profiling Radar and Slab Models and Its Responses to Seasonality of Land Cover, Subsidence, and Advection". In: *Journal of Geophysical Research: Atmospheres* 126 (7). ISSN: 21698996. DOI: 10.1029/2020JD033775.

Cimini, D., F. de Angelis, J.-C. Dupont, S. Pal, and M. Haeffelin (2013). "Mixing layer height retrievals by multichannel microwave radiometer observations". In: *Atmospheric Measurements Techniques, European Geosciences Union* 6 (11), pp. 2941–2951. DOI: 10.5194/amt-6-2941-2013.

Cimini, D., M. Haeffelin, S. Kotthaus, U. Löhnert, P.Martinet, E. O'Connor, C. Walden, M. Collaud Coen, and J. Preissler (2020). "Towards the profiling of the atmospheric boundary layer at European scale—introducing the COST Action PROBE". In: *Bulletin of Atmospheric Science and Technology* 1 (1). ISSN: 2662-1495. DOI: 10.1007/s42865-020-00003-8.

Collaud Coen, M., E. Andrews, A. Bigi, G. Martucci, G. Romanens, F.P.A. Vogt, and L. Vuilleumier (2020a). "Effects of the prewhitening method, the time granularity, and the time segmentation on the Mann-Kendall trend detection and the associated Sen's

slope". In: *Atmospheric Measurement Techniques* 13 (12), pp. 6945–6964. ISSN: 18678548. DOI: 10.5194/amt-13-6945-2020.

Collaud Coen, M., E. Andrews, A. Lastuey, T.P. Arsov, J. Backman, B.T. Brem, N. Bukowiecki, C. Couret, K. Eleftheriadis, H. Flentje, M. Fiebig, M. Gysel-Beer, J.L. Hand, A. Hoffer, R. H., C. Hueglin, W. Joubert, M. Keywood, J.E. Kim, S.W. Kim, C. Labuschagne, N.H. Lin, Y. Lin, C.L. Myhre, K. Luoma, H. Lyamani, A. Marinoni, O.L. Mayol-Bracero, N. Mihalopoulos, M. Pandolfi, N. Prats, A.J. Prenni, J.P. Putaud, L. Ries, F. Reisen, K. Sellegri, S. Sharma, P.k Sheridan, J.P. Sherman, J. Sun, G. Titos, E. Torres, T. Tuch, R. Weller, A. Wiedensohler, P. Zieger, and P. Laj (2020b). "Multidecadal trend analysis of in situ aerosol radiative properties around the world". In: *Atmospheric Chemistry and Physics* 20 (14), pp. 8867–8908. ISSN: 16807324. DOI: 10.5194/acp-20-8867-2020.

Collaud Coen, M., C. Praz, A. Haefele, D. Ruffieux, P. Kaufmann, and B. Calpini (2014). "Determination and climatology of the planetary boundary layer height above the Swiss plateau by in situ and remote sensing measurements as well as by the COSMO-2 model". In: *Atmospheric Chemistry and Physics* 14 (23), pp. 13205–13221. ISSN: 16807324. DOI: 10.5194/acp-14-13205-2014.

Collaud Coen, M., E. Weingartner, M. Furger, S. Nyeki, A.S.H. Prévôt, M. Steinbacher, and U. Baltensperger (2011). "Aerosol climatology and planetary boundary influence at the Jungfraujoch analyzed by synoptic weather types". In: *Atmospheric Chemistry and Physics* 11, pp. 5931–5944. DOI: 10.5194/acp-11-5931-2011.

Compton, J.C., R. Delgado, T.A. Berkoff, and R.M. Hoff (2013). "Determination of planetary boundary layer height on short spatial and temporal scales: A demonstration of the covariance wavelet transform in ground-based wind profiler and lidar measurements". In: *Journal of Atmospheric and Oceanic Technology* 30 (7), pp. 1566–1575. DOI: 10.1175/JTECH-D-12-00116.1.

Dinoev, T., V. B. Simeonov, Y. Arshinov, S. Bobrovnikov, P. Ristori, B. Calpini, M. Parlange, and H. Van Den Bergh (2013). "Raman Lidar for Meteorological Observations, RALMO - Part 1: Instrument description". In: *Atmospheric Measurement Techniques* 6 (5), pp. 1329–1346. ISSN: 18671381. DOI: 10.5194/amt-6-1329-2013.

Du, L., Y. Pan, and W. Wang (2020). "Random sample fitting method to determine the planetary boundary layer height using satellite-based lidar backscatter profiles". In: *Remote Sensing* 12 (23), pp. 1–18. ISSN: 20724292. DOI: 10.3390/rs12234006.

Díaz, J.P., F.J. Expósito, J.C. Pérez, A. González, Y. Wang, L. Haimberger, and J. Wang (2019). "Long-term trends in marine boundary layer properties over the Atlantic Ocean". In: *Journal of Climate* 32 (10), pp. 2991–3004. ISSN: 08948755. DOI: 10.1175/JCLI-D-18-0219.1.

Emeis, S., K. Schaefer, C. Münkel, R. Friedl, and P. Suppan (2012). "Evaluation of the Interpretation of Ceilometer Data with RASS and Radiosonde Data". In: *Boundary-Layer Meteorology* 143, pp. 25–35. DOI: 10.1007/s10546-011-9604-6.

Guo, J., Y. Li, J. Blake Cohen, J. Li, D. Chen, H. Xu, L. Liu, J. Yin, K. Hu, and P. Zhai (2019). "Shift in the Temporal Trend of Boundary Layer Height in China Using Long-Term (1979–2016) Radiosonde Data". In: *Geophysical Research Letters* 46 (11), pp. 6080–6089. ISSN: 19448007. DOI: 10.1029/2019GL082666.

Haefele, A. and D. Ruffieux (2015). "Validation of the 1290 MHz wind profiler at Payerne, Switzerland, using radiosonde GPS wind measurements". In: *Meteorological Applications* 22, pp. 873–878. ISSN: 14698080. DOI: 10.1002/met.1507.

Haeffelin, M., F. Angelini, Y. Morille, G. Martucci, S. Frey, G.P. Gobbi, S. Lolli, C. O'Dowd, L. Sauvage, and I. Xueref-Remy (2012). "Evaluation of mixing-height retrievals from automatic profiling lidars and ceilometers in view of future integrated networks in Europe". In: *Boundary-layer meteorology* 143, pp. 49–75.

Herrera, L. and C.D. Hoyos (2019). "Characterization of the atmospheric boundary layer in a narrow tropical valley using remote-sensing and radiosonde observations and the WRF model: the Aburrá Valley case-study". In: *Quarterly Journal of the Royal Meteorological Society* 145 (723), pp. 2641–2665. ISSN: 1477870X. DOI: 10.1002/qj.3583.

Hervo, M. (2020). *Ceilometer Klosters*. DOI: http://dx.doi.org/10.16904/envidat.127. URL: https://www.envidat.ch/dataset/ceilometer-klosters.

Hirsch, R.M., J.R. Slack, and R.A. Smith (1982). "Techniques of trend analysis for monthly water quality data". In: *Water Resources Research* 18.1, pp. 107–121. DOI: https://doi.org/10.1029/WR018i001p00107.

Holzworth, G.C. (1964). "Estimates of mean maximum mixing depths in the contiguous united states". In: *Monthly Weather Review* 92 (5), pp. 235–242.

Huth, R., C. Beck, and M. Kučerová (Dec. 2015). "Synoptic-climatological evaluation of the classifications of atmospheric circulation patterns over Europe". In: *International Journal of Climatology* 36. DOI: 10.1002/joc.4546.

Hägeli, P., D. G. Steyn, and K. B. Strawbridge (2000). "Spatial And Temporal Variability Of Mixed-Layer Depth And Entrainment Zone Thickness". In: *Boundary-Layer Meteorology* 97 (1). ISSN: 0006-8314. DOI: 10.1023/A:1002790424133.

Jeannet, P. (2018). *Comparison of Vaisala RS41 and RS92 radiosondes at Payerne, as well as comparisons with the Swiss radiosondes SRS-C50, SRS-C34 and SRS-400*. MeteoSwiss, Payerne.

Jeannet, P., R. Philipona, and H. Richner (2016). *Swiss upper-air balloon soundings since 1902*. Vdf Hochschulverlag.

Jeričević, A. and B. Grisogono (2006). "The critical bulk Richardson number in urban areas: Verification and application in a numerical weather prediction model". In: *Tellus, Series A: Dynamic Meteorology and Oceanography* 58 (1), pp. 19–27. ISSN: 02806495. DOI: 10.1111/j.1600-0870.2006.00153.x.

Jin, S., Y. Ma, W. Gong, B. Liu, L. Lei, and R. Fan (2021). "Characteristics of vertical atmosphere based on five-year microwave remote sensing data over Wuhan region". In: *Atmospheric Research* 260, p. 105710. ISSN: 0169-8095. DOI: https://doi.org/10.1016/j.atmosres.2021.105710.

Kotthaus, S., J.A. Bravo-Aranda, M. Collaud Coen, M. Haeffelin, and D. Ciminidi (2021). "Atmospheric boundary layer height from ground-based remote sensing: capabilities and limitations". In: *In preparation*.

Kotthaus, S., M. Haeffelin, M.A. Drouin, J.C. Dupont, S. Grimmond, A. Haefele, M. Hervo, Y. Poltera, and M. Wiegner (2020). "Tailored Algorithms for the Detection of the Atmospheric Boundary Layer Height from Common Automatic Lidars and Ceilometers (ALC)". In: *Remote Sensing* 12.19. ISSN: 2072-4292. DOI: 10.3390/rs12193259.

Lehmann, V. (2012). "Optimal Gabor-frame-expansion-based intermittent-clutter-filtering method for radar wind profiler". In: *Journal of Atmospheric and Oceanic Technology* 29 (2), pp. 141–158. ISSN: 07390572. DOI: 10.1175/2011JTECHA1460.1.

Li, J., Y. Chu, X. Li, and Y. Dong (2020). "Long-term trends of global maximum atmospheric mixed layer heights derived from radiosonde measurements". In: *Environmental Research Letters* 15 (3). ISSN: 17489326. DOI: 10.1088/1748-9326/ab7952.

Li, Y., J. Li, Y. Zhao, M. Lei, Y. Zhao, B. Jian, M. Zhang, and J. Huang (2021). "Long-term variation of boundary layer height and possible contribution factors: A global analysis". In: *Science of The Total Environment* 796, p. 148950. ISSN: 0048-9697. DOI: https://doi.org/10.1016/j.scitotenv.2021.148950.

Li, Z., J. Guo, A. Ding, H. Liao, J. Liu, Y. Sun, T. Wang, H. Xue, H. Zhang, and B. Zhu (2017). "Aerosol and Boundary-Layer Interactions and Impact on Air Quality". In: *National Science Review* 4, 810–833. DOI: 10.1093/nsr/nwx117.

Liu, B., Yingying Ma, Jianping Guo, Wei Gong, Yong Zhang, Feiyue Mao, Jian Li, Xiaoran Guo, and Yifan Shi (2019). "Boundary layer heights as derived from ground-based radar

wind profiler in Beijing". In: *IEEE Transactions on Geoscience and Remote Sensing* 57 (10), pp. 8095–8104. ISSN: 15580644. DOI: 10.1109/TGRS.2019.2918301.

Löhnert, U. and O. Maier (2012). "Operational profiling of temperature using ground-based microwave radiometry at Payerne: Prospects and challenges". In: *Atmospheric Measurement Techniques* 5 (5), pp. 1121–1134. ISSN: 18671381. DOI: 10.5194/amt-5-1121-2012.

Martinet, P., D. Cimini, F. Burnet, B. Ménétrier, Y. Michel, and V. Unger (2020). "Improvement of numerical weather prediction model analysis during fog conditions through the assimilation of ground-based microwave radiometer observations: A 1D-Var study". In: *Atmospheric Measurement Techniques* 13 (12), pp. 6593–6611. ISSN: 18678548. DOI: 10.5194/amt-13-6593-2020.

Martinet, P., A. Dabas, J.M. Donier, T. Douffet, O. Garrouste, and R. Guillot (2015). "1D-Var temperature retrievals from microwave radiometer and convective scale model". In: *Tellus, Series A: Dynamic Meteorology and Oceanography* 6 (1). ISSN: 16000870. DOI: 10.3402/tellusa.v67.27925.

Martucci, G., F. Navas-Guzmán, L. Renaud, G. Romanens, S.M. Gamage, M. Hervo, P. Jeannet, and A. Haefele (2021). "Validation of pure rotational Raman temperature data from the Raman Lidar for Meteorological Observations (RALMO) at Payerne". In: *Atmos. Meas. Tech* 14, pp. 1333–1353. DOI: 10.5194/amt-14-1333-2021. URL: https://doi.org/10.5194/amt-14-1333-2021.

Molod, A., H. Salmun, and A.B. Marquardt Collow (2019). "Annual Cycle of Planetary Boundary Layer Heights Estimated From Wind Profiler Network Data". In: *Journal of Geophysical Research: Atmospheres* 124 (12), pp. 6207–6221. ISSN: 21698996. DOI: 10.1029/2018JD030102.

Moreira, G.d.A., J.L. Guerrero-Rascado, J.A. Bravo-Aranda, I. Foyo-Moreno, A. Cazorla, I. Alados, H. Lyamani, E. Landulfo, and L. Alados-Arboledas (2020). "Study of the planetary boundary layer height in an urban environment using a combination of microwave radiometer and ceilometer". In: *Atmospheric Research* 240. ISSN: 01698095. DOI: 10.1016/j.atmosres.2020.104932.

Pal, S. and M. Haeffelin (2015). "Forcing mechanisms governing diurnal, seasonal, and interannual variability in the boundary layer depths: Five years of continuous lidar observations over a suburban site near Paris". In: *Journal of Geophysical Research* 120 (23), pp. 11,936–11,956. ISSN: 21562202. DOI: 10.1002/2015JD023268.

Pasquier, J. (2018). *Cloud Cover Detection and its Automation*. Internship project at MeteoSwiss.

Philipp, A., C. Beck, R. Huth, and J. Jacobeit (Mar. 2014). "Development and comparison of circulation type classifications using the COST 733 dataset and software". In: *International Journal of Climatology* 36. DOI: 10.1002/joc.3920.

Pielke, R.A. (2001). "Influence of the spatial distribution of vegetation and soils on the prediction of cumulus Convective rainfall". In: *Reviews of Geophysics* 39.2, pp. 151–177. DOI: https://doi.org/10.1029/1999RG000072.

Praz, C. (2013). "Automatic planetary boundary layer detection: validation of various detection instruments and methods, comparison with the forecast model Cosmo-2 and one-year climatology". Master thesis, Swiss Federal Institute of Technology.

Richardson, H., S. Basu, and A.A.M. Holtslag (2013). "Improving Stable Boundary-Layer Height Estimation Using a Stability-Dependent Critical Bulk Richardson Number". In: *Boundary-Layer Meteorology* 148 (1), pp. 93–109. ISSN: 00068314. DOI: 10.1007/s10546-013-9812-3.

Rihani, J.F., F.K. Chow, and R.M. Maxwell (2015). "Isolating effects of terrain and soil moisture heterogeneity on the atmospheric boundary layer: Idealized simulations to diagnose land-atmosphere feedbacks". In: *Journal of Advances in Modeling Earth Systems* 7.2, pp. 915–937. DOI: https://doi.org/10.1002/2014MS000371.

Schraff, C., H. Reich, A. Rhodin, A. Schomburg, K. Stephan, A. Periáñez, and R. Potthast (2016). "Kilometre-scale ensemble data assimilation for the COSMO model (KENDA)". In: *Quarterly Journal of the Royal Meteorological Society* 142 (696), pp. 1453–1472. ISSN: 1477870X. DOI: 10.1002/qj.2748.

Seidel, D.J., C.O. Ao, and K. Li (2010). "Estimating climatological planetary boundary layer heights from radiosonde observations: Comparison of methods and uncertainty analysis". In: *Journal of Geophysical Research Atmospheres* 115 (16). ISSN: 01480227. DOI: 10.1029/2009JD013680.

Seidel, D.J., Y. Zhang, A. Beljaars, J.C. Golaz, A.R. Jacobson, and B. Medeiros (2012). "Climatology of the planetary boundary layer over the continental United States and Europe". In: *Journal of Geophysical Research Atmospheres* 117 (17). ISSN: 01480227. DOI: 10.1029/2012JD018143.

Sivaraman, C., S. Mcfarlane, E. Chapman, M. Jensen, T. Toto, S. Liu, and M. Fischer (2013). *Planetary Boundary Layer (PBL) Height Value Added Product (VAP): Radiosonde Retrievals*. DOI: DOE/SC-ARM/TR-132.

Stull, R.B. (1998). *An Introduction to Boundary Layer Meteorology*. Kluwer Academic Publishers.

Szintai, B. (2010). "Improving the turbulence coupling between high resolution numerical weather prediction and Lagrangian particle dispersion models". PhD thesis, Swiss Federal Institute of Technology.

Weatherhead, B., G. Reinsel, G. Tiao, C. Jackman, S. Firth, J. DeLuisi, T. Keller, S. Oltmans, E. Fleming, D. Wuebbles, J. Kerr, and A. Miller (2000). "Detecting the recovery of total column ozone". In: *Journal of Geophysical Research* 105, pp. 22201–22210. DOI: 10.1029/2000JD900063.

Wilczak, J.M., R.G. Strauch, F.M. Ralph, B.L. Weber, D.A. Merritt, J.R. Jordan, D.E. Wolfe, L.K. Lewis, D.B. Wuertz, J.E. Gaynor, S.A. McLaughlin, R.R. Rogers, A.C. Riddle, and T.S. Dye (1995). "Contamination of Wind Profiler Data by Migrating Birds: Characteristics of Corrupted Data and Potential Solutions". In: *Journal of Atmospheric and Oceanic Technology* 12.3, pp. 449 –467. DOI: 10.1175/1520-0426(1995)012<0449:COWPDB>2.0.CO;2.

WMO (2008). *Guide to Meteorological Instruments and Methods of Observation (Seventh edition)*. WMO Publications Board.

Yue, S., P. Pilon, B. Phinney, and G. Cavadias (2002). "The influence of autocorrelation on the ability to detect trend in hydrological series". In: *Hydrological Processes* 16.9, pp. 1807–1829. DOI: https://doi.org/10.1002/hyp.1095.

Zhang, Y., Z. Gao, D. Li, Y. Li, N. Zhang, X. Zhao, and J. Chen (2014). "On the computation of planetary boundary-layer height using the bulk Richardson number method". In: *Geoscientific Model Development* 7 (6), pp. 2599–2611. ISSN: 19919603. DOI: 10.5194/gmd-7-2599-2014.

Zhang, Y., D.J. Seidel, and S. Zhang (2013). "Trends in planetary boundary layer height over europe". In: *Journal of Climate* 26 (24), pp. 10071–10076. ISSN: 08948755. DOI: 10.1175/JCLI-D-13-00108.1.

Appendix A

Methodology

A.1 Computation of mass mixing ratio

From water vapour density (measured by the MWR) to relative humidity (WMO, 2008):

$$RH = \frac{\rho \cdot R \cdot T}{M_w \cdot e_{ww}} \tag{A.1}$$

where ρ is the water vapour density $[g/m^3]$, R is the molar gas constant, M_w is the molar mass of water and e_{ww} is the saturation vapour pressure of humid air over water.

$$e_{ww} = f \cdot e_w = \left(1.0016 + 3.15^{-6} p - \frac{0.074}{p}\right) \cdot \left(6.112 \cdot exp^{\left(\frac{17.62T}{243.12+T}\right)}\right) \tag{A.2}$$

where f is the pressure factor and e_w the saturation vapour pressure in pure phase over water.

From relative humidity (measured by RS) to mass mixing ratio:

$$r = \frac{M_w \cdot RH \cdot e_s}{M_a(p - RH \cdot e_s)} \tag{A.3}$$

where M_w and M_a are the molar mass of water and air respectively and e_s is the saturation water vapour over liquid water for a given T and r is the mass mixing ratio.

$$e_s \approx 1010.25 \cdot 10^{10.80\frac{1-T_k}{T} - 5.03 \cdot log_{10}(\frac{T}{T_k}) + 1.50 \cdot 10^{-4}(1 - 10^{-8.30\frac{T}{T_k - 1}}) + 0.43 \cdot 10^{-3}(10^{4.77\frac{1-T_k}{T}} - 1) - 2.22} \tag{A.4}$$

where T_k is the triple point of water in Kelvin (273.16 K).

From specific humidity (measured by RALMO) to mass mixing ratio:

$$r = \frac{SH \cdot 1000}{1000 - SH} \tag{A.5}$$

where SH is the specific humidity and r is the mass mixing ratio.

A.2 Error propagation calculations

Error from pressure estimation: (See Eq. 3.3 for the estimation of p)

$$\Delta p = \left|\frac{\partial p}{\partial T}\right| \Delta T = \left|\frac{-p \cdot M_a \cdot g}{R \cdot T}\right| \Delta T \tag{A.6}$$

Error from θ computation: (See Eq. 3.1 for the definition of θ)

$$\Delta\theta = \left|\frac{\partial \theta}{\partial T}\right| \Delta T + \left|\frac{\partial \theta}{\partial p}\right| \Delta p = \left|\left(\frac{p_{ref}}{p}\right)^{0.286}\right| \Delta T + \left|T \cdot p_{ref}^{0.286} \cdot (-0.286) \cdot p^{-1.286}\right| \Delta p \tag{A.7}$$

Error from θ_v computation: (See Eq. 3.2 for the definition of θ_v)

$$\Delta\theta_v = \left|\frac{\partial \theta_v}{\partial \theta}\right| \Delta\theta + \left|\frac{\partial \theta_v}{\partial r}\right| \Delta r = |(1 + 0.61 \cdot r)|\, \Delta\theta + |\theta \cdot 0.61|\, \Delta r \tag{A.8}$$

Error from bR_i computation: (See Eq. 3.4 for the definition of bR_i)

$$\begin{aligned} \Delta bR_i &= \left|\frac{\partial bR_i}{\partial \theta}\right| \Delta\theta + \left|\frac{\partial bR_i}{\partial U}\right| \Delta U + \left|\frac{\partial bR_i}{\partial V}\right| \Delta V \\ &= \left|\frac{gz(\theta^2 - \theta + \theta_0)}{\theta^2(U^2+V^2)}\right| \Delta\theta + \left|\frac{-2gzU(\theta - \theta_0)}{\theta(U^2+V^2)^2}\right| \Delta U + \left|\frac{-2gzV(\theta - \theta_0)}{\theta(U^2+V^2)^2}\right| \Delta V \end{aligned} \tag{A.9}$$

A.3 Error climatology

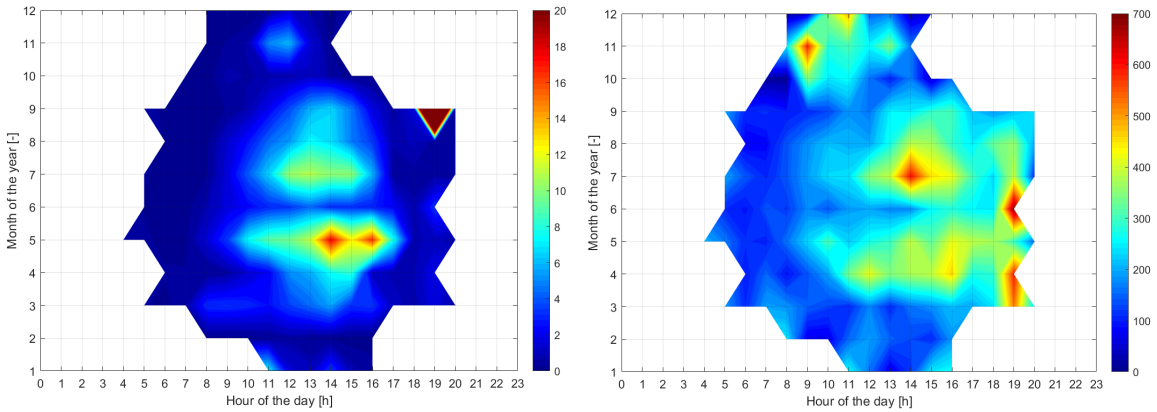

(A) PM based on 1^{st} method.

(B) PM based on 2^{nd} method.

FIGURE A.1: Climatology of the PBLH error from computation with 1^{st} and 2^{nd} method on RALMO/PM, for clear sky conditions in Payerne.

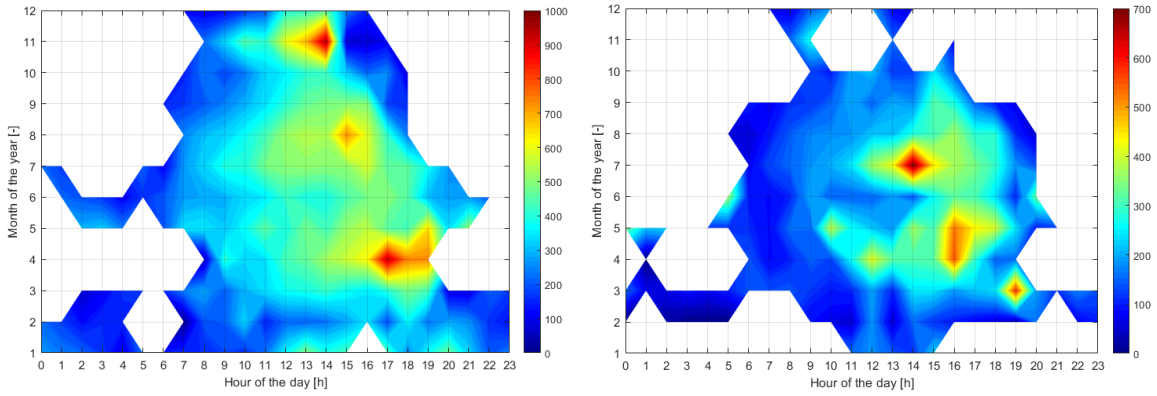

(A) MWR/bR.

(B) RALMO/bR.

FIGURE A.2: Climatology of the PBLH error from computation with bR method on MWR and RALMO, for clear sky conditions in Payerne.

Appendix B

Results

B.1 Potential vs. virtual potential temperature

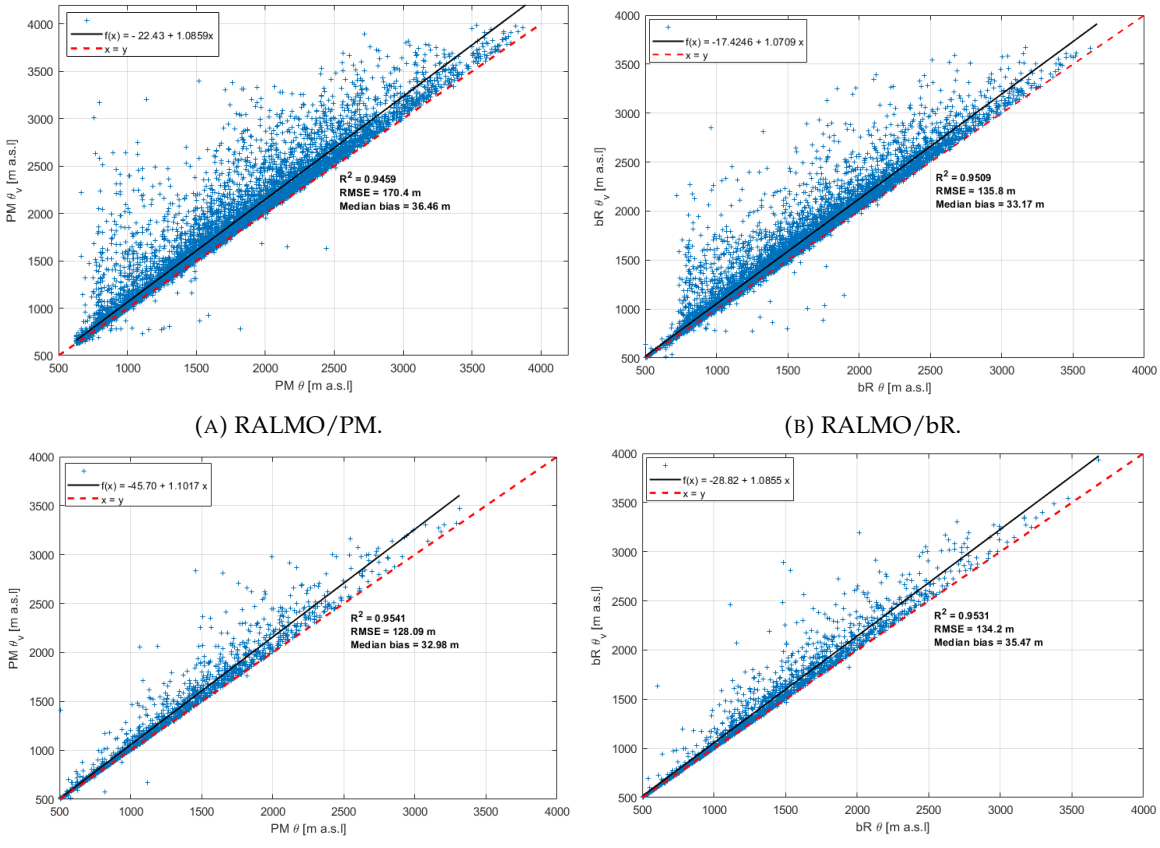

(A) RALMO/PM.

(B) RALMO/bR.

(C) RS/PM.

(D) RS/bR.

FIGURE B.1: Scatter plots of PBLH retrieved with PM and bR applied on potential (x-axis) and virtual potential (y-axis) temperature with RALMO and RS in Payerne (2016-2020). A linear fit is applied on the data (black line) with correlation coefficient R^2 and Root Mean Square Error $RMSE$. The 1:1 linear relation ($x = y$, red dashed line) is used to visually assess the deviation of the data. The median bias between θ_v and θ is also given.

B.2 Comparison instruments/methods

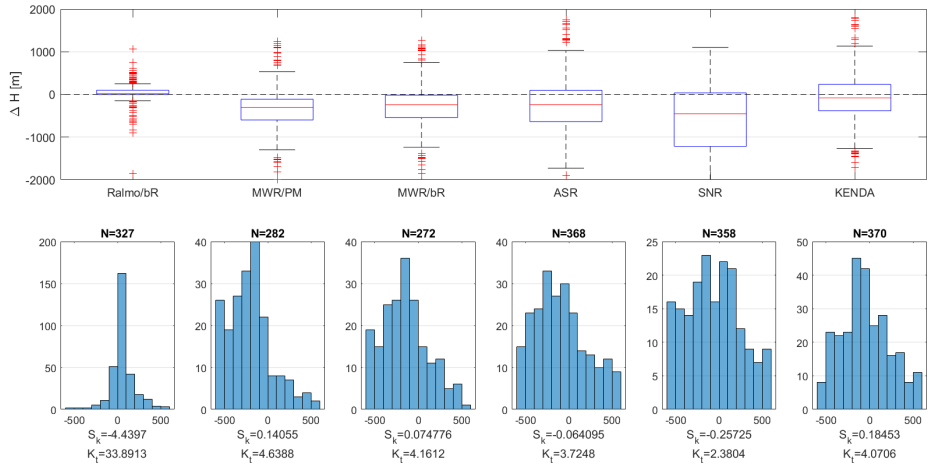

FIGURE B.2: Comparison between RALMO/PM and the other instruments/methods taking the median between 12:00 and 15:00 in 2016-2020 for clear sky days in Payerne. See Fig. 5.3 for legend description.

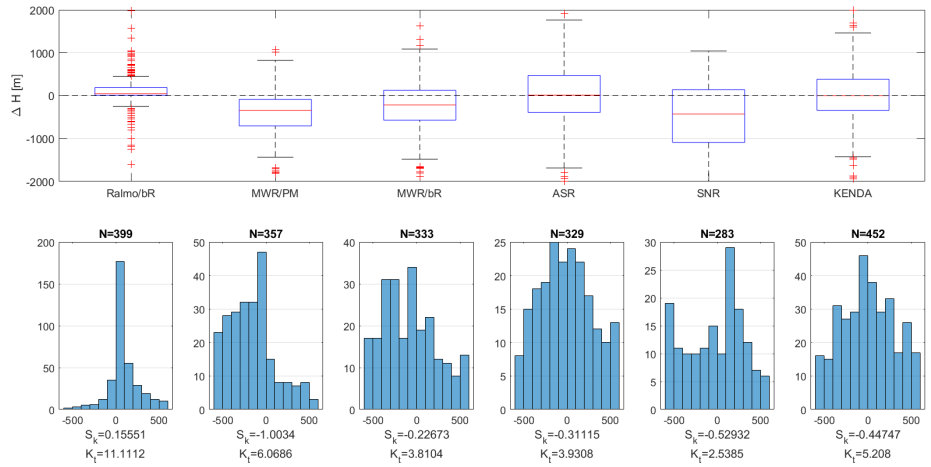

FIGURE B.3: Comparison between RALMO/PM and the other instruments/methods taking the median between 12:00 and 15:00 in 2016-2020 for cloudy sky days in Payerne. See Fig. 5.3 for legend description.

B.3 Climatology

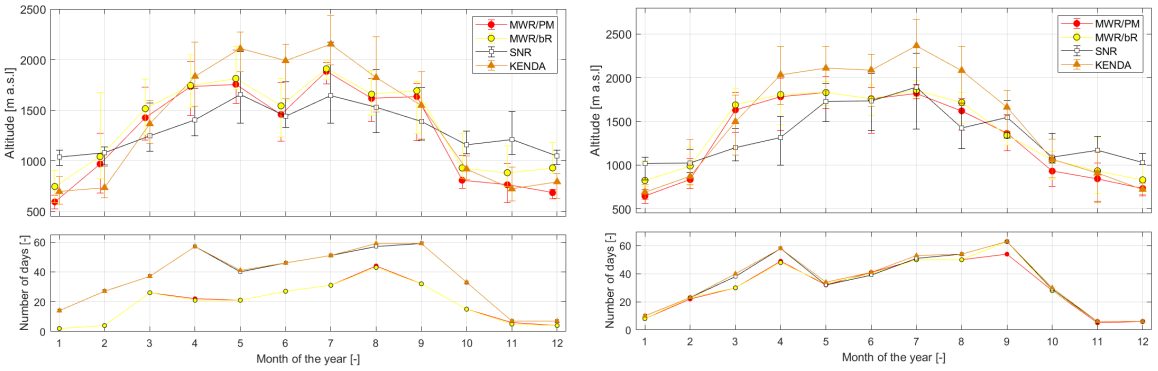

(A) Grenchen station (B) Schaffhausen station

FIGURE B.4: Climatology (2016-2020) of the CBLH^{Max} taking the monthly median of the median between 12:00 and 15:00, for clear sky conditions in Grenchen and Schaffhausen stations. The "error bars" correspond to the quantiles 25 and 75%. Lower panel: number of monthly cases.

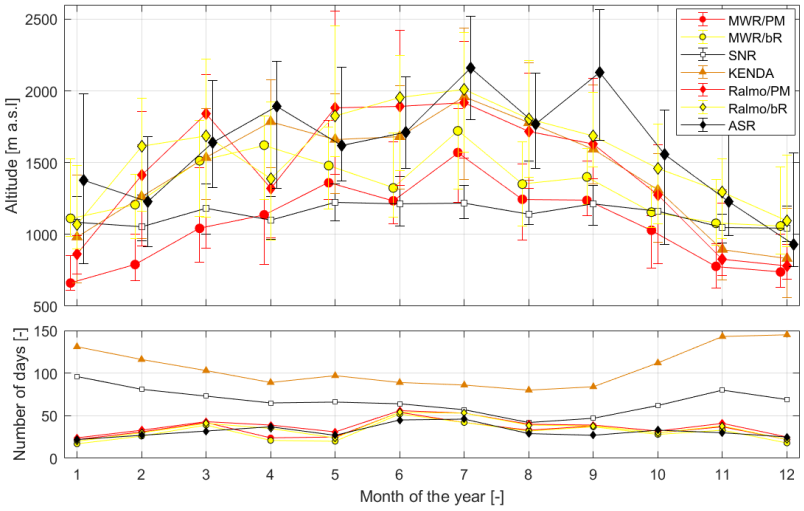

FIGURE B.5: Same climatology than in Fig. 5.5b, where MWR is restricted to the same cases as RALMO.

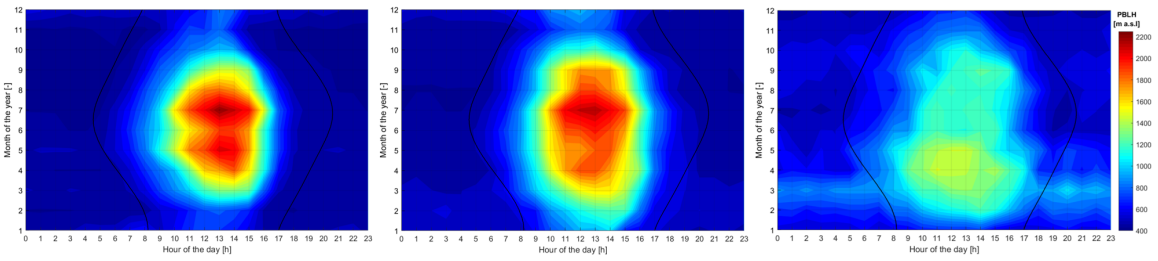

FIGURE B.6: Climatology (2016-2020) using KENDA/bR in **Grenchen**. From left to right: clear, cloudy and very cloudy sky conditions. The black curved lines indicate sunrise and sunset hours throughout the months.

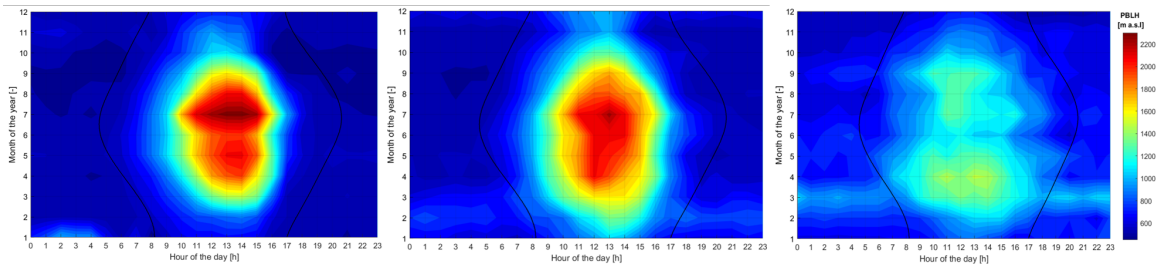

FIGURE B.7: Climatology (2016-2020) using KENDA/bR in **Schaffhausen**. From left to left: clear, cloudy and very cloudy sky conditions. The black curved lines indicate sunrise and sunset hours throughout the months.

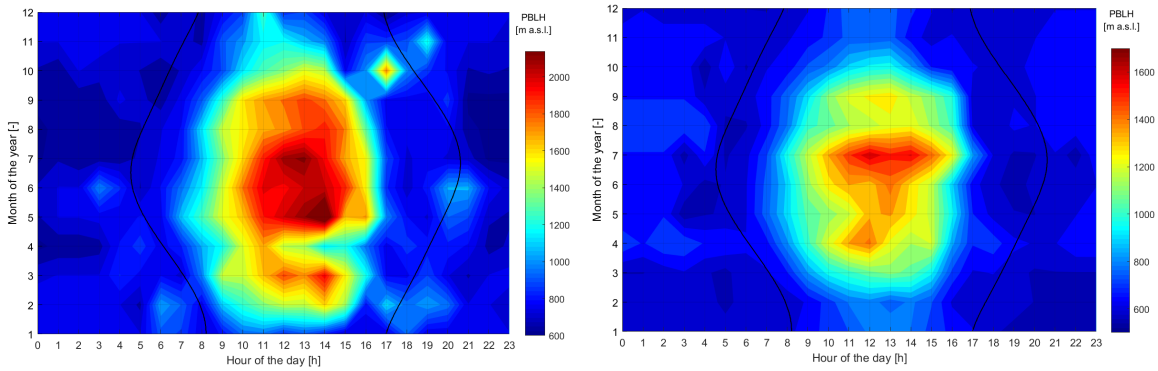

(A) RALMO SBI + PM

(B) MWR SBI + PM

FIGURE B.8: Climatology (2016-2020) using SBI during the night and PM during the day, with RALMO (left) and MWR (right), in Payerne for cloudy sky conditions. See Fig. 5.8 for legend description.

B.4 June CBLH decrease

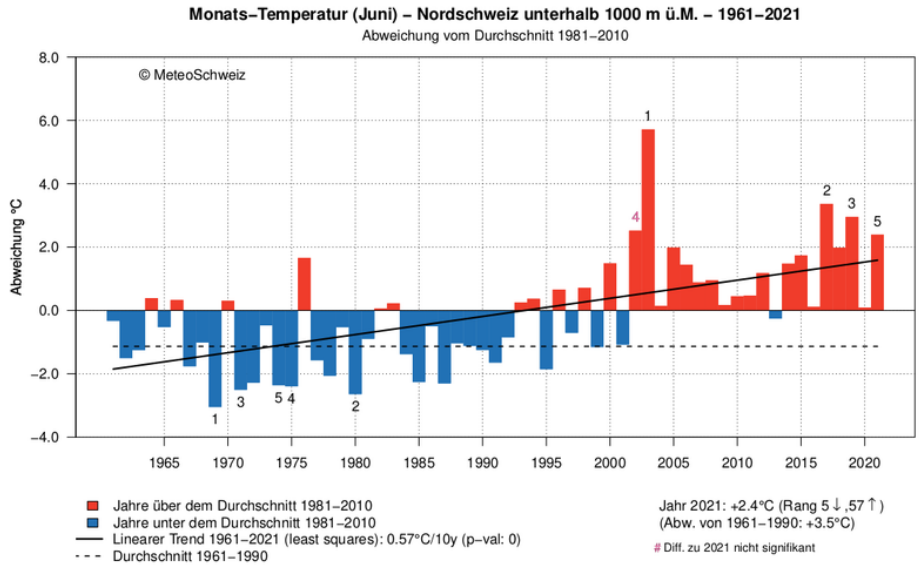

FIGURE B.9: Monthly T deviation from the average in June, with a reference period from 1981 to 2010, for northern Switzerland (altitude < 1000 m a.s.l.). Source: MeteoSwiss - ClimateBrowser.

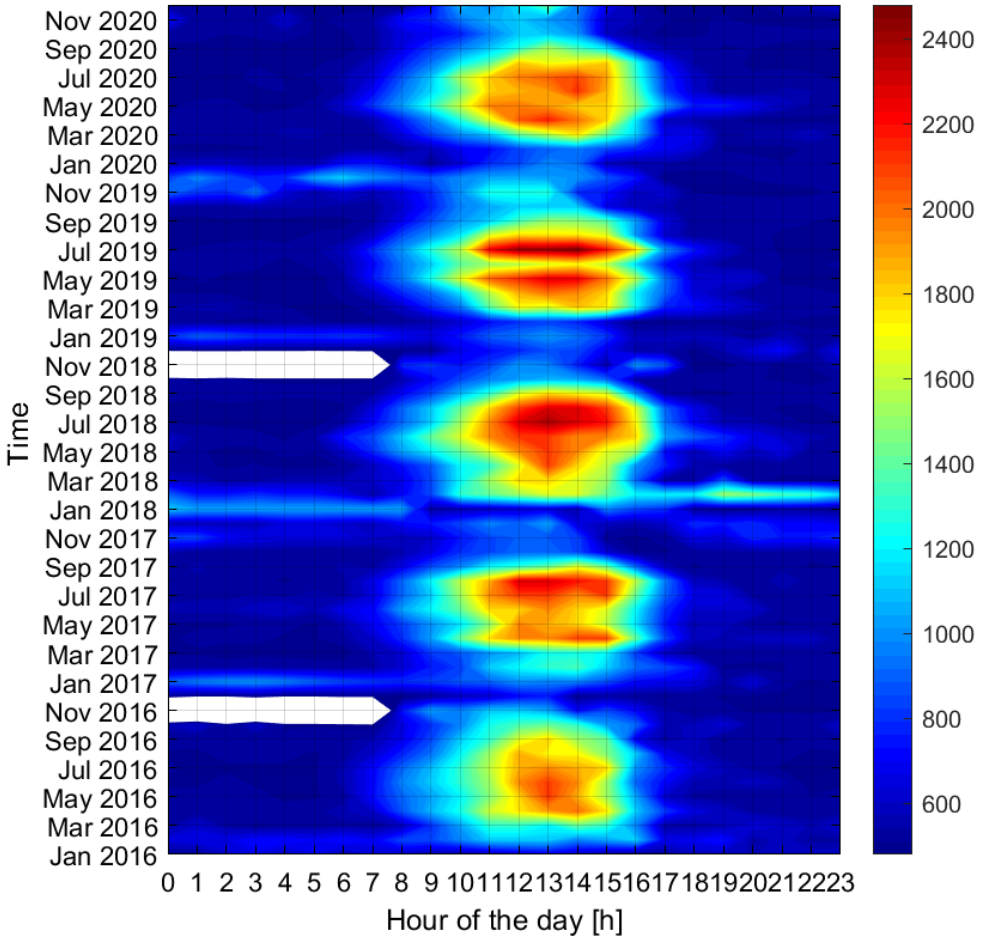

FIGURE B.10: Climatology (2016-2020) using KENDA/bR in Payerne.

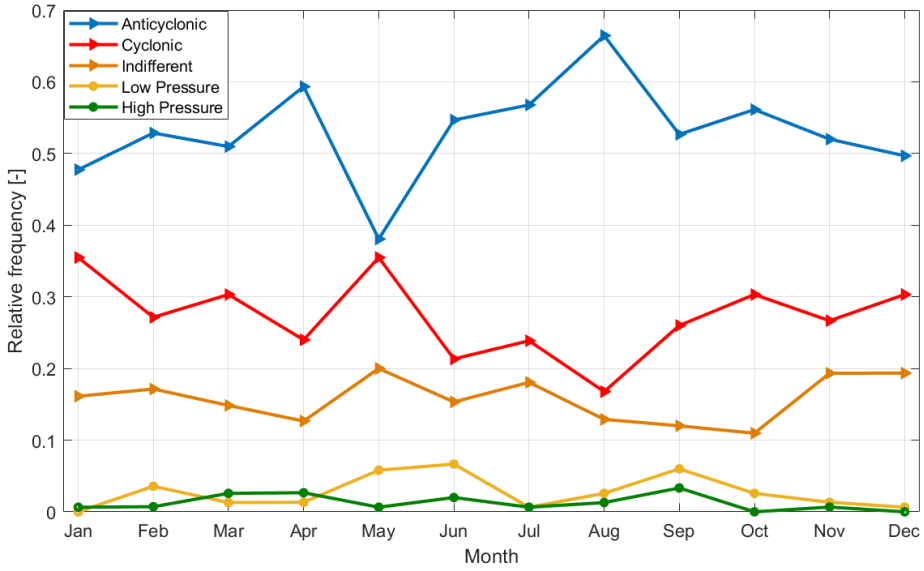

FIGURE B.11: Climatology (2016-2020) of the synoptic weather conditions over Switzerland. Triangles indicate advective weather types and circles convective ones.

B.5 Growth rate

	Winter	Spring	Summer	Autumn
KENDA/bR	121.3	229.0	227.7	102.2
MWR/PM	165.8	183.3	203.6	77.2
MWR/bR	160.0	151.8	186.2	88.1
SNR	92.7	92.3	85.9	93.3

TABLE B.1: Seasonal CBL median growth rate [m/h] in Grenchen (2016-2020) with different instruments and methods.

	Winter	Spring	Summer	Autumn
KENDA/bR	104.5	227.1	243.0	99.3
MWR/PM	105.3	157.2	165.1	84.1
MWR/bR	97.1	160.4	157.4	92.0
SNR	79.0	105.2	103.4	102.2

TABLE B.2: Seasonal CBL median growth rate [m/h] in Schaffhausen (2016-2020) with different instruments and methods.

B.6 Long-term trends

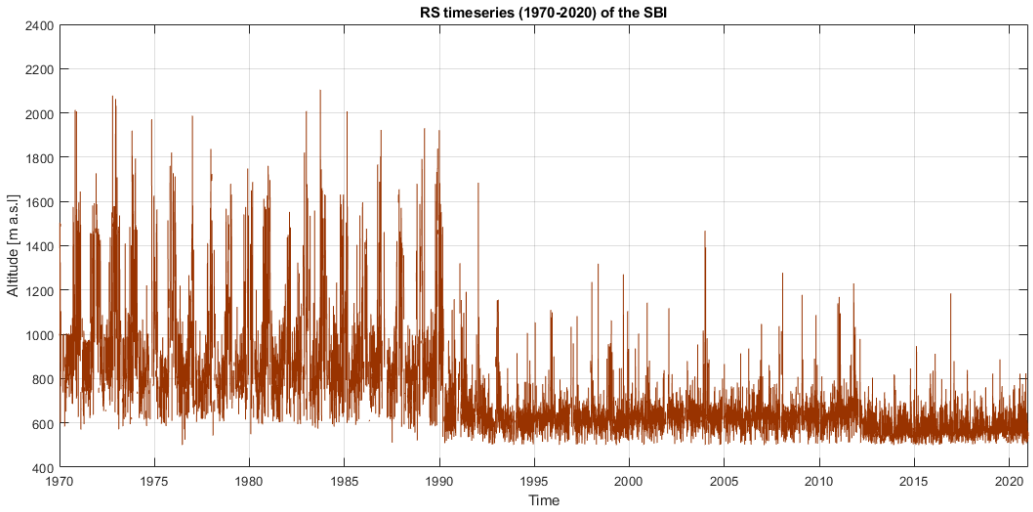

FIGURE B.12: RS/SBI timeseries between 1970 and 2020. Note the impact of important changes in vertical resolution in 1991 and 2012

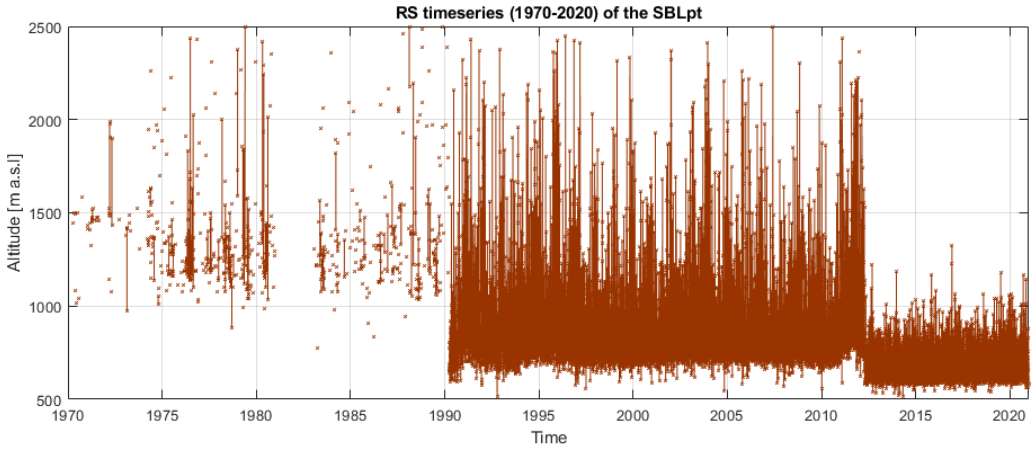

FIGURE B.13: RS/SBLpt timeseries between 1970 and 2020. Note the impact of important changes in vertical resolution in 1991 and 2012, where the resolution is too low before 1991 to be able to compute the SBLpt.

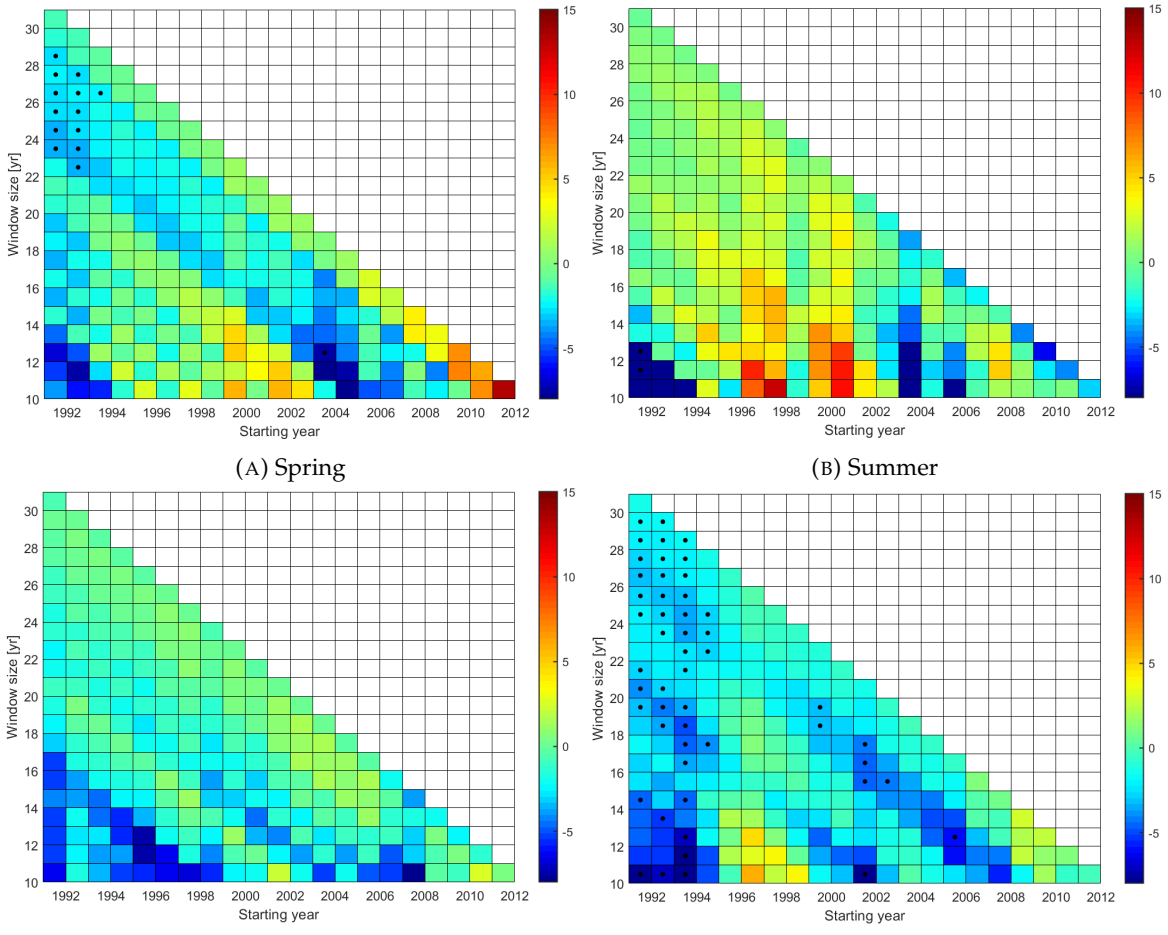

(A) Spring

(B) Summer

(C) Autumn

(D) Winter

FIGURE B.14: Seasonal Mann-Kendall trend detection on RS/bR with a 1991-2020 data set. The color scale corresponds to the associated Sen's slope [m/year] for each set of starting year and window size. Black dots indicate that the trend is significant on a 90% confidence interval.